Seasonal Trends in Titan's Atmosphere: Haze, Wind, and Clouds

Thesis by

Antonin Henri Bouchez

In Partial Fulfillment of the Requirements

for the Degree of

Doctor of Philosophy

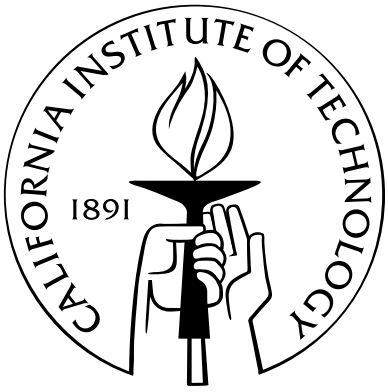

California Institute of Technology

Pasadena, California

2004

(Defended July 25, 2003)

This dissertation is dedicated to Eleta Trejo-Cantwell, my friend and partner throughout this long and sometimes difficult process.

Abstract

I present an analysis of visible and near-infrared adaptive optics images and spectra of Titan taken over 43 nights between October 1997 and January 2003 with the AEOS 3.6-m, Palomar Hale 5-m, and W.M. Keck 10-m telescopes. These observations reveal a seasonally changing stratospheric haze layer, two distinct regions of condensate clouds in the southern hemisphere, the albedo of Titan's surface, and the zonal wind field of the stratosphere.

Transient convective CH_4 clouds are identified near Titan's south pole, rising to 16±5 km above the surface. These clouds have been continuously present south of 70°S since at least December 2001, currently account for 0.5–1% of Titan's 2 μm flux, and appear to be gradually brightening or thickening as the insolation of the south polar region increases. Above the polar clouds, an extensive but optically thin ($\tau \approx 0.05$ at 2 μm) cloud layer is noted near the tropopause south of 30°S. Aside from the convective CH_4 clouds near the south pole, Titan's troposphere is free of aerosols with an upper limit of $\tau < 0.01$ on the 2 μm vertical optical depth in the 5–30 km altitude region.

The albedo of Titan's surface at 2.0 μm is derived from the radiative transfer analysis of spatially resolved spectra and images, and presented in the form of a $\sim$ 600 km resolution global surface albedo map. At this resolution, the 2.0 μm albedo ranges from 0.05 to 0.17, consistent with extensive exposure of clean water ice in some regions, while hydrocarbons and atmospheric sediments blanket others.

The zonal wind field of Titan's stratosphere near southern summer solstice is derived from adaptive optics observations of the occultation of a binary star on 20 December 2001. Multiple refracted stellar images were detected on Titan's limb during the each successive occultation, allowing the angular deflection of the starlight at two altitudes over both hemispheres to be measured with an uncertainty of $\sim$ 2 milliarcseconds. The zonal wind field derived from this measurement of the shape of Titan's limb exhibits strong but asymmetric high latitude jets, with peak wind speeds of 230 ± 20 m s^{-1} at 60°N and 160 ± 40 m s^{-1} at

40°S, and lower winds of 110 ± 40 m s^{-1} at the equator. The direction of the wind is not constrained.

Acknowledgements

My greatest thanks go to my advisor Mike Brown. For over 10 years, at U.C. Berkeley, the University of Arizona and finally Caltech, Mike has offered me opportunities, challenges, and especially inspiration.

Caitlin Griffith generously allowed me to use and modify her radiative transfer model of Titan's atmosphere, central to much of the analysis presented in this dissertation. Leslie Young provided the initial motivation for the occultation observations, and useful advice on their analysis. Special thanks go to Chad Trujillo, Henry Roe, and Chris Koresko for advice on observational and analytical techniques, and to Mark Richardson and Andy Ingersoll for helpful discussions on atmospheric physics.

Rich Dekany and Mitch Troy built the Palomar adaptive optics system, with which much of the data presented in this dissertation was collected. They frequently participated in the acquisition of the of the observations, and went out of their way to optimize the hardware for observations of Titan. Without their dedicated efforts, and support of Rick Burruss at Palomar Observatory, little of this work would have been possible.

I am grateful to Chao Bian, Randy Campbell, Joe Carson, Christophe Dumas, Josh Eisner, Bill Forrest, Elise Furlan, Luke Keller, Maciej Konacki, Jean-Luc Margot, David Le Mignant, Stan Metchev, Keven Uchida, and Dan Watson for acquiring images of Titan on their own observing time, providing otherwise unattainable nightly observations of Titan's clouds. I also thank Sarah Hörst, who spent 30 cold winter nights observing Titan from the roof of Robinson Hall, maintaining her enthusiasm throughout.

My six years at Caltech were made much more enjoyable by the companionship of my fellow GPS graduate students, especially Magali Billen, Shane Byrne, Lori Fenton, Elizabeth Johnson, Matt Pritchard, Edwin Shauble, Sarah Stewart-Mukhopadhyay, Anthony Toigo, Ashwin Vasavada, Ben Weiss, and Huiquin Wang. Finally, I thank my friend Ute Zimmermann for inspiration during the final weeks of this effort.

Contents

List of Figures

List of Tables

Chapter 1

Introduction

1.1 Opening remarks

Titan, the largest satellite of Saturn, remains one of the most mysterious objects in our solar system. This is due to its great distance from the Earth, 8.6 astronomical units during a typical opposition, and the dense, hazy atmosphere through which the surface can only dimly be seen. The possible presence of seas of liquid hydrocarbons, and an alien meteorological cycle involving these fluids, suggests that Titan's surface may exhibit many of the morphological features due to fluid erosion which we at present associate only with the Earth. It is these intriguing similarities, on a frigid and alien world, which initially drew me to study Titan.

Discoved by Christiaan Huygens in 1655, Titan remained an unresolved point of light until the close flyby of Voyager 1 in 1980. Voyager revealed the structure of Titan's atmosphere and the complexity of its chemistry, but Titan's surface and lower atmosphere

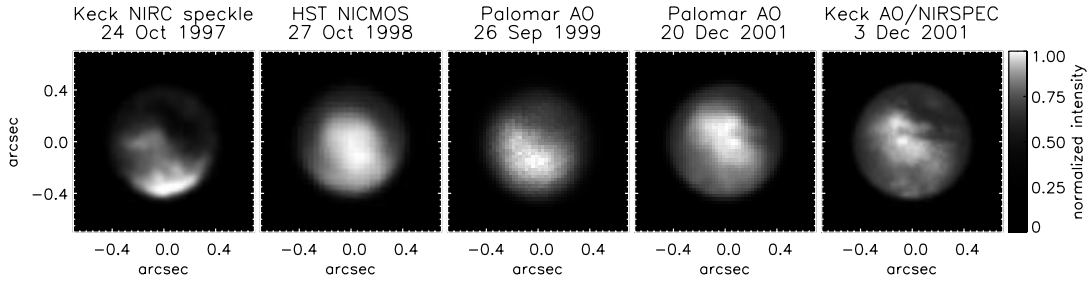

Figure 1.1: Five images of Titan's leading hemisphere, illustrating the rapidly improvements in resolution and contrast achieved in recent years. Ground-based images were taken through a K′ filter (2.0 μm) while the Hubble Space Telescope image (Meier *et al.*, 2000) was taken through filter F165M (1.6 μm).

remained hidden from its visible-wavelength cameras. It was only realized in 1991 that Titan's surface is directly observable in the near-infrared (Griffith *et al.*, 1991). This, combined with spectacular advances in the spatial resolution achievable by large telescopes, has led to a rapid evolution of our understanding of Titan's surface and troposphere over the past few years. The ever-increasing clarity with which we can view Titan's surface and troposphere is recorded in the series of papers which comprise this dissertation (Fig. 1.1). The pace of discovery is poised to intensify dramatically in July 2004, when the Cassini and Huygens spacecraft arrive at Saturn.

Though it is Titan's mysterious surface which initially motivated this work, this dissertation primarily addresses questions regarding the satellite's atmosphere. One reason is that understanding the three-dimensional distribution of absorbers and aerosols in Titan's atmosphere is a prerequisite to correctly interpreting observations of Titan's surface. The spectroscopic discovery of variable clouds in Titan's troposphere by Griffith *et al.* (1998) motivated much of the work in this dissertation. Clearly, the distribution and frequency of clouds must be understood before even such a basic property of the surface as its albedo can reliably be determined. The original intent of the observational projects described in Chapters 2, 3, and 7 was to locate these enigmatic tropospheric clouds. They were unsuccessful in this regard, but instead revealed an optically thin region of condensates near Titan's tropopause, and gradual seasonal changes in the haze structure of the stratosphere.

As the performance of adaptive optics systems steadily improved, Titan's methane clouds finally sprang into sharp focus in December 2001 (Ch. 5). Their location near Titan's south pole (currently in mid-summer) was a complete surprise and it suggests that these clouds may be analogous to summer thunderstorms on Earth, caused by the heating of moist ground by sunlight. Titan's methane storms are now routinely observed with the W. M. Keck and Palomar Hale telescopes, and more frequent observations are beginning to shed light on their lifetimes and seasonal behavior (Ch. 6). It remains to be seen how long these storms will persist, and whether similar cloud activity moves to Titan's equatorial regions as the long southern summer draws to an end in August 2009.

The observed distribution of aerosols and clouds is intimately related to the global dynamics of the Titan's atmosphere. This topic is interesting in its own right, as Titan constitutes a unique case in the solar system combining slow rotation reminiscent of Venus with substantial seasonal effects due to Titan's $26\overset{\circ}{.}7$ obliquity, similar to that of Earth and

Mars. Chapters 2 and 3 begin to address the general circulation of Titan's atmosphere, as it is revealed in the distribution of stratospheric haze and an unknown condensate near the tropopause at high southern latitude. Chapter 4 reports the results of an occultation of a binary star by Titan, from which wind velocities in Titan's stratosphere are directly measured.

Finally, I also present in this dissertation maps of Titan's surface albedo at both visible and near-infrared wavelengths (Ch. 2 and 6). These are the first surface maps free of artifacts induced by a zonally averaged subtraction, and reveal several surprising features of Titan's enigmatic surface.

1.2 Methods

1.2.1 Adaptive optics

Titan's hazy disk never subtends more than $0\farcs88$ as seen from the Earth. This is roughly equal to the scale of the image degradation imposed on ground-based telescopes by turbulent mixing of air of differing refractive indices in the Earth's atmosphere. Ground-based telescopes with traditional, fixed optical components can therefore resolve little or no detail on Titan.

Adaptive optics (AO) systems, whose conceptual basis was first proposed by Babcock (1953), correct the blurring induced by the Earth's atmosphere on astronomical images. The light of a guide-star, its phase aberrated due to its passage through the Earth's inhomogeneous and constantly varying atmosphere, is monitored using a wavefront sensor. Based on the wavefront measurement, a shape is applied to the surface of a deformable mirror, mechanically adjusting the length of the path which the light travels to cancel the aberrations induced by the atmosphere.

An ideal AO system would correct the light of the guide-star and of the field surrounding it to its original state, leaving the resolution of the final image limited only by the size of the telescope's primary mirror. Current AO systems, however, can provide only a partial and variable correction of the incoming light. Any object imaged with such a system exhibits a sharp, high resolution core, surrounded by a broad halo of uncorrected light. The visible effect of this blurry halo has been suppressed as much as possible in images displayed in this dissertation by a judicious choice of gray-scales, but its effect must be accounted for in

the analysis of the observations.

This dissertation is based on images and spectra of Titan taken with the Advanced Electro-Optical System (AEOS), Palomar Hale, and Keck-II adaptive optics systems. The initial development and gradual improvement of these AO systems over the past five years (all achieved first light in 1998–1999) have propelled the rapid advances in our understanding of Titan's atmosphere and surface which are described herein.

1.2.2 Radiative transfer calculations

Titan's hazy atmosphere poses a multitude of problems to investigations of the surface and troposphere. Thought the behavior of light through an absorbing and scattering medium is well understood (see Goody and Yung, 1989) the difficulty lies in both the poorly constrained properties of Titan's atmosphere (aerosol distribution and phase function), and its physical thickness.

I have attempted in this dissertation to treat radiative transfer through Titan's atmosphere in a precise and self-consistent fashion. The vertical and latitudinal distribution of aerosols in Titan's atmosphere is determined in Ch. 3 by fitting the spectra predicted by a radiative transfer model to spatially resolved spectra of Titan recorded with the Palomar adaptive optics system over a two year period. The radiative transfer model used is that of Griffith *et al.* (1991), a plane-parallel model which assumes a simple Mie scattering phase function, with constant-sized aerosols throughout the haze layer. More details of the model are given in Section 3.4.2. Though the geometric and phase assumptions are simplifications, modeled spectra reproduce those measured to within the observational errors and constrain the thickness and vertical distribution of the haze more precisely than previous analyses of broad-band images of Titan's haze (Gibbard *et al.*, 1999; Young *et al.*, 2002). I have then used this same radiative transfer model, with the three-dimensional aerosol distribution derived from resolved spectra, to analyze broad-band images of Titan taken with the Palomar and Keck adaptive optics systems (Ch. 6).

Chapter 2

Visible adaptive optics observations of Titan's atmosphere and surface

2.1 Introduction

The close flyby of Titan by Voyager 1 in 1980 revealed a deep, hazy atmosphere of N_2 and CH_4, beneath which the surface remained hidden. Zonal structure was noted in the main stratospheric haze layer with the southern hemisphere appearing 15–20% brighter than the north in violet through green filters (370–600 nm), and a dark polar collar encircling the north pole (Smith *et al.*, 1981). Sromovsky *et al.* (1981) showed that a seasonal alternation of this north-south hemispheric asymmetry (NSA) can account for much of the long-term photometric variability of Titan at those wavelengths. After a 10-year data gap, Titan was imaged once again with the Hubble Space Telescope (HST), confirming that the NSA had reversed sign at 440 and 550 nm (Caldwell *et al.*, 1992). The temporal evolution of the NSA at a wide range of wavelengths (336–953 nm) has since been monitored regularly with HST.

The seasonal variations in the appearance of Titan's haze reflect changes in the mid- and upper-stratospheric aerosol distribution (above $\sim$ 70 km altitude) due to the advection of the smallest particles by thermally direct winds (Lorenz *et al.*, 1997, 1999, 2001). The NSA exhibits a peak contrast near equinox, but its sign and phase depend on the wavelength of observation. This is because the single-scattering albedo of Titan's stratospheric aerosols

[1]This chapter has been submitted for publication in *Icarus* as a paper of the same title by authors A.H. Bouchez, M.E. Brown, C.R. Neyman, M. Troy, and R.G. Dekany.

varies greatly across the visible spectrum (McKay *et al.*, 2001). Shortward of approximately 600 nm, an increase in the optical thickness of haze darkens the bright Raleigh scattering atmosphere below. At longer wavelengths, particularly in the CH_4 absorption bands at 890 nm and beyond, the haze appears bright against a dark lower atmosphere and surface. In both the ultraviolet and the near-infrared CH_4 bands, Titan's lower stratosphere and troposphere are opaque, and only uppermost region of the main haze layer is visible. Seasonal changes at these highest levels lead those in the main layer by several years (Lorenz *et al.*, 1999). The most recent HST observations, acquired in November 2000 (solar longitude $L_s = 240°$, where $L_s = 270°$ corresponds to southern summer solstice), show accelerating haze redistribution from the southern to the northern hemisphere, though the main haze layer remains thicker in the south (Lorenz *et al.*, 2001).

Though opaque at wavelengths imaged by Voyager ($\lambda < 650$ nm), Titan's haze becomes increasingly transparent at longer wavelengths due to a combination of particle size and the optical properties of the organic aerosol material (McKay *et al.*, 2001). Between methane absorption bands, photons from Titan's surface, sometimes singly or multiply scattered in the haze layer, can reach an observer above the atmosphere. Smith *et al.* (1996) used HST images in filters centered at 850 and 1042 nm, sampling Titan's atmospheric transmission windows at 940 and 1080 nm, to produce the first map of relative surface albedo of Titan. These maps show a generally dark surface with a large (4000×2500 km) bright region roughly centered on Titan's leading hemisphere (110°W, 10°S), as well as many smaller bright and dark features. However, to compensate for the haze-scattered sunlight admitted by the broad filters on board HST, a zonally averaged image was subtracted from individual images to create the maps. This procedure increased the contrast of certain mapped features, but led to the loss of all zonally symmetric surface or cloud patterns. The same technique was used by Meier *et al.* (2000) to derive relative albedo maps from 1–2 μm HST images taken with the NICMOS camera though they note that their zonally averaged atmospheric images included banded structures which might be clouds near Titan's surface.

Variations in Titan's near-infrared spectrum clearly show that clouds do form in Titan's troposphere (Griffith *et al.*, 1998, 2000). Both large, apparently infrequent cloud-formation events (covering 7% of Titan's disk on 5 September 1995), and smaller daily clouds (covering $\sim 1\%$ of the disk) have been observed. Recently, Lorenz *et al.* (2001) report that HST images taken through a narrow-band filter at 953 nm show a bright southern limb which between

1996 and 2000 did not appear to undergo the seasonal changes observed in Titan's main haze layer. They interpret the feature as evidence for a zonally symmetric CH_4 cloud layer, condensing onto C_4N_2 ice crystals falling through Titan's upper troposphere, a process predicted by Samuelson *et al.* (1997) to occur in spring when stratospheric temperatures reach a minimum. Ground-based near-infrared adaptive optics (AO) observations with the Keck-II 10-m telescope have resolved a circumpolar ring of condensates at greater than 30–40 km altitude in this same region (Roe *et al.*, 2002). It remains unclear whether this represents the same feature observed with HST and in the observations reported here, or a higher cloud (such as the C_4N_2 stratospheric ice cloud).

Further progress in understanding of the seasonal cycle of Titan's stratospheric haze, and the location and physical processes governing condensate clouds on Titan, require observations which combine high spatial, temporal, and spectral resolution. We have therefore undertaken a nightly monitoring campaign with the Advanced Electro-Optical System (AEOS), a 3.63-m telescope operated by the U.S. Air Force on Heleakala Volcano, Maui, capable of nearly diffraction-limited imaging at 700–1000 nm. The results of the initial two weeks of observation are reported here.

2.2 Observations and data reduction

Observations of Titan were acquired on 7 nights between 7 November and 17 December 2000 (UT), and 7 out of 8 consecutive nights from 18 to 25 November 2001. Atmospheric conditions on 23 November 2000 were very poor and those data are not included in this analysis. Observational parameters and filters used on each night are summarized in Table 2.1.

2.2.1 AEOS adaptive optics system

The f/200 beam of the altitude-over-azimuth AEOS telescope is directed to a coudé optical bench below the telescope where it enters the AEOS AO system. This consists of a tip-tilt sensor ($\lambda < 500$ nm) driving a fast tracking mirror, and a Shack-Hartmann wavefront sensor ($500 < \lambda < 700$ nm) controlling a 941-actuator deformable mirror, which together partially correct atmosphere-induced wavefront aberrations of the $\lambda > 700$ nm science beam (Abreu *et al.*, 2000). The science beam is then directed through an image de-rotator to the Visible Imager camera, where it is focused on a 512×512 pixel fast-readout Roper Scientific CCD

Table 2.1: AEOS observations

UT Date	Time	Filters[a]	Int.[b]	Pscl.[c]	Sub-Earth[d]	Sub-solar[e]	FWHM[f]	Strehl[g]
2000 Nov 07	08:45–12:54	a, b, c, d, e	30	0.0205	257.4,−23.5	259.0,−23.5	0.10–0.20	0.04–0.13
2000 Nov 08	09:20–12:47	a, b, c, d, e	1	0.0205	281.0,−23.5	282.4,−23.5	0.10–0.12	0.06–0.13
2000 Dec 09	07:14–11:06	a, b, c, d, e	1	0.0492	261.0,−23.1	258.6,−23.7	0.17–0.30	0.02–0.06
2000 Dec 10	06:08–11:24	a, b, c, d, e	1	0.0492	283.5,−23.1	281.0,−23.7	0.14–0.25	0.03–0.06
2000 Dec 16	07:52–09:19	a, b, c, d, e	1	0.0492	59.4,−23.0	56.2,−23.8	0.16–0.18	0.04–0.06
2000 Dec 17	08:22–09:04	a, b, c	1	0.0492	82.2,−23.0	78.9,−23.8	0.15–0.18	0.04–0.06
2001 Nov 18	09:14–10:13	a, b, c, d	5	0.0205	90.2,−25.7	92.1,−25.7	0.10–0.12	0.08–0.17
2001 Nov 19	09:14–09:46	a, b, d	5	0.0205	112.6,−25.7	114.5,−25.8	0.09–0.12	0.11–0.20
2001 Nov 20	09:43–10:16	a, b, d	5	0.0205	135.8,−25.7	137.5,−25.8	0.10–0.11	0.08–0.12
2001 Nov 21	10:09–10:52	a, b, d	5	0.0205	158.9,−25.7	160.5,−25.8	0.10–0.11	0.11–0.14
2001 Nov 23	10:29–10:57	a, b, d	5	0.0205	204.7,−25.7	206.0,−25.8	0.10–0.12	0.07–0.10
2001 Nov 24	09:30–10:27	a, b, d	5	0.0205	226.6,−25.6	227.8,−25.8	0.12–0.14	0.06–0.07
2001 Nov 25	12:10–12:41	a, b, d	5	0.0205	251.4,−25.6	252.5,−25.8	0.14–0.16	0.05–0.07

a. Filters used: $a = 890$ nm, $b = 940$ nm, $c = 950$ nm, $d = 960$ nm, $e = 1000$ nm
b. Integration time (s).
c. Detector platescale ($''$ pix^{-1}).
d. West longitude and latitude of the sub-Earth point (°).
e. West longitude and latitude of the sub-solar point (°).
f. PSF full-width at half maximum ($''$).
g. The ratio of the PSF peak value to that of a diffraction-limited PSF of equal total flux.

at one of three selectable platescales. On bright targets ($V < 5$), the AEOS AO system can be run at up to 200 Hz closed-loop bandwidth and the resulting point spread function (PSF) can approach that imposed by the telescope diffraction limit, with a full-width at half maximum (FWHM) of $0\farcs053$ at 950 nm (Roberts and Neyman, 2002). Observations of Titan and reference PSF stars ($V \approx 8.2$) required longer integration times on the tip-tilt and Shack-Hartmann sensors, leading to only a partial and variable correction of the seeing-limited PSF.

The tracking and deformable mirror feedback loops were run at between 10 to 20 Hz closed-loop bandwidth on Titan and PSF reference stars, depending on the atmospheric turbulence conditions. The resulting short-exposure PSF typically consisted of a narrow, occasionally cross-shaped core region with FWHM between $0\farcs08$ and $0\farcs20$, with a broad seeing-limited $1''$–$2''$ halo containing most of the light. The FWHM, shape of the core, and fraction of light in the core and halo were found to vary substantially over time scales of 10–100 s. In addition, low-frequency (~ 1 Hz) image motion left uncorrected by the tip-tilt feedback loop compromised the resolution in exposures longer than 1 s taken during the year 2000 observing runs. This image motion was substantially reduced by modifications made to the secondary mirror control loop and support structure in mid-2001.

Our observing strategy was motivated by the need to maximize the resolution of the

final Titan images, while accurately characterizing the varying PSF with which they were recorded. We therefore alternated sets of short exposures of Titan and one of several PSF calibration stars, then summed the frames of each after correcting for the image motion. The PSF calibration stars were HD 24886 and HD 22481 in 2000, and HD 29158, HD 30191, and HD 29512 in 2001. These were chosen to be isolated field stars near Titan ($< 5^\circ$ away) and of similar magnitude (V=8.09–8.35) and color (F5–G8), to attempt to reproduce identical performance in the AO system. Nevertheless, AO performance may differ between the unresolved stars and Titan, particularly on nights of excellent seeing when Titan may be marginally resolved in the wavefront sensor sub-apertures. A further source of PSF uncertainty is due to the coudé location of the AEOS adaptive optics system. Most azimuthally asymmetric PSF artifacts will remain fixed with respect to the orientation of the deformable mirror, and thus will appear to rotate on the sky. Observations prior to 19 November 2001 used the image de-rotator to keep celestial north fixed along one axis of the detector, causing the PSF artifacts to rotate on the detector. To improve the fidelity of the PSF estimates, the de-rotator was left in its parked position subsequent to this date. The integration time and platescale used varied over the course of the observing period in response to changes in atmospheric conditions, and are listed in Table 2.1.

2.2.2 Data reduction

Individual frames (Titan or PSF star) were bias and dark current subtracted, then divided by a flat field map determined from twilight sky observations made during the same observing run. At least two sources of vignetting of the coudé/AO beam affect the large-scale illumination pattern of the Visible Imager detector. In the $0\farcs0205$ pix^{-1} platescale, vignetting within the Visible Imager leads to a roughly conical illumination pattern. This pattern is not present at other platescales. In addition, vignetting of the coudé beam upstream of the AO system generates a superimposed $\sim 1\%$ amplitude spider-shaped illumination pattern which appears to remain stationary with respect to the orientation of the telescope pupil, thus rotating with respect to the AO system and the sky (Roberts, 2001). We therefore in 2001 acquired sets of zenith twilight sky observations with the telescope positioned every 30° of azimuth and the image de-rotator parked, and used the appropriate mean flat map for the reduction of each Titan and PSF image. Rotationally resolved flats were not acquired during the 2000 observing runs, so images were reduced using a single

mean flat, leading to possible $\sim 1\%$ systematic gain errors on spatial scales of $\sim 1''$. This is not a problem for the observations described here.

The short-exposure images necessitated by the low-frequency image drift led to very low signal-to-noise ratio (SNR) in individual frames, ranging from 0.9 to 15.3 pix^{-1}. We tested several techniques for aligning the frames by constructing model images of Titan with the appropriate flux and noise levels and measuring the root-mean-squared (RMS) difference between the recovered and input disk center locations. The technique found to be most precise in this SNR range was to cross-correlate a blank disk with a map of those pixels higher than 0.5 times the brightest in the frame, which effectively kept noise and features on Titan's disk from biasing the measured disk center. The simulations demonstrated that at an SNR of 3.0 pix^{-1}, the center of Titan's disk could be located to better than 0.5 pix ($0\farcs010$) RMS, growing rapidly worse with lower SNR. In certain cases, as noted in Table 2.1, we therefore summed the consecutive frames in sets of up to 10 to increase the SNR to a minimum of 3.0 before measuring the disk center. This is equivalent to increasing the original integration times in these filters, though at the cost of some loss of efficiency due to increased readout noise and overheads. Images were then shifted to a common center by adding a phase ramp to their Fourier transform, then transforming back to the image domain. This technique allows one to perform sub-pixel shifts while keeping the power spectrum of the image unchanged.

PSF calibrator images were similarly shifted to a common center, measured by performing a least-squares fit of a 2-D Gaussian function to the PSF core (central 5×5 pixels) and adopting its central coordinates. The centered images of Titan and the PSF calibrator stars were then summed in the original sets of consecutive observations, thus producing final images with typical total integration times of 100 s. Between 3 and 12 sets of Titan frames were taken in each filter each night, reduced by the methods detailed above to 3–12 independent images with associated PSF estimates. In a final step, the best 3 of these images were resampled at 4 times their original pixel scale, rotated to a common orientation (celestial north up, east left), and added in a nightly mean image. These nightly mean images and PSFs are displayed in Fig. 2.1.

Though all the nights included in this study were free of clouds, no absolute photometric calibration was attempted, since several of the filters fall within a variable telluric H_2O absorption band (927–970 nm). However, as detailed below, relative photometric calibration

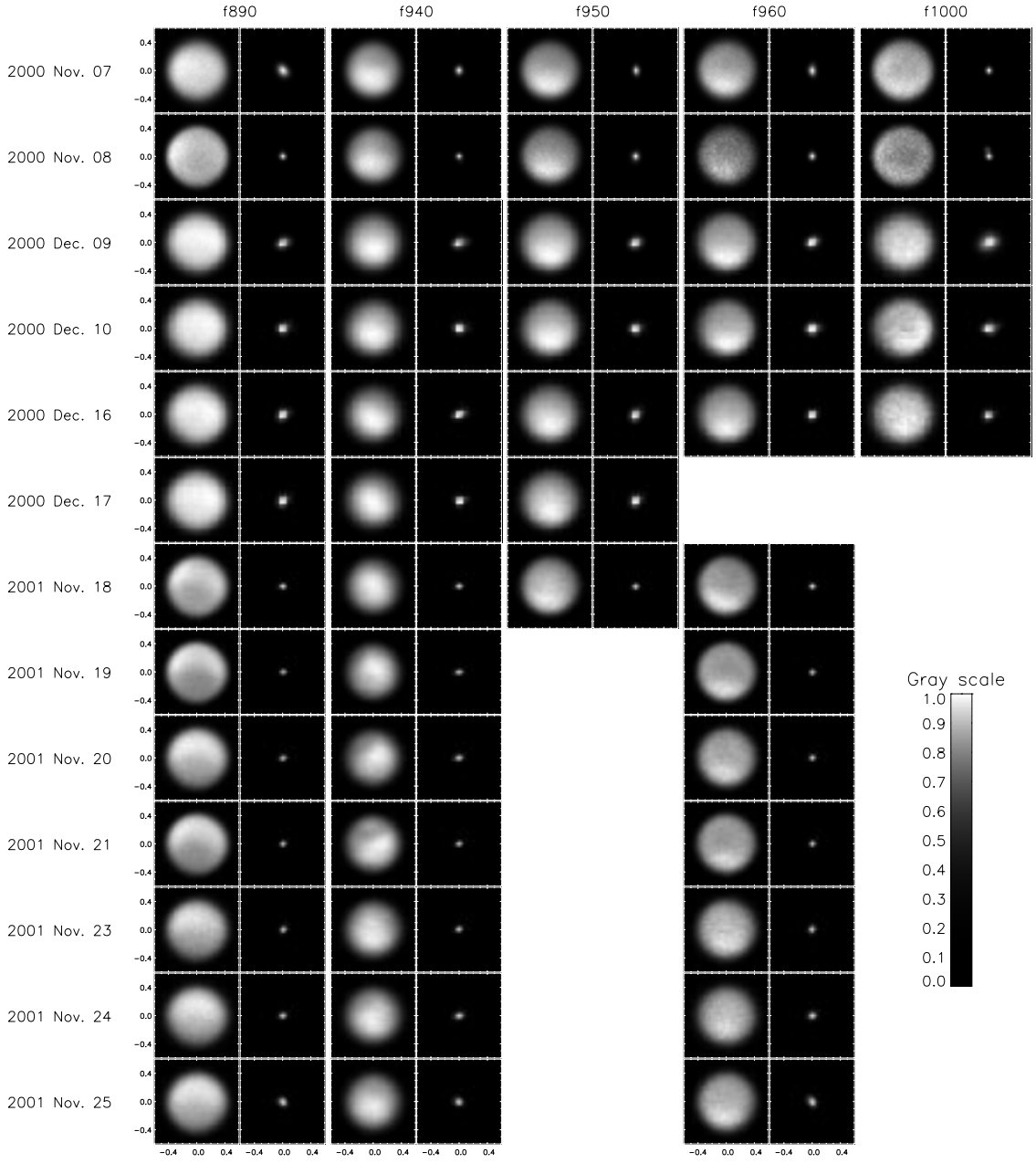

Figure 2.1: Mean nightly images of Titan with associated PSF estimates. Filters are shown in order of increasing wavelength from left to right, observation epoch increases from top to bottom. Not all filters were used every night. All images are scaled with respect to their brightest pixel. Filters at 890 and 1000 nm image only Titan's stratospheric haze, 950 and 960 nm probe the haze and troposphere, while 940 nm penetrates to Titan's surface.

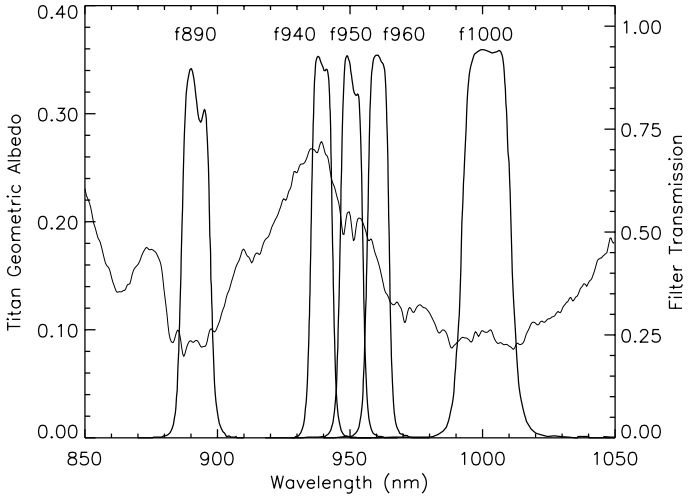

Figure 2.2: Filter transmission curves superimposed on a spectrum of Titan from Karkoschka (1998).

of the 940-nm images was performed by tracking features on Titan's surface.

2.2.3 Filters

We recorded images of Titan and PSF calibrator stars through 5 custom-made interference filters between 890 nm and 1 μm, manufactured by Andover Corporation. Transmission curves are shown in Fig. 2.2, while filter names and bandpasses are listed in Table 2.2. The bandpasses chosen selectively probe various depths of Titan's atmosphere, using the strongly varying CH_4 absorption in this spectral region as a vertical discriminator.

Table 2.2: AEOS Filters

Name	Wavelength[a]	FWHM[b]	τ_{surf} [c]	$\tau = 1$ altitude [d]
890	891.86	11.03	16 ± 2	80
940	939.33	8.26	0.22 ± 0.04	-
950	950.54	8.65	1.9 ± 0.4	7 ± 1
960	960.56	8.33	4.3 ± 0.7	20
1000	1001.47	18.89	10 ± 0.5	59

a. Central wavelength (nm).
b. Full width at half maximum transmission (nm).
c. Effective two-way opacity to surface due to CH_4 absorption at normal incidence, with uncertainty due to 3–10% allowed range of CH_4 surface mixing ratio.
d. Altitude above surface at which effective two-way opacity is 1 (km).

We have used a simple radiative transfer model of Titan's atmosphere to estimate the depth to which each filter is sensitive. Only absorption by methane in considered, as this is the most important opacity source in this wavelength range (Young *et al.*, 2002). Titan's atmosphere is modeled as 147 layers ranging in thickness from 0.5 km near Titan's surface to 50 km at 1200 km altitude, using the temperature-pressure model of Lellouch (1990). In our baseline model, the CH_4 mixing ratio in the lower troposphere is assumed to be 0.07, up to the height at which this equals the saturation value. The saturation mixing ratio is then followed to the tropopause at 40 km, above which the saturated tropopause value of 0.017 is followed (Lellouch *et al.*, 1989). The 0.4 nm resolution methane absorption coefficients κ_λ measured by Karkoschka (1998) were then used to predict the effective two-way opacity $\tau_{CH_4}(L)$ from the top of the atmosphere to the bottom of layer L for each filter, in a manner similar to that used by Roe *et al.* (2002);

$$\tau_{CH_4}(L) = -\ln\left(\sum_{w=1}^{W} f_w \exp\left[-\sum_{l=L}^{l_{top}} 2\kappa_w u_l h_l \mu\right]\right), \tag{2.1}$$

where u_l is the abundance of CH_4 in layer l, h_l is the layer thickness, μ is the cosine of the incidence angle, and f_w is the interpolated, volume normalized transmission of the filter in wavelength bin w at which the absorption coefficients are known.

Plots of $\tau(L)$ for each filter at incidence angles of 0° and 60° are shown in Fig. 2.3. Varying the CH_4 mixing ratio at Titan's surface from 0.03 to 0.10, shown as the thin diverging lines near Titan's surface in both plots, has little effect on the altitude sensitivity predicted for these filters. The two-way opacity τ_{CH_4} to Titan's surface, and the altitude at which $\tau_{CH_4} = 1$ for all filter passbands are listed in Table 2.2.

2.3 Results

2.3.1 Stratosphere

AEOS images of Titan through 890 and 1000-nm filters deep in CH_4 absorption bands show a limb-brightened disk with zonally symmetric structure, devoid of features rotating with Titan's surface (Fig. 2.1). Absorption by CH_4 renders Titan's lower atmosphere opaque at these wavelengths, and only sunlight scattered off aerosols above 50 and 70 km, respectively, contributes significantly to the images.

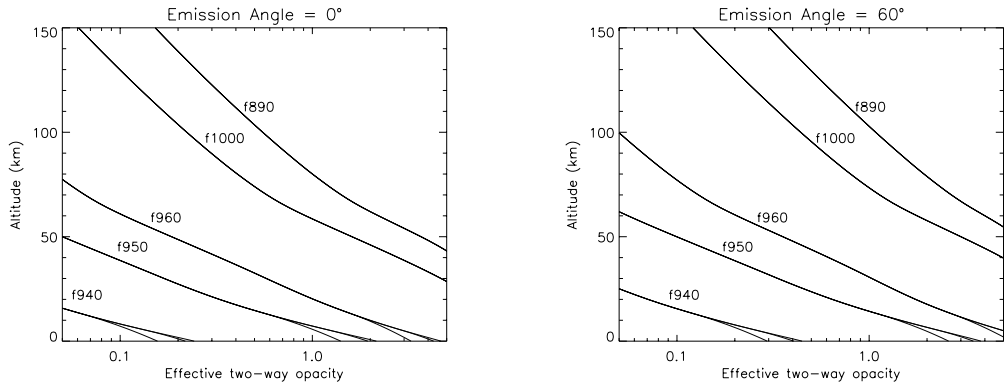

Figure 2.3: Effective two-way opacity due to CH_4 absorption averaged over each filter bandpass, as a function of altitude above Titan's surface. The uncertainty due to varying Titan's surface CH_4 mixing ratio from 3% to 10% is shown as thin lines diverging from the 7% nominal case.

890-nm images of Titan in November and December 2000 show a nearly uniform disk, with a conspicuous bright eastern (in November) or western (in December) limb. 1000-nm images display similar features but with lower SNR, due to the decrease in detector sensitivity near 1 μm. The region south of $\sim$ 60°S and the northern limb appear less bright than the equatorial band, suggesting a higher concentration of stratospheric haze above Titan's equator. The limb brightening is enhanced in the low latitude band, and further enhanced on the limb observed at lower solar zenith angle, giving the appearance of asymmetric ansae. The E-W limb-brightening $I_{\rm E}/I_{\rm W}$ asymmetry evolved over the 2000 observing period, with the brightest point on Titan's eastern limb at the equator 7% brighter than that on the western limb on 8 November 2000 (11 days prior to opposition, solar phase angle 1.°6) transitioning to $I_{\rm E}/I_{\rm W} = 0.98$ by 9 December (20 days after opposition, solar phase angle $-2.°4$), the next night of observation. Since we are under-resolving Titan's limb, the measured intensity ratio between Titan's limbs is a function of the telescope/AO system PSF, and as such the 9 December value is depressed with respect to the higher strehl ratio achieved on 8 November. Nevertheless, the asymmetry appears consistent in sign and approximate magnitude with those noted in many previous near-infrared observations (Meier *et al.*, 2000; Roe *et al.*, 2002).

The appearance of Titan's stratospheric haze changed substantially between December 2000 and November 2001 (see Fig. 2.4). Continuing the trend underway since at least

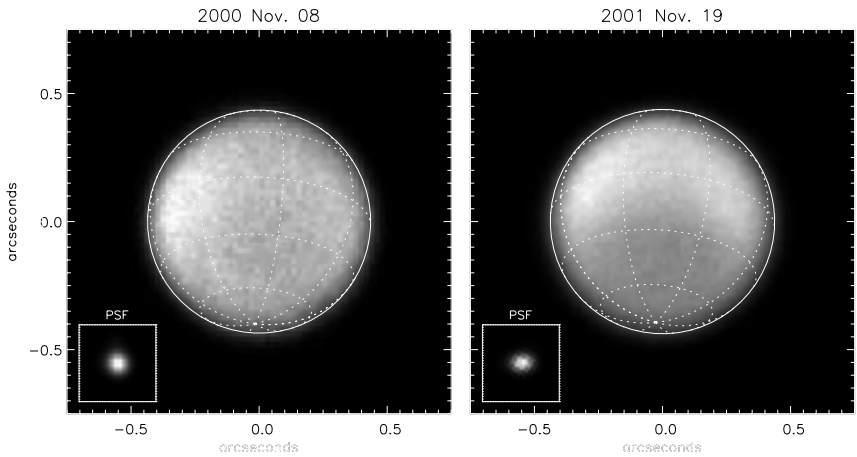

Figure 2.4: Highest resolution 890-nm images of Titan's stratospheric haze taken in 2000 and 2001. Seasonal migration of haze particles from the southern to northern hemisphere, which began in 1995 (Lorenz *et al.*, 1999), continues at a rapid pace.

1995 (Lorenz *et al.*, 1999), the high stratospheric haze (> 90 km) viewed in the 890 nm CH_4 absorption band has moved north, with the brightest region now residing north of the equator. This appears to be due to both a decrease in scattering south of 30°S, and an accompanying increase north of Titan's equator. The brightest point on Titan's limb as seen at the $\sim 0\farcs10$ resolution of the AEOS has consequently shifted from 15°S on 8 November 2000 to Titan's equator on 19 November 2001. All observations in 2001 described here were performed prior to Titan opposition. A steady decrease in the east-west limb brightening asymmetry was observed as the solar phase angle decreased from $1\fdg9$ on 18 November, when $I_E/I_W = 1.03$ to $1\fdg1$ on 25 November, when $I_E/I_W = 1.01$.

2.3.2 Troposphere

Filter at 950 and 960 nm record primarily solar photons scattered in Titan's atmosphere above 7 and 20 km altitude, respectively, as shown in the radiative transfer results in Fig. 2.3. As also predicted by these calculations, albedo patterns on on Titan's surface are suppressed in 950-nm images with respect to the atmospheric features above them, but can still clearly be recognized. We therefore concentrate our analysis of scattering in Titan's troposphere on the 960-nm images, which are predicted and observed to have negligible transmission to Titan's surface.

The most obvious feature in 960-nm images from both the 2000 and 2001 observing

periods is a bright region of scattering at high southern latitudes. This feature appears equally bright in both 960 and 950-nm images, and must therefore be located above ~ 30 km altitude. The feature is clearly absent in the 890-nm images already discussed, and faintly visible in the more noisy 1000-nm images (see in particular the nightly mean 1000-nm image from 7 November 2000). Its absence at 890 nm and places an upper altitude limit at 65 km ($\tau_{CH_4} = 3$ at 60° emission angle). The fainter detection at 1000 nm would be consistent with scattering between 40 and 65 km (τ_{CH_4} =1–3) above Titan's surface. This cloud or haze must therefore be located near Titan's tropopause (40 km) or in the lowest stratosphere.

In addition to the southern cloud/haze cap, the 960-nm images include photons scattered in Titan's main haze layer well above the tropopause. To search for more subtle structures below the main haze layer, we subtracted nightly mean 890-nm images from each 960-nm image taken in November 2001, scaled to minimize the square of the residual intensity beyond Titan's geometric limb (see Fig. 2.5). The telescope/AO PSF achieved during the year 2000 observing runs proved too variable to allow an accurate subtraction. To the extent that the optical properties of Titan's main haze layer are similar at 890 and 960 nm, these subtracted images should display only light scattered between approximately 20 and 80 km altitude in Titan's atmosphere.

The $(960 - 890)$-nm subtracted images show only a global residual over Titan's entire disk, and the bright southern cloud/haze cap mentioned above. No night-to-night changes or zonally asymmetric features are apparent which cannot be attributed to noise or instrumental effects (a malfunction of the image rotator on 18 November 2001 accounts for the apparent east-west asymmetry seen on that night only). In particular, large transient CH_4 condensate clouds in the mid-troposphere, such as those observed spectroscopically by Griffith *et al.* (1998) covering 7% of Titan's disk, would be clearly visible in these 0.″10–0.″12 resolution difference images, had they been present.

We modeled the $(960 - 890)$-nm subtracted images using a weighted average of the 960 and 890 nm nightly mean PSFs to determine the nature of residual and the physical extent of the bright southern cap. The global residual appears to be limb-darkened, with a best-fit exponent to an $I = I_0\mu^{2k}$ Minnaert scattering law, where μ is the cosine of light's emission angle, of $k = 1 \pm 0.5$. It is probably due to light scattered in the nearly uniform lowest levels of Titan's main haze layer, with the apparent phase function being due to absorption by CH_4 at longer path lengths. If assumed to be a single contiguous region of uniform

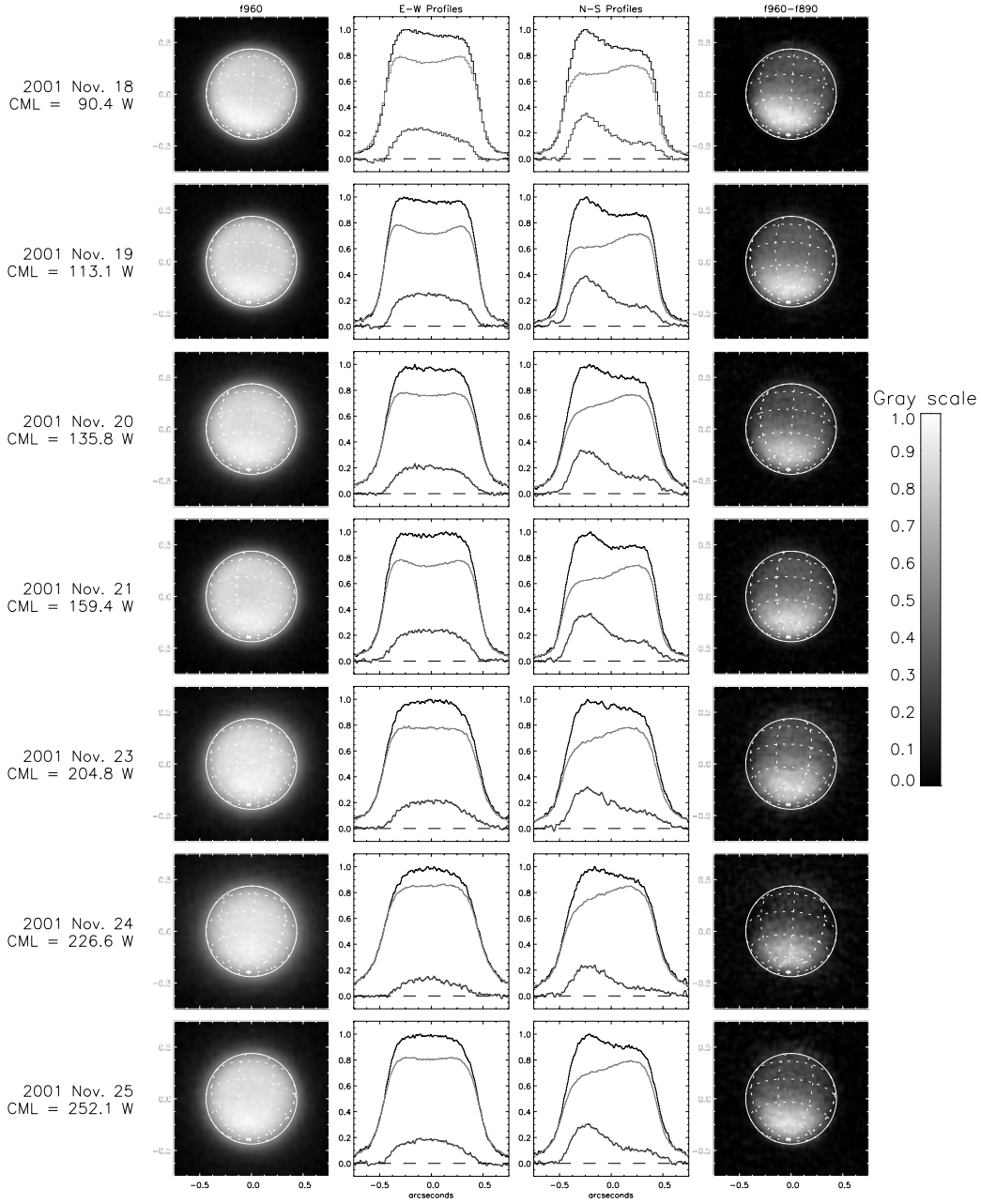

Figure 2.5: The subtraction of stratosphere-only 890-nm images from those at 960 nm sensitive to scattering in Titan's troposphere reveals a bright scattering region at high southern latitudes and a limb-darkened, global residual. *Left*: Nightly mean 960 nm images taken on 7 of 8 consecutive nights in November 2001. Images have been scaled individually. *Middle columns*: East-west and north-south (celestial) relative intensity profiles across the center of Titan's disk at 960 nm (top, dark line) and 890 nm (middle gray line, scaled to give zero mean residual beyond Titan's true limb). Lower dark line shows north-south profile of subtracted image, which consists only of photons scattered between approximately 20 and 80 km above Titan's surface. *Right*: (960 − 890)-nm subtracted images.

brightness, the southern cloud/haze cap must extend from $40^\circ \pm 5^\circ$ S to near Titan's south pole. It is not as strongly limb-darkened as the global residual, ($k = 0 \pm 0.5$), and therefore may be either optically thick or higher in Titan's atmosphere.

2.3.3 Surface

The 940 nm filter was chosen to view Titan's surface with minimum CH_4 absorption, but the two-way CH_4 opacity nevertheless ranges from 0.22 ± 0.04 at 0° incidence to 0.36 ± 0.06 at 60° incidence. The one-way scattering optical depth of the main haze layer is predicted to be $\tau_{scat} \approx 2$ (McKay *et al.*, 2001), so most surface-reflected photons will be scattered more than once on their way out of Titan's atmosphere. Titan's surface should therefore appear blurred on scales of 100–200 km, and the contrast of surface features diluted by sunlight scattered directly off haze and condensates in the atmosphere.

Surface features can clearly be discerned in the nightly averaged 940-nm images displayed in Fig. 2.1, rotating eastward (on Titan) 23° per day. Their contrast can be increased by subtracting the light scattered directly off overlying haze and clouds, sampled at 960 nm. The optical properties of the overlying haze and condensates are unlikely to vary appreciably between 940 and 960 nm. The empirical scaling factor by which to multiply each 960-nm image to match the radiance due to scattering in Titan's atmosphere sampled by the corresponding 940-nm surface image was again determined by minimizing the square of the residual beyond Titan's geometric limb. The $(940 - 960)$-nm subtracted images thus calculated are displayed in Fig. 2.6. They effectively display only light scattered below ~ 20 km altitude in Titan's atmosphere or on the surface.

We were initially unable to flux calibrate the images due to variable telluric H_2O absorption band at 927–970 nm. However, the brightening and fading of surface features due to the surface phase function and the extinction of the overlying CH_4-rich atmosphere provides a method of calibration of the haze subtracted surface images, which we can then combine into a map of Titan's relative surface albedo at 940 nm. We begin by map-projecting each haze subtracted nightly mean image of Titan, resampling on a fine latitude-longitude grid such that at least 4 grid points correspond to each image pixel. Ideally one could determine a mean effective phase function for Titan's surface by dividing the radiance at each location in every map by that observed at zero phase angle, and fitting a model to the normalized radiances. Since few locations on Titan were actually observed at zero phase, we loosen

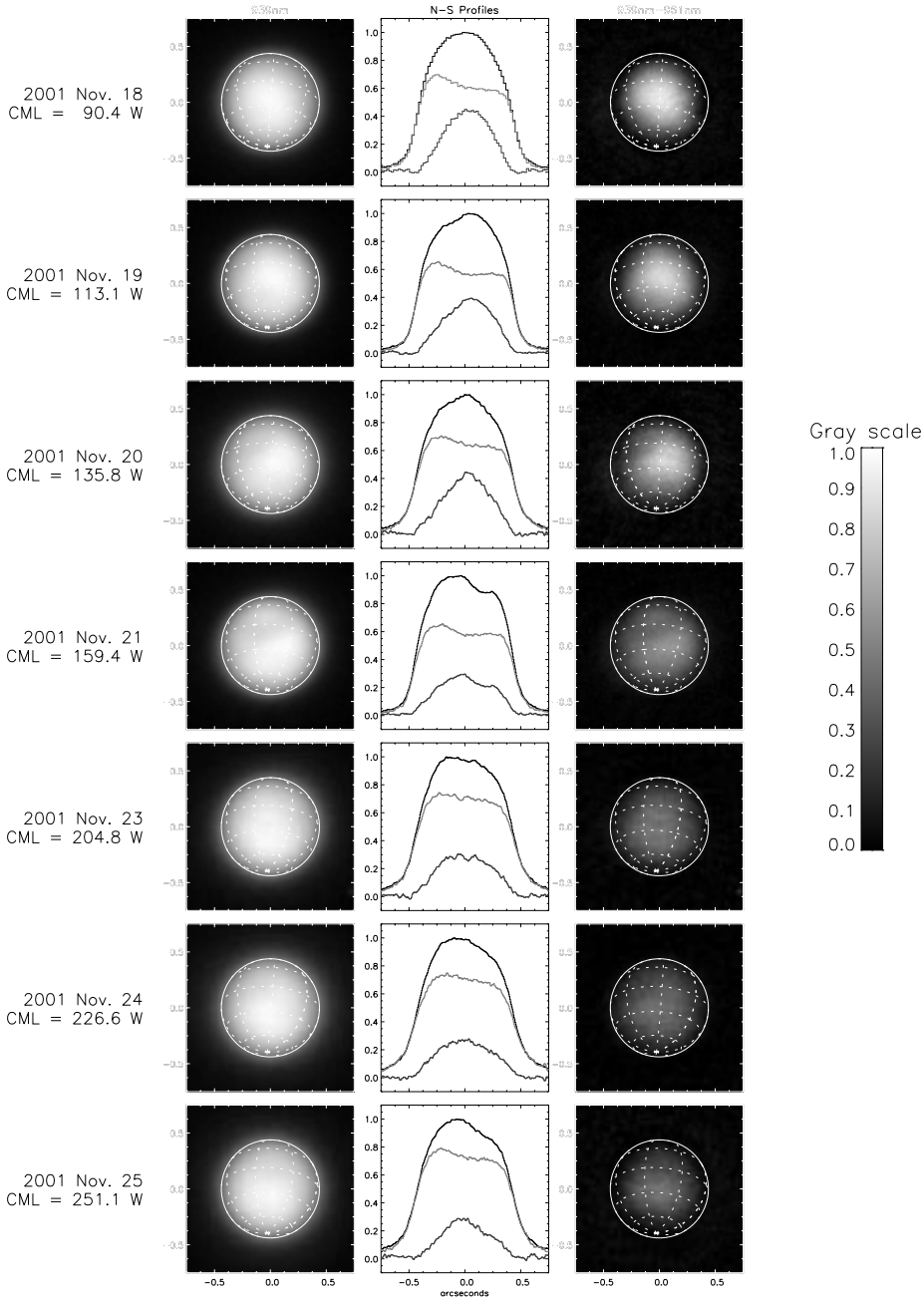

Figure 2.6: Subtraction of atmosphere-only 960-nm images from those at 940 nm sensitive to Titan's surface reveals surface albedo features. *Left*: Nightly mean 940-nm images taken on 7 of 8 consecutive nights in November 2001. Images have been scaled individually. *Middle*: North-south (celestial) relative intensity profile across the center of Titan's disk at 940 (top, dark line) and 960 nm (middle gray line, scaled to give zero mean residual beyond the physical edge of Titan's disk). Lower dark line shows north-south profile of subtracted image, which consists only of photons scattered within ~ 20 km of Titan's surface. *Right*: $(940 - 960)$-nm subtracted images, on a common relative intensity scale.

this requirement and normalize by the radiance observed when that location is viewed at its lowest emission angle, and limit the analysis to those locations observed at least once at $< 30^\circ$ emission angle.

The normalized radiances at every location on Titan fulfilling the above requirement are shown in Fig. 2.7 as a function of emission angle, and define the effective phase function of Titan's surface for these observations. The normalization by non-zero phase observations adds noise to this estimate of the effective phase function, as does the photometric variability of the images due to telluric H_2O. We can nevertheless use these normalized radiances to constrain the coefficient of a Minnaert scattering law of form $I_\mu/I_0 = \mu^k \mu_0^k$, where I_μ/I_0 is the normalized radiance, μ is the cosine of the emission angle, and μ_0 the cosine of the solar zenith angle. Since the observations were performed near Titan opposition, we assume $\mu_0 \approx \mu$, leading to the simplified Minnaert law $I_\mu/I_0 = \mu^{2k}$. We find that $k = 1.05 \pm 0.25$ is consistent with the observed phase behavior of Titan's surface and therefore adopt $k = 1$ in the subsequent analysis. We ascribe no physical significance to this description of the phase function, since it includes the effects of the true phase function of Titan's surface, the opacity of the overlying atmosphere, and the reduction in contrast due to light in the halo of the PSF. However, it serves the purpose of describing the apparent photometric behavior of Titan's surface as a function of emission angle, allowing us to combine nightly haze subtracted images of uncertain relative photometry into a map of the relative surface albedo seen at zero phase.

We use a slight modification of the technique of Smith *et al.* (1996) to fit for the relative albedo at each location on our latitude-longitude grid, while simultaneously solving for the relative photometric scaling factor of each input nightly mean image. For each position i on the latitude-longitude grid, we take the best estimate of the radiance at zero phase angle $I_{0,i}$ to be that which minimizes the reduced χ^2

$$(\chi^2)_i = \frac{\sum_j (I_{0,i}\mu_{ij}^2 - \alpha_j I_{ij})^2 (\alpha_j \sigma_{ij})^{-2}}{(N-1)}, \tag{2.2}$$

where μ_{ij} is the cosine of the emission angle at location i in image j, α_j is the unknown photometric scaling factor for image j, and I_{ij} and σ_{ij} are the observed uncorrected radiance

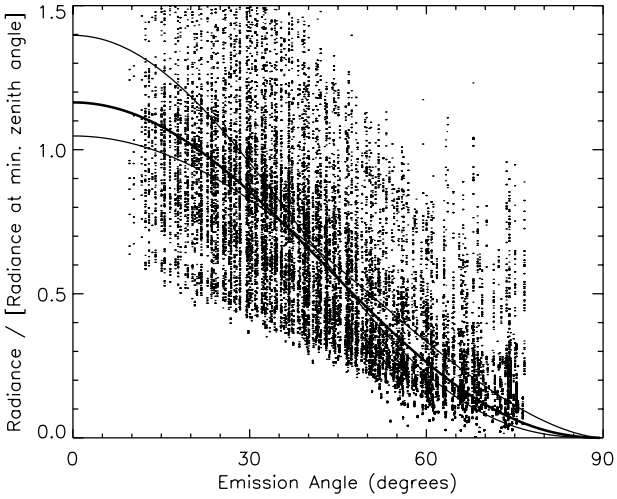

Figure 2.7: Radiance of Titan's disk in nightly mean images from November 2001, divided by the radiance at that point on the night at which it was observed at minimum emission angle. Only points for which the minimum emission angle was less than 30° are included. The large vertical scatter is due to uncertain photometric calibration of the individual images, and the range in minimum emission angles included. Nevertheless, a Minnaert power law of form $I = I_0 \mu^k \mu_0^k$ can be fit in a least-squares sense to constrain the exponent $k = 1.05 \pm 0.25$ (range is shown as thin lines).

and uncertainty at location i in image j. χ^2 will be minimized when

$$I_{0,i} = \frac{\sum_j \alpha_j^{-1} I_{ij} \mu_{ij}^2 \sigma_{ij}^{-2}}{\sum_j \alpha_j^{-2} \mu_{ij}^4 \sigma_{ij}^{-2}}, \tag{2.3}$$

where the sums are taken only over the images in which the location i is viewed at less than some maximum emission angle, here taken to be 60°.

We solve for the photometric scaling factors α_j iteratively, by requiring that the residuals in each image of Titan's surface after subtraction of the surface model to have a mean of zero. We start with an initial estimate $\alpha_j = 1$, compute $I_{0,i}$ using Eq. 2.3, then update our estimates of the photometric scaling factors as

$$\alpha_j' = \alpha_j \frac{\sum_j (I_{ij} \mu_{ij}^2 / I_{0,i})}{N}, \tag{2.4}$$

where the sum is taken over the N pixels in image j in which Titan's surface is viewed at less than 60° emission angle. Repeating this procedure, $I_{0,i}$ and α_j are found to converge rapidly

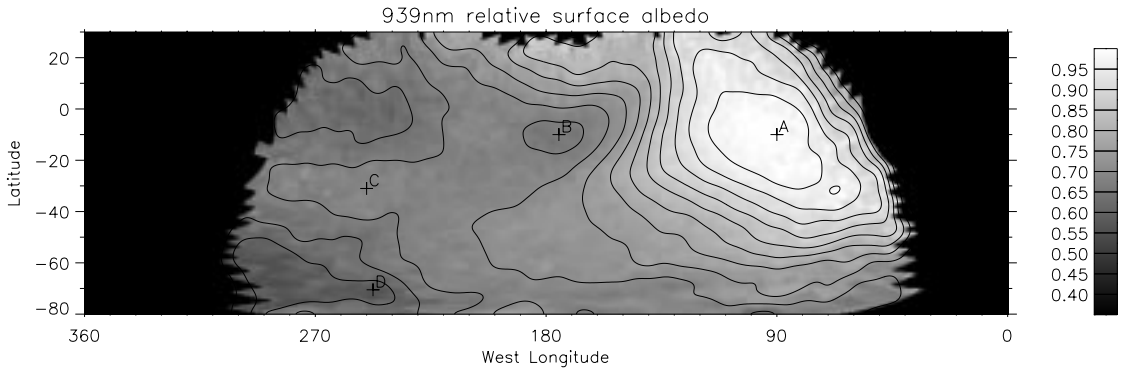

Figure 2.8: Map of the 940 nm relative surface albedo for regions observed in 2001 at less than 60° emission angle in a minimum of two images. Marked locations correspond to photometry in Fig. 2.10.

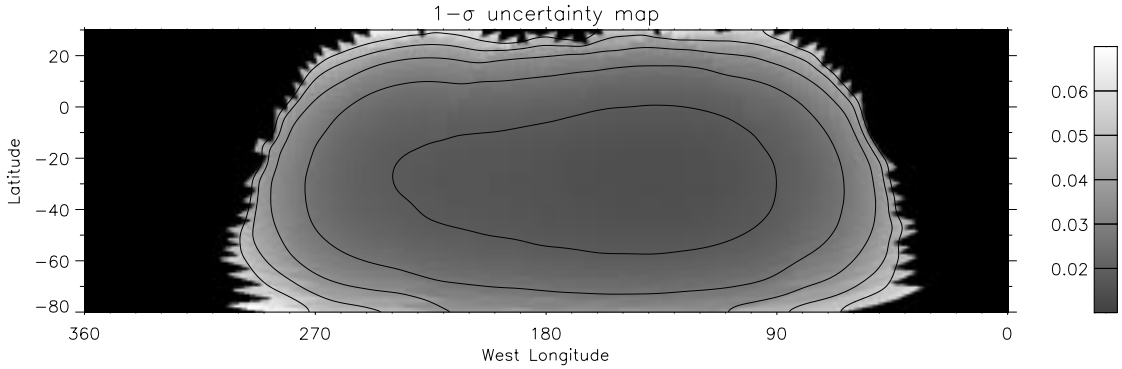

Figure 2.9: Map of statistical uncertainty in 940 nm relative albedo map of Titan (Fig. 2.8).

(in 3–5 iterations) to values which minimize both the differences between the predicted and observed radiance at each location of Titan, and the absolute value of the mean residuals in each nightly image.

The relative radiance at zero phase I_0 derived by this procedure, though not absolutely calibrated, is proportional to Titan's surface albedo. Figure 2.8 presents our map of Titan's relative surface albedo at 940 nm, normalized to the brightest location observed (at 90°W, 10°S). Only locations on Titan viewed on a minimum of 3 nights with an emission angle of less than 60° are included. A map of the uncertainty of the relative albedo estimate, is displayed in Fig. 2.9. The corrected radiances $\alpha_j I_{ij}$ measured at 4 representative locations on Titan's surface are shown in Fig. 2.10, along with the phase functions fit to those radiances. Note the generally good fit of the $I = I_0\mu^2$ phase function to the corrected

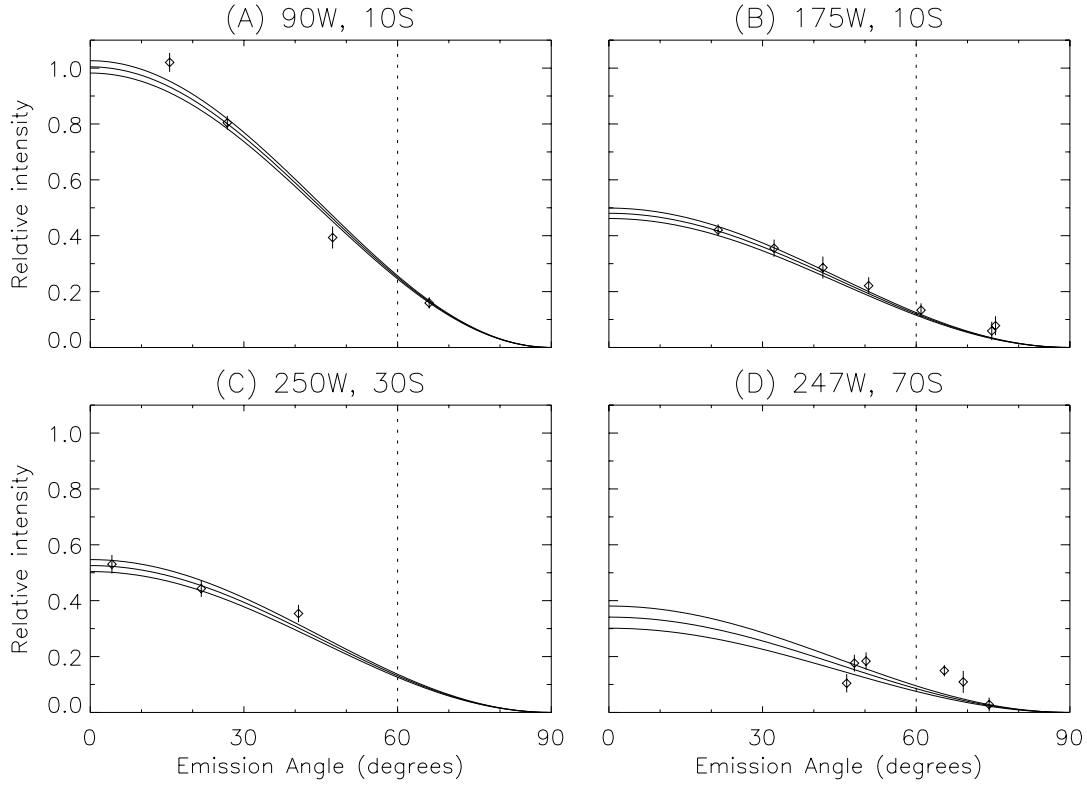

Figure 2.10: Corrected photometry of four representative locations on Titan, with their $I = I_0\mu^2$ models overplotted. Locations are marked in Fig. 2.8. 1-σ error bars are shown for photometry and model fit.

radiances at emission angles of less than 60°. Radiances measured at emission angles greater than 60° are included in Fig. 2.10, but were never used in the fitting procedure.

Titan's surface displays complex and surprisingly strong albedo contrasts. Many of the features visible in Fig. 2.8 have previously been noted in visible (Smith *et al.*, 1996) and near-infrared (Combes *et al.*, 1997; Gibbard *et al.*, 1999; Meier *et al.*, 2000; Coustenis *et al.*, 2001) images of Titan. Titan's leading hemisphere is dominated by a large high albedo region, centered near 100°W, 10°S. Sometimes referred to as Titan's continent, this region appears bright at all wavelengths thus far sampled, leading to the suggestion that it may be a highland terrain whose surface is washed free of dark hydrocarbons by meteorological processes (Smith *et al.*, 1996).

Significant extensions of this bright terrain to the north-west (to 180°W, 25°N) and south-east (to at least 50°W, 40°S) can be seen in Fig. 2.8. The north-western extension has been described by all previous authors, but the south-eastern extension appears to be

missing in several of the maps. As pointed out by Combes *et al.* (1997), the subtraction of a zonally averaged image by Smith *et al.* (1996) may have led to the loss of real surface features if certain latitudes are on average brighter or darker than others. This appears to have occurred at 20°S–40°S, where both our 940 nm map and those at 1.3, 1.6, and 2.0 μm (Combes *et al.*, 1997; Coustenis *et al.*, 2001) made without the subtraction of a zonally averaged image show a high albedo region extending most of the way around Titan. Thus, a bright band running across Titan's southern face (from 180°W to at least 300°W) lines up with the southern extension of the bright terrain, leading to the accidental subtraction of both these features in the surface maps of Smith *et al.* (1996) and Meier *et al.* (2000).

Besides the discrepancies in the 20°S–40°S latitude band, most features in the 940 nm relative albedo map displayed in Fig. 2.8 coincide with those noted by previous authors. The north-western extension of the bright terrain is resolved into a distinct bright feature centered at 180°W, 25°N. To the west and south of this bright peninsula lies the mostly dark trailing hemisphere of Titan. At the $\sim$ 700 km resolution achieved by these observations, the darkest regions mapped appear 40% the albedo of the bright terrain, consistent with the even higher contrast observed at higher spatial resolution in the near-infrared (Gibbard *et al.*, 1999; Coustenis *et al.*, 2001).

2.4 Conclusions

Observations combining high spatial, spectral, and temporal resolution are necessary to further our understanding of Titan's dynamic atmosphere and mysterious surface. The images presented here, acquired with the AEOS telescope and 5 custom narrow-band filters, provide an example of one technique which achieves this goal. The $\sim$ 700 km spatial resolution achieved by this system on Titan is sufficient to study global-scale haze and cloud structures in Titan's atmosphere, though it is not high enough to detect individual convective clouds in the troposphere. Narrow-band filters sampling the edge of a CH_4 band with a spectral resolution of $\lambda/\Delta\lambda \approx 100$ provide a convenient method of vertically discriminating atmospheric and surface features.

Titan's atmosphere undergoes substantial seasonal changes, which as a whole remain poorly understood. As Titan's southern summer solstice approaches in October 2002, the highest haze continues to move north across the equator, causing the southern hemisphere

to appear darker at wavelengths of strong CH_4 absorption in 2001 than in 2000. This is consistent with the high aerosols being transported by a thermally direct pole-to-pole meridional circulation pattern, predicted by general circulation models of Titan's atmosphere (Hourdin *et al.*, 1995; Tokano *et al.*, 1999). The lower regions of the main haze layer appear uniform at 960 nm, and it is not known whether they are similarly affected by a meridional transport mechanism.

The bright scattering region near the tropopause in Titan's high southern latitudes appears to have undergone little change between 2000 and 2001. One possible origin of this feature is the condensation of ethane and methane onto precipitating C_4N_2 ice, formed in the lower stratosphere when temperatures reach their minimum near spring equinox (Samuelson *et al.*, 1997). The persistence of this feature argues against this, however, since lower stratospheric temperatures are expected to rise rapidly as summer solstice approaches in November 2002.

Alternately, the southern scattering layer may be more analogous to tropical cirrus on Earth. Methane could be highly supersaturated at the south polar tropopause during late southern spring on Titan, due to the rising motion accompanying the expected pole-to-pole global meridional circulation. On Earth, such regional uplift due to Hadley circulation leads to widespread tropical cirrus, which may nucleate either homogeneously or heterogeneously (Kärcher, 2002). Spatially resolved spectroscopy of Titan's atmosphere in the near-infrared constrains the southern scattering layer to have an optical thickness of $\tau \approx 0.05$ (Ch. 3), reinforcing the analogy to terrestrial cirrus.

The map of Titan's relative surface albedo at 940 nm which we present in Fig. 2.8 is the first at visible wavelengths created without the subtraction of zonally averaged images. Some discrepancies are noted between this map and the somewhat higher resolution maps assembled from HST images in the visible (Smith *et al.*, 1996) and near-infrared (Meier *et al.*, 2000). These differences are most likely due to the unintentional subtraction from the HST maps of a series of high albedo features which encircle Titan at 20°S–4°S. These features were also noted by Combes *et al.* (1997) at 2 μm, who suggested that they might form the northerly boundary of a bright southern polar cap. The present more southerly view allows us to rule out the existence of an extensive bright southern polar cap at 940 nm.

Though Titan's surface has now been mapped at wavelengths from 940 nm to 2 μm, the source of the static albedo variations remains a mystery. Water ice, perhaps washed clean

by meteorological processes, is generally assumed to be responsible for high albedo features (Griffith *et al.*, 1991; Smith *et al.*, 1996), while both liquid and solid hydrocarbons and atmospheric sediments are probably responsible for darkening other regions of the surface (Lunine *et al.*, 1983; Gibbard *et al.*, 1999). Though measured albedos are consistent with these compositions, no unambiguous evidence has yet been uncovered for either.

Chapter 3

Spatially resolved spectroscopy of Titan

3.1 Introduction

While the Voyager 1 flyby of Titan in 1980 established the structure and composition of Titan's atmosphere (Lindal *et al.*, 1983), little could be distinguished below a thick layer of haze which fills the stratosphere. The haze is the end-product of the photolysis of N_2 and CH_4, the two most common atmospheric constituents (Kunde *et al.*, 1981; Yung *et al.*, 1984). Although the main haze layer was optically thick to Voyager's visible-light cameras, some structure was clearly apparent in its uppermost regions, such as a detached global haze layer at 300–350 km altitude, a north polar hood, and a pronounced hemispheric albedo contrast (Smith *et al.*, 1981; Rages and Pollack, 1983). The hemispheric brightness asymmetry appears to alternate seasonally (Caldwell *et al.*, 1992; Lorenz *et al.*, 1997, 1999, 2001), consistent with transport of haze across Titan's equator by thermally direct winds (Sromovsky *et al.*, 1981; Hutzell *et al.*, 1996). Thus it appears that Titan's haze distribution is shaped by both the latitude-dependent environment of the stratosphere, and by dynamical transport of aerosols. An important recent advance in understanding the haze distribution has been the coupling of a microphysical haze production model (McKay *et al.*, 2001) with a global circulation model which takes into account the radiative properties of the haze, which together reproduce many of these observed features (Rannou *et al.*, 2002).

Observations through near-infrared spectral windows in Titan's atmosphere have now revealed a complex surface (Smith *et al.*, 1996; Combes *et al.*, 1997; Gibbard *et al.*, 1999; Meier *et al.*, 2000; Coustenis *et al.*, 2001) and transient CH_4 clouds near Titan's south pole

(Griffith *et al.*, 1998, 2000; Brown *et al.*, 2002; Roe *et al.*, 2002), yet the distribution of haze and long-lived clouds in the troposphere is poorly constrained. Titan's surface must provide the ultimate sink for the haze, but it is unclear whether condensation of CH_4 on the aerosols once below the tropopause (at 40 km altitude) might increase their fall velocity and clear out the region, or whether condensation is inhibited for kinetic or chemical compatibility reasons (McKay, 1996; Samuelson and Mayo, 1997; Samuelson *et al.*, 1997). If rain-out of the haze does occur, it is possible that the CH_4 would re-evaporate before reaching the surface, leaving a separate low aerosol layer (Lorenz, 1993).

Two recent observational studies have attempted to map the distribution of haze and clouds in Titan's lower stratosphere and troposphere. Young *et al.* (2002) analyzed narrow-band 890–950 nm Hubble Space Telescope (HST) images, using the strongly varying CH_4 absorption over this spectral region to constrain the altitude structure of the haze in the lower stratosphere and troposphere. They find an apparent gap in the haze at 16–32 km altitude, underlain by an optically thick region between the surface and 16 km. However, the apparent presence of this lower haze layer is likely to be a consequence of their assumption of a zero-albedo surface, since its claimed thickness correlates closely with the actual surface albedo distribution (Fig. 6.5). Chanover *et al.* (2003) provide further evidence for a relatively clear atmosphere below 30–60 km altitude in Titan's equatorial region.

Understanding the vertical distribution of haze and other condensates in Titan's lower atmosphere provides insight into the seasonally varying circulation patterns, and proves critical to correctly interpreting near-infrared images of Titan's surface (Ch. 6). We present in this chapter the first spatially resolved near-infrared spectra of Titan's atmosphere and surface, acquired with the Palomar Hale telescope adaptive optics (AO) system and PHARO spectrograph between September 1999 and December 2001. Spatially resolving Titan's disk provides spectra of each latitude at a variety of emission angles, from which we determine both the vertical distribution of aerosols and condensates, and the underlying surface albedo. Though the spatial resolution of these data is not sufficient to resolve the small transient clouds recently discovered near Titan's south pole (Brown *et al.*, 2002; Roe *et al.*, 2002), a broad region of high clouds is noted at high southern latitudes.

Sections 3.2 and 3.3 present in detail our observing strategy and the steps required to process and calibrate AO-corrected spectra, with the goal of providing a useful resource for future users of the Palomar AO system. Sections 3.4 describes our analysis of these

spectra, by which we determine the three-dimensional haze and cloud structure of Titan's atmosphere and the surface albedo distribution, presented in Section 3.5. Finally, Sec. 3.6 discusses the implications for Titan's global atmospheric circulation, the physical conditions in the troposphere, and Titan's surface composition.

3.2 Observations

Spectra of Titan were obtained on 26 September 1999, 20 July 2000, and 20 December 2001 UT using the JPL AO system and the Cornell-built PHARO camera/spectrograph at the Cassegrain focus of the Hale 5-m telescope. The AO system consists of a Shack-Hartmann sensor ($\lambda < 1.05$ μm) controlling a fast tip-tilt mirror and a 241-active element deformable mirror, which together partially correct atmosphere-induced wavefront aberrations of the $\lambda > 1.05$ μm science beam (Dekany, 1996). Titan itself ($V \approx 8.2$) provided the reference source for these observations, allowing the deformable mirror to be run at a closed-loop servo bandwidth of ~ 20 Hz (500 Hz update rate). The PHARO near-infrared camera (Hayward *et al.*, 2001) was used to record both broad-band images and medium-resolution spectra of Titan. Images were taken through either a K-prime (K′, 1.945–2.296 μm) or K-short (K_s, 1.990–2.300 μm) filter, and recorded with the 1024×1024 pixel Rockwell HAWAII HgCdTe array detector at a platescale of $0\farcs0252$ pix^{-1} (Metchev *et al.*, 2003). To acquire AO-corrected spectra, an $0\farcs13 \times 40''$ slit was placed in the focal plane near the entrace to the PHARO camera, and a grism used to disperse the beam onto the same detector at a spectral resolution of $\lambda/\Delta\lambda = 1800$ over the wavelength range 2.03–2.37 μm, at a spatial platescale of $0\farcs040$ pix^{-1}. The 20 July 2000 and 20 December 2001 observations recorded only the wavelength range 2.10–2.32 μm, due to a mistaken choice of the $0\farcs0252$ pix^{-1} platescale mode of the instrument.

The observing sequence was dictated by the need to reconstruct the pointing of each spectrum after the fact, and to maintain the spectral stability of PHARO throughout the observations. Before each set of Titan spectra, 4 to 16 dithered K′ or K_s images of Titan with an integration time of 9.1 s were first acquired. These were used to estimate the point spread function (PSF) and the pointing of the subsequent spectra.

Since PHARO does not provide a slit-viewing capability, spectra are typically acquired by centering on the target in imaging mode, then moving the slit and grism into the optical

Table 3.1: Palomar AO spectroscopic observations

UT date	Time	Target	Type	Spectral range[a]	Airmass	Diam.[b]	Sub-Earth[c]
26 Sep 1999	07:17–07:24	Titan	imaging	K′	1.47–1.43	0.84	55.5, −20.6
26 Sep 1999	07:58–08:11	Titan	spectra	2.03–2.37	1.29–1.25	0.84	56.2, −20.6
26 Sep 1999	08:41–08:44	HD 1461	spectra	2.03–2.37	1.37–1.38	-	-
26 Sep 1999	09:16–09:35	Titan	spectra	2.03–2.37	1.10–1.08	0.84	57.4, −20.6
26 Sep 1999	10:03–10:13	Titan	spectra	2.03–2.37	1.06–1.06	0.84	58.1, −20.6
20 Jul 2000	11:40–11:48	HD 20065	spectra	2.10–2.32	1.51–1.46	-	-
20 Jul 2000	11:57–11:59	Titan	imaging	K′	1.62–1.61	0.74	295.2, −23.8
20 Jul 2000	12:05–12:09	Titan	spectra	2.10–2.32	1.56–1.55	0.74	295.4, −23.8
20 Jul 2000	12:28–12:32	HD 17163	imaging	K′	1.34–1.33	-	-
20 Jul 2000	12:32–12:34	HD 17163	imaging	K_s	1.32–1.32	-	-
20 Jul 2000	12:39–12:41	HD 22686	imaging	K_s	1.57–1.56	-	-
20 Jul 2000	12:41–12:44	HD 22686	imaging	K′	1.56–1.55	-	-
20 Jul 2000	12:51–12:53	Y5546	imaging	K′	1.79–1.80	-	-
20 Jul 2000	12:53–12:55	Y5546	imaging	K_s	1.80–1.81	-	-
20 Dec 2001	06:33–06:37	Titan	imaging	K_s	1.03–1.03	0.87	92.5, −25.5
20 Dec 2001	07:07–07:34	Titan	spectra	2.10–2.32	1.04–1.06	0.87	93.2, −25.5
20 Dec 2001	07:50–07:55	HD 32923	spectra	2.10–2.32	1.06–1.06	-	-
20 Dec 2001	09:22–09:51	Titan	spectra	2.10–2.32	1.32–1.46	0.87	95.3, −25.5
20 Dec 2001	09:59–10:05	HD 32923	spectra	2.10–2.32	1.36–1.38	-	-

a. Recorded spectral range (μm) or filter name.
b. Apparent diameter of Titan ($''$).
c. West longitude and latitude of the sub-Earth point ($^\circ$).

path. However, the position angle of the entrance slit and the orientation of the grism are not precisely reproducible after such moves. In most cases, we therefore acquired all spectra in a given set (Titan, sky, calibrator star, sky) without moving either the slit or grism. To accomplish this, Titan was initially centered $0\farcs6$ to the east of the measured slit location while in imaging mode. The slit (with a position angle of $0^\circ \pm 2^\circ$) and grism were then installed, and the first of a set of 120-s spectral integrations was begun. After each integration, the telescope was commanded $0\farcs10$ or $0\farcs12$ east, and the next integration begun, thus gradually sampling every location on Titan's disk. Several effects lead to uncertainty in the actual offset between spectra, the most important being differential flexure between the science and wavefront-sensing light paths on the AO bench. This causes AO targets to drift linearly on the PHARO focal plane, at a rate of $\sim 0\farcs0002$ s^{-1}. Depending on the direction of the drift, Titan's disk was covered in 8–12 pointings.

After scanning the slit across Titan's disk, the telescope was offset $60''$ north or south of Titan and several night-sky spectra with the same integration time were obtained. These were used to correct the detector bias, dark current, and atmospheric thermal and line emission recorded in the Titan spectra. With the slit and grism still in place, the telescope was slewed to a nearby solar analogue star (spectral class G0–G5, within 3° of Titan), and

several 60-s spectra of the star acquired with the AO feedback loops open. Finally, the telescope was offset 60″ and several 60-s night-sky spectra were recorded, for calibration of the solar analogue spectra.

The entire observing sequence was repeated twice on both 26 September 1999 and 20 December 2001. A more limited set of observations was taken on 20 July 2000, consisting only of an imaging sequence, three 120-s spectra with the slit centered on Titan's central meridian, and calibration spectra. The grism and slit were also accidentally moved between Titan and calibrator star observations on that night, resulting in poor correction of the interference fringes which are superimposed on all spectra.

The observing conditions were photometric on 26 September 1999 and 20 July 2000 and marked by variable thin cirrus on 20 December 2001. Immediately following the Titan observations, three bright photometric standard stars (HD 17163, HD 22686, and Y 5546) were imaged on 20 July 2000. The AO feedback loop was left open to avoid saturation and 5 1.8-s images, in each of 4 positions on the detector, were acquired of each star through both K′ and K_s filters. A summary of the observations is given in Table 3.1.

3.3 Data reduction

3.3.1 Images

Standard near-infrared image processing techniques were applied to the Titan images. Each set of dithered images was first grouped according to the location of Titan on the detector. For each location, a pixel-by-pixel median of the images not included was calculated and subtracted from each image in this subset, thus correcting for the detector bias, dark current, and the sky background. All images were then divided by a map of the relative pixel gains (the flat-field map), which was calculated from the average of bias and dark current subtracted twilight sky images taken through the appropriate filter on the same night. Finally, pixels with abnormal gain properties, as determined from twilight sky images taken over a wide range of sky brightness, were replaced by the median of the surrounding good pixels.

The geometric center of Titan's disk was next determined for each image in the set. The technique found to be most accurate at the high signal-to-noise ratio (SNR) of these broad-band images (> 150 pix^{-1} on the disk) was to fit a circle to Titan's limb. All

pixels within 1% of one-half the peak intensity of the disk were identified, and the sum of the squares of the distance between the center of these pixels and the nearest point of a circle was numerically minimized, solving for the circle's position and radius. Monte-Carlo simulations of the technique demonstrate that at this SNR, the median random error in the determination of the disk of the disk center is 0.05 pix (1 milliarcsecond, mas). The actual uncertainty in Titan's position on the detector is therefore dominated by systematic effects, particularly the presence of high contrast features on Titan's disk. The feature capable of inducing the strongest centering bias would be a hemispheric albedo contrast, due either to surface albedo or the haze distribution. We estimate the systematic centering error by constructing a model of Titan's disk with the strongest hemispheric contrast consistent with each recorded images, convolving this synthetic image with the estimated PSF (see Sec. 3.4.3) and calculating the apparent shift in the disk center. This leads to an upper limit in the systematic centering error of 0.9 pix (23 mas) for the 26 September 1999 images, which display a strong east-west albedo contrast, 0.7 pix (18 mas) on 20 July 2000, and 0.4 pix (10 mas) on 20 December 2001.

With Titan's location determined, the images were shifted to a common center by adding a phase ramp to the Fourier transform, then transforming back to the image domain. This technique allows one to perform a sub-pixel shift while keeping the power spectrum of the image unchanged. The shifted images were then averaged to produce three nightly-mean images of Titan, displayed in Figure 3.1.

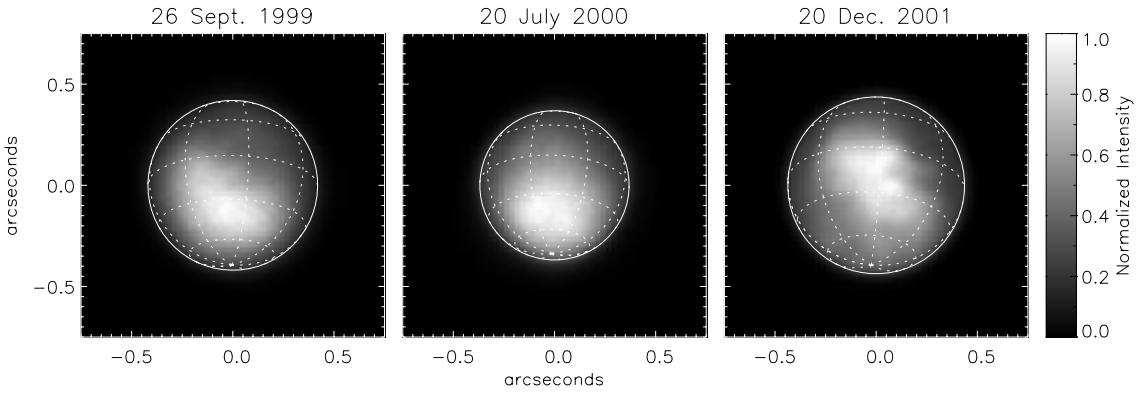

Figure 3.1: Broad-band K_s and K' images of Titan on the three nights of observation. Each image has been scaled independently to highlight subtle surface albedo patterns. Titan's varying size and perspective are indicated by lines of latitude every 30° and longitude every 45°.

The initial processing steps applied to the photometric standard star images taken on 20 July 2000 were identical to those applied to the Titan images. However, rather than centering and averaging the images, the sum of the detector counts within a $10''$ radius of the centroid was determined for each frame, and the mean of these values used to establish the apparent instrumental flux of each star. The photometric zero-point and extinction per unit airmass in both K' and K_s were then determined by fitting the three standard star observations, allowing us to photometrically calibrate the 20 July 2000 Titan images to an accuracy of 5% . The same photometric factors were applied to the 26 September 1999 K' and 20 December 2001 K_s images for which no standard stars were observed, but the resulting calibration is only approximate.

3.3.2 Spectra

The process of transforming raw two-dimensional spectra of Titan and a solar analogue star to calibrated albedo spectra of known locations on Titan's disk required the following general steps. The precise alignment of the slit and grism relative to the detector, and the wavelength scale of each set of observations, were first determined from summed raw spectra. Each Titan and stellar spectrum was then corrected for detector, instrumental, and atmospheric effects, and the one-dimensional spectrum of Titan at each location along the slit extracted and divided by the stellar spectrum. Finally, the pointing location and photometric corrections of each Titan spectrum were determined by cross-correlating the image recorded through the slit with broad-band images taken the same night.

Spectra acquired with the PHARO camera are dispersed along the x-axis of the detector, with the projection of the entrance slit falling roughly parallel to the y-axis. Following movements of the silt and grism wheels, however, the alignment of these optical elements in PHARO can be uncertain by up to several degrees. Additionally, the projection of the slit on the PHARO detector is somewhat curved by optical distortions. Atmospheric OH emission lines recorded in long-exposure spectra provide a convenient fiducial with which to measure the slit angle and curvature. To maximize the SNR of the sky lines, we subtracted a mean of several 120-s dark frames from every Titan and night-sky spectrum in each set of observations, and averaged these dark-subtracted frames. The mean trace of the sky lines was then determined by cross-correlating each row of the resulting image with an arbitrary row near the center of the detector (ignoring the portion of the slit occupied by Titan),

then fitting a second order polynomial in relative offset x as a function of row y.

A similar procedure was used to measure the alignment of the grims with respect to the detector, and the optical distortion in the spectral dimension. A mean of the 60-s night-sky spectra taken immediately after the calibrator star observations was first subtracted from each stellar spectrum. All corrected calibrator star spectra in a set of observations were then averaged, and each column of the resulting image was cross-correlated with the central column. A second-order polynomial was then fit to the relative offsets in y as a function of column x.

A third step performed prior to the processing of individual Titan and calibrator star spectra was to determine the wavelength scale of each set of observations from the OH emission lines. The average of all dark-subtracted Titan and night-sky integrations was resampled using bilinear interpolation to cancel the measured slope and curvature in both axes. A high SNR sky spectrum was calculated by averaging all rows greater than $2''$ from Titan's location on the slit, and the locations of the 6 brightest emission lines determined by fitting one-dimensional Gaussian functions to them. A linear wavelength scale was finally fit to the locations and known wavelengths (Chamberlain and Smith, 1959) of these OH emission lines.

Following these preliminary steps, each Titan and calibrator star spectrum was processed individually. Spectra were first checked for cosmic rays, and the affected pixels replaced by the median of the surrounding good pixels. The 2–5 120-s night-sky integrations taken immediately after the Titan spectra were averaged, and this mean sky spectrum subtracted from Titan frame. Similarly, a mean of 60-s sky spectra was subtracted from each calibrator star integration. This step corrected for the detector bias and dark current, as well as subtracting the line and thermal sky emission which are superimposed on the target spectra. All spectra were next divided by the same K_s or K' flat-field map used for that night's images, correcting the detector's pixel-to-pixel gain variations. Bad pixels were replaced by the median of the surrounding values.

Both the Titan and stellar spectra were next resampled to align the spatial and spectral axes with the detector y and x axes. As was the case for the wavelengths scale determination, this resampling was done with the origin (the location at which the shift in both dimensions was zero) near the middle of Titan's spectrum, thus minimizing the loss of spatial and spectral resolution caused by the bilinear interpolation of adjacent pixel values. Some

residual sky emission remained visible in the Titan spectra at this stage, due to the changing atmospheric conditions during the observations. The residual sky emission was determined by averaging the spectrum 2″–4″ to either side of Titan along the slit, and subtracting this residual spectrum from each row. This step was not necessary for the higher SNR stellar spectra.

The processed calibrator star frames were averaged, and a one-dimensional stellar spectrum extracted by taking the mean over all illuminated rows, weighted by the relative flux in that row. By dividing every row of the Titan spectra by this spectrum of a solar analogue taken under identical conditions, the spectrally variable instrumental and atmospheric response were calibrated out, leaving Titan spectra in units proportional to albedo. In particular, strong interference fringes are present in the uncalibrated spectra, superimposed on both the Titan and stellar spectra due to monochromatic internal reflections in the detector. Division by the solar analogue spectrum successfully eliminates the fringes if the grism and slit were not moved between Titan and stellar observations. Some fringes remain in the 20 July 2000 Titan spectra due to the very slight ($\sim$ 1 pix) mis-match in wavelength between Titan and calibrator star spectra.

Each row of the processed Titan spectra records the spectrum at one location along the entrance slit. Since the detector platescale oversamples the diffraction-limited spatial resolution of the Hale telescope, spectra were next averaged along-slit by a factor of 2–3, leading to a final spatial sampling of 0.″080 on 26 September 1999 and 0.″076 on 20 July 2000 and 20 December 2001. The uncertainty in the spectra due to electronic and photon noise was estimated from the the full range of the pixel values included in the spatial average at each wavelength.

The final step of the reduction sequence was to determine the pointing location of each spectrum with respect to the center of Titan's disk, by comparing the spectrum recorded through the slit with the K′ or K_s images taken the same night. As noted previously, the telescope was commanded 0.″10 or 0.″12 east between each Titan integration, but flexure of components on the AO bench and inaccurate control of the articulated mirrors which direct light to the wavefront sensor caused this offset to be uncertain. Experiments performed with an internal calibration source demonstrate that the gradual drift of the AO corrected image on the PHARO focal plane due to flexure is linear on timescales of an hour or less. The effect of inaccurate steering mirror control is less well constrained, but probably contributes

random offsets between spectra of less than 0.″02. The sum of the commanded offset and the gradual $\sim 0.''0002\ s^{-1}$ drift due to flexure therefore causes Titan to follow a nearly linear trajectory across the entrance slit.

Each Titan spectrum was multiplied by the imaging filter transmission function, and summed over wavelength to produce one-dimensional images of Titan as seen through the 0.″13-wide entrance slit. The iterative routine AMOEBA (Press *et al.*, 1992) was then used to minimize the square of the difference between the set of slit images and the nightly broad-band image, assuming a linear offset between successive spectra. Five parameters were solved for: the location of the slit center with respect to that of Titan for an arbitrary spectrum (2 parameters), the offset in arcseconds between successive spectra (2 parameters), and a photometric scaling factor. This scaling factor, corrected for the flux admitted by the imaging filter but not sampled by the spectra which we calculated from the disk integrated spectra of Fink and Larson (1979), allowed us to photometrically calibrate the Titan spectra to match the calibrated images. The sets of central meridian spectra taken on 26 September 1999 and 20 July 2000 were navigated in a similar fashion, solving for only 3 parameters: the north-south position, drift rate, and photometric scaling factor. Finally, several of the individual spectra taken on 20 December 2001 were clearly affected by passing terrestrial clouds. The procedure was modified for these data, allowing the minimization algorithm to correct the photometry of each slit image independently. Those spectra whose apparent flux was reduced by more than a factor of two (located along Titan's western limb) were excluded from the analysis.

3.4 Analysis

3.4.1 Spectral diversity

Titan's near infrared albedo results largely from the absorption of solar radiation by CH_4 and H_2, and scattering of radiation from particles (both photochemically produced haze and possibly from condensate clouds) and from the surface. We use the strongly wavelength-dependent absorption features of methane in Titan's atmosphere as a vertical filter with which we can resolve the altitude of hazes and clouds. Deep in the saturated absorption band at 2.17–2.25 μm, only sunlight scattered off haze in Titan's stratosphere is detected. Shorter wavelengths sample progressively deeper levels of the atmosphere, allowing scattering in the

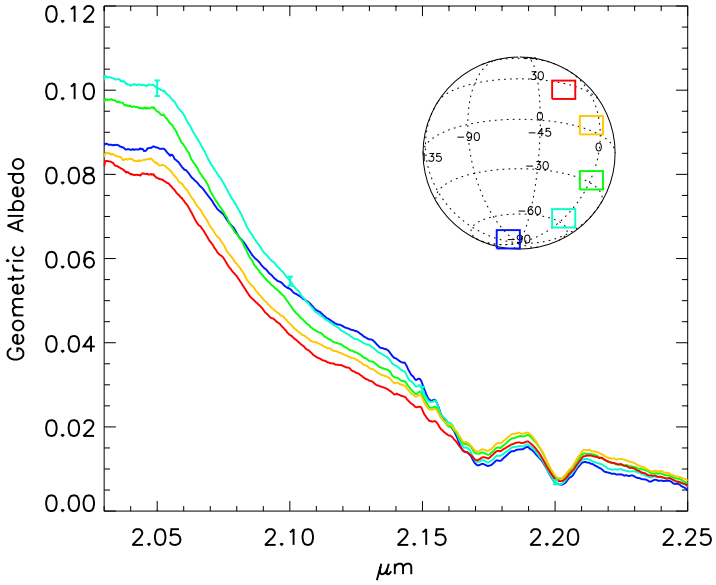

Figure 3.2: Five spectra of Titan's disk on 26 September 1999, chosen to sample similar incidence angles through Titan's atmosphere at a variety of latitudes. They have been smoothed for clarity. Equatorial spectra are brightest deep in the 2.25 μm absorption band, indicating a thicker stratospheric haze layer above the bulk of Titan's atmospheric methane. Spectra at high southern latitudes, in contrast, rise steeply on the edge of the methane band (from 2.17 to 2.12 μm), revealing a region of enhanced scattering deep in Titan's atmosphere, yet distinct from variations in surface albedo which dominate the spectra shortward of 2.12 μm.

troposphere to affect the flux shortward of 2.17 μm, and albedo variations on Titan's surface to dominate shortward of 2.12 μm. A comparison of spectra of various regions on Titan's disk on 26 September 1999 (Fig. 3.2) illustrates the diversity of spectra recorded across the disk. Equatorial spectra are brightest at 2.17–2.25 μm, while spectra of regions near Titan's south pole appear brighter at 2.12–2.16 μm. Near 2.10 μm, spectra cross one another again as local surface albedo begins to dominate.

Low-resolution images of Titan's surface, troposphere, and stratosphere can created by integrating each spectrum over a narrow wavelength range and displaying the resulting albedo over projections of the spectral apertures (Fig 3.3). Titan's surface is most clearly seen at 2.02–2.05 μm, but this spectral region was only sampled in 1999. The 2.10–2.12 μm range was observed on every run, and remains weakly sensitive to Titan's surface while also displaying a concentration of scattering particles near Titan's south pole. Summed

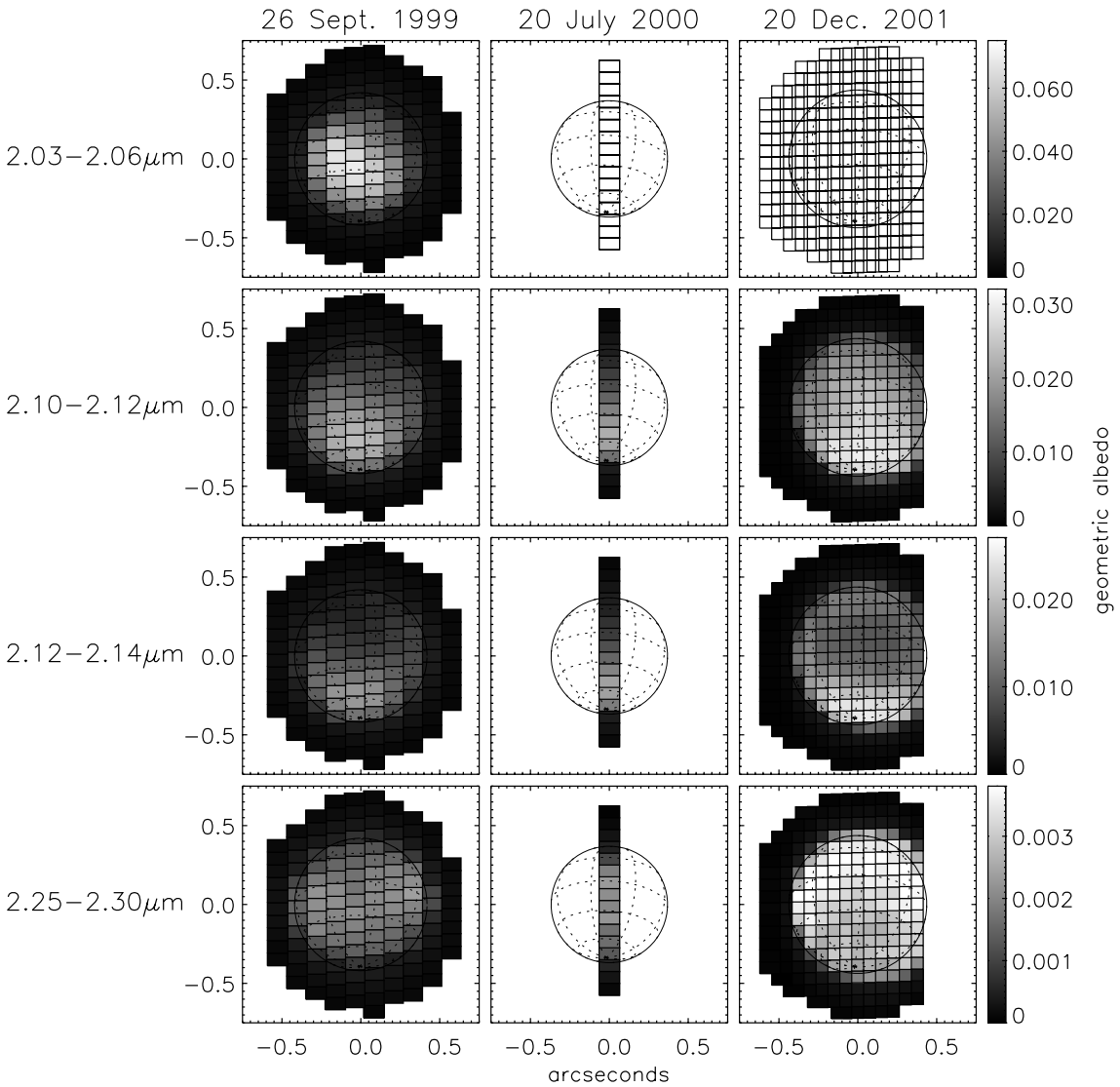

Figure 3.3: Narrow-band images of Titan created by averaging the spectrum recorded in each aperture over four narrow wavelength ranges. High contrast features on Titan's surface can be clearly seen at 2.02–2.05 μm on 26 September 1999. The surface contributes only weakly to the 2.10–2.12 μm images. A region of bright scattering particles near Titan's south pole is most clearly seen at 2.12–2.14 μm, where the atmosphere is opaque to Titan's surface. Obvious changes can be seen in the highest haze layers, seen most clearly in the 2.25–2.30 μm images. The apparent brightening of Titan at all wavelengths is due to the improved AO correction of the 2001 observations.

over 2.12–2.14 μm, all traces of Titan's surface disappear and he bright atmospheric feature near Titan's south pole is more clearly seen. Only a region of bright scattering near the tropopause, present above Titan's south pole but thin or absent over the equator and mid-latitudes, can account for this feature. The most dramatic change in the appearance of Titan's atmosphere between 1999 and 2001 can be seen in the 2.25–2.30 μm images, which record only the highest haze layers ($>$ 110 km altitude.)

3.4.2 Radiative transfer

The strategy we adopt to derive Titan's surface albedo and the opacity structure of the overlying atmosphere is to forward model the spectra, starting with a parametrized description of Titan's surface and atmosphere. Using the radiative transfer model of Griffith (1991), we compute the predicted reflectance spectrum at every location on dense grid covering Titan's disk, which we then spatially convolve by an estimate of the PSF and sample at the locations of the spectral apertures.

The equation of radiative transfer is approximated using the doubling and adding technique (Hansen and Travis, 1974). Titan's atmosphere is modeled as 147 layers ranging in thickness from 0.5 km near Titan's surface to 50 km at 1200 km altitude, using the temperature-pressure model of Lellouch (1990). Absorption due to CH_4 and H_2 is calculated line by line, and converted to correlated K-coefficients for the actual calculations. The CH_4 mixing ratio in the lower troposphere is assumed to be 0.07 (60% relative humidity at the surface), up to the height at which this equals the saturation value. The saturation mixing ratio is then followed to the tropopause at 40 km, above which the saturated tropopause value of 0.017 is followed (Lellouch *et al.*, 1989). Raleigh scattering by the gas is included, as is Mie scattering by haze (0.6 μm particles with tholin optical constants). CH_4 cloud particles are assumed to scatter isotropically, with a single-scattering albedo of 0.98.

3.4.3 PSF estimation

An estimate of the mean long-exposure PSF was determined for each set of observations by modeling the broad-band images acquired immediately prior to the spectrum observations. The nightly mean K$'$ or K_s image (Fig 3.1) was modeled by convolving a blank disk at the known location of Titan by a PSF consisting of a sum of 3 Gaussian functions. A sum of

Gaussians is clearly only a rough approximation to the true PSF, but its purpose here was primarily to estimate the power and width of the halo component, which is expected to be both smooth and symmetric. The structure of the PSF core and possible diffraction rings were of much less concern. The full-width at half maximum (FWHM) of the narrowest Gaussian was fixed at $0\farcs087$, that expected for a diffraction-limited PSF at 2.1 μm wavelength. The widths of the other two, and their relative contribution to the normalized PSF, were allowed to vary, and were optimized using the AMOEBA algorithm (Press *et al.*, 1992) to minimize the square of the difference between the predicted and observed halos (the region beyond the solid limb of Titan). The optimized PSFs were found to closely reproduce the observed halos, thus providing a robust estimate of the contribution of distant regions of Titan to individual spectral apertures.

3.4.4 Model optimization

Both Voyager and Earth-based observations have found Titan's haze to be zonally symmetric. This is to be expected from the long response time of the stratosphere to seasonal forcing, and the slow rotation of the satellite. Spatially resolving Titan's disk therefore allows us to sample a given haze column at a variety of emission angles. This reinforces the ability to constrain the vertical haze opacity profile, and to distinguish low haze from bright surface regions. The recent identification of discrete condensate clouds near Titan's south pole (Brown *et al.*, 2002; Roe *et al.*, 2002) indicates that tropospheric clouds cannot be treated in the same way.

The spectral modeling was performed in several steps, gradually increasing the number of free parameters; we describe here the most complex, final model. Titan's atmosphere is divided into 5 zonal bands whose widths roughly match the spatial resolution achieved under the worst conditions. The haze in each band is parametrized in terms of the optical thickness in 4 layers between 40 km and 1265 km altitude, plus a fifth layer in the troposphere whose altitude is allowed to vary. Each latitude band is further divided into longitudinal zones of width $\sim 45°$, between which only the surface albedo is allowed to vary. 14 independent surface albedo patches cover Titan's visible disk (Fig. 3.8). A maximum of 6 free parameters are therefore used to describe Titan's surface and atmosphere at each location on the disk, for a maximum total of 39 free parameters.

The observed spectra constitute a set of N measurements of the geometric albedo $y_i =$

$y_1, \ldots, y_N$ at location $\mathbf{r}$ and wavelength λ, with an associated uncertainty σ_i. We fit these spectra using the above model with M adjustable parameters $a_k = a_1, \ldots, a_M$. For a given vector of parameters $\mathbf{a} = (a_1, \ldots, a_M)$, we transform this model into a prediction of the spectrum in each aperture $y(\mathbf{r}, \lambda; \mathbf{a})$ as follows. We first use the radiative transfer model to calculate the predicted spectrum every $0\farcs010$ on a $1'' \times 1''$ grid centered on Titan. The emission angle for which the spectra are calculated varies between grid points, even within latitude bands and surface-albedo patches. The resulting three-dimensional dataset (a spectrum at every grid point) is then spatially convolved by the estimated PSF, and sampled at the locations of the actual spectral apertures. Assuming normally distributed errors σ_i, the maximum likelyhood estimate of the model parameters $\mathbf{a}$ will be achieved by minimizing the χ^2 merit function

$$\chi^2(\mathbf{a}) = \frac{1}{N-M} \sum_{i=1}^{N} \left(\frac{y_i - y(\mathbf{r}_i, \lambda; \mathbf{a})}{\sigma_i} \right)^2 . \tag{3.1}$$

We used the Levenberg-Marquardt algorithm (Press *et al.*, 1992) to optimize the M adjustable model parameters described above to minimize this merit function.

3.5 Results

3.5.1 Mean atmosphere

Though it is clear that Titan's haze, clouds, and surface albedo vary across the visible disk, disk average haze properties provides a useful point of reference, permitting comparison

Table 3.2: Radiative transfer model parameters

Model	Date	N^a	M^b	Wavelength (μm)	χ^2
Mean atmosphere	26 Sep 1999	89×105	5	2.12–2.30	18.4
	20 Jul 2000	26×105	5	2.12–2.30	11.5
	20 Dec 2001	150×105	5	2.12–2.30	9.0
Zonal atmosphere	26 Sep 1999	89×105	25	2.12–2.30	13.8
	20 Jul 2000	26×105	25	2.12–2.30	6.0
	20 Dec 2001	150×105	25	2.12–2.30	6.0
Atm. & surface	26 Sep 1999	89×120	39	2.03–2.05, 2.12–2.30	13.3

a. Number of spectral apertures, times the number of wavelengths fit.
b. Number of free parameters in the model.

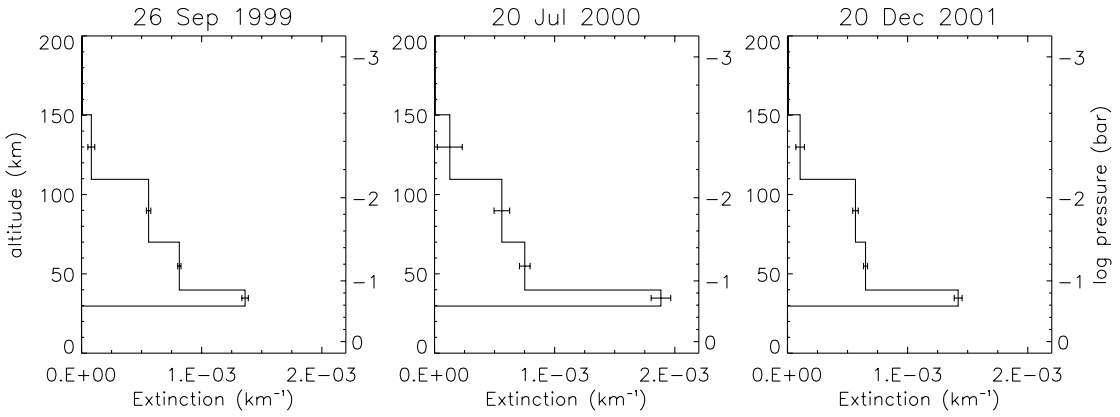

Figure 3.4: Average haze extinction profiles on each night. No haze or cloud layer is necessary below 30 km. Error bars represent 1-σ random error. To within the errors, the mean opacity distribution of the main haze layer ($>$ 40 km) appears to have remained unchanged over the two years spanned by these observations.

with previous disk integrated spectroscopy. We therefore first fit the observed spectra using a single set of parameters to describe the vertical haze profile at all latitudes, while performing all other aspects of the model optimization as described in section 3.4. Note that this average model is therefore weighted not by flux, as an unresolved spectrum would be, but by area (since the individual spectra are evenly distributed in area.) Only the spectral region insensitive to Titan's surface (2.12–2.30 μm) is used in the fit.

The resulting fit between the predicted spectra and those observed is not particularly good (see Table 3.2.) However, several interesting features of Titan's haze are apparent (Fig. 3.4). In a global mean sense, the total optical depth of scatterers in Titan's lower stratosphere remained constant over the two years of observations. The total haze optical depth was $\tau = 0.072 \pm 0.005$ on 26 September 1999, $\tau = 0.076 \pm 0.016$ on 20 July 2000, and $\tau = 0.070 \pm 0.006$ on 20 December 2000. The 1-σ uncertainties listed here and displayed in the figures are the random error due primarily to electronic and photon noise in the raw spectra. Not included is an additional systematic uncertainties, the most important being the uncertain flux calibration of the spectra which we estimate to be in error by less than 15% on 26 September 1999 and 20 December 2001, and 5% on 20 July 2000.

The haze extinction appears to increase with decreasing altitude to 30 km above Titan's surface, below which no haze is necessary to adequately model the spectrum. However, haze or clouds between 30 and 40 km altitude are required to correctly fit the spectra (Fig. 3.7).

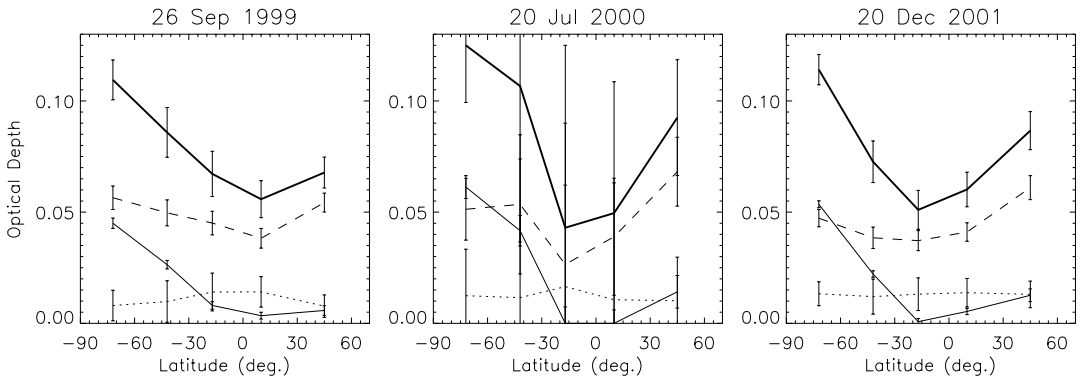

Figure 3.5: Summary of the optical depth of haze measured as a function of altitude and latitude. *Dotted line:* $>$ 110 km. *Dashed line:* 40–110 km. *Thin solid line:* 30–40 km. *Thick solid line:* Total scattering optical depth. Error bars represent 1-σ random error. Though the south polar tropopause scattering layer has remained unchanged over two years, a gradual shift to the north can be seen in the main haze layer above 40 km.

3.5.2 Zonal haze model

Gradually increasing the complexity of the model, we next divide Titan's atmosphere into five zonal bands. We continue to ignore the surface by fitting only the 2.12–2.30 μm region of the spectra. Figure 3.5 summarizes the evolution of the vertical distribution of the haze over the two years of observations, while vertical profiles near Titan's south pole and equator on 26 September 1999 and 20 December 2001 are shown in Fig. 3.6.

The most striking feature of the latitude-resolved haze profiles is the strongly scattering layer at 30–40 km altitude, present only at high southern latitudes. Though the layer is optically thin ($\tau \approx 0.05$), it accounts for half of the total scattering optical thickness at Titan's south pole. Above this tropospheric scattering layer, the main haze deck exhibits a distinctly different latitude dependence. At 40–110 km, aerosols appear evenly distributed in latitude in 1999, while a clear shift towards Titan's northern limb has occurred by December 2001. The highest haze layers to which these observations are sensitive, above 110 km, appear thicker above Titan's equator in 1999, but more evenly distributed by 2001. Haze profiles fit to the central meridian spectra taken 20 July 2000 are included in Fig. 3.5 to demonstrate that they are consistent with a gradual transition between the 1999 and 2001 aerosol distributions. However, the absence of a variety of emission angles sampling each zonal band of the model leads to far larger uncertainties in the retrieved haze optical depths.

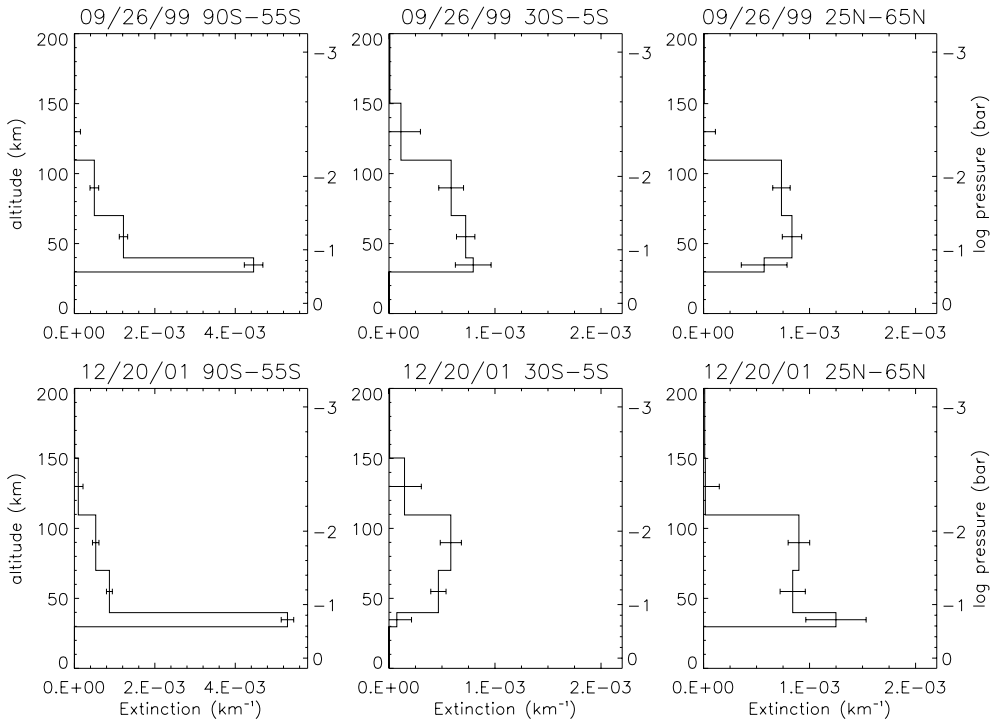

Figure 3.6: Sample haze profiles at 3 latitudes on Titan, on 26 September 1999 and 20 December 2001. The conspicuous scattering layer at 30–40 km altitude is reduced in thickness by at least a factor of 4 north of 30°S. Error bars represent 1-σ random error. Note the change in extinction scale between the plots.

In both the mean atmosphere and zonal models, the altitude of any tropospheric scattering layer is left as a free parameter, which is optimized along with its optical depth and the vertical distribution of the overlying stratospheric haze. Though the spectral fits indicate that the optimum altitude of a tropospheric scattering layer is 30–40 km, this result is not independent of the derived stratospheric haze profiles.

To better constrain the altitude of the southern tropospheric scattering layer, we isolate its spectrum by subtracting spectra of Titan's southern and northern limbs (Fig. 3.7). The residual shows a rapid rise in albedo between 2.17 and 2.14 μm. The residual is most closely fit by a layer of scattering particles at 30–40 km above Titan's surface, with an optical depth of $\tau = 0.04 \pm 0.01$. This is slightly lower than was found in the zonal model optimization, since some opacity ($\tau \approx 0.01$) is present at this altitude in the northern limb spectra as well. The difference spectrum can equally well be fit by a region of scattered optically thick clouds with tops near 40 km, covering $2.7 \pm 0.7\%$ of the region sampled by the southern spectra. By fitting the difference between southern and northern limb spectra, the altitude

at which we locate the layer is independent of our interpretation of the overlying haze. The disadvantage of this method is that the optical depth of the layer is underestimated. The primary uncertainty in the altitude is due to the poorly constrained distribution of CH_4 in Titan's stratosphere, which we assume to have a constant mixing ratio of 0.02 (Lellouch *et al.*, 1989). Below the tropopause scattering layer, Titan's atmosphere appears free any widespread haze or cloud layers with optical thickness $\tau > 0.01$ at 2.0 μm (averaged over the $\sim$ 1200 km projected spatial resolution), determined by inserting such a layer in the atmospheric model and testing for consistency with the observed spectra.

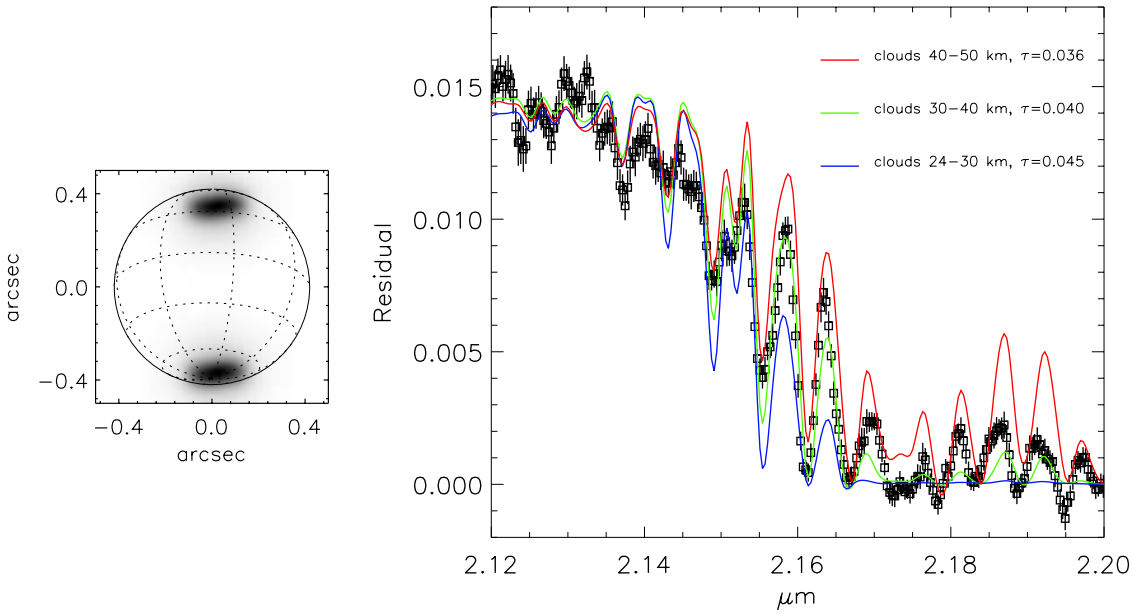

Figure 3.7: The difference between the mean of two southern and two northern limb spectra, fit with radiative transfer models. Their spatial weighting functions are displayed on the left. Model spectra were calculated with the identical geometry, and their difference fit to the residual. The extra flux in Titan's south polar atmosphere can best be fit by the addition of an optical depth $\tau = 0.04 \pm 0.01$ scattering layer at 30–40 km altitude in the south. Equivalently, the layer could consist of scattered optically thick clouds with tops at 30–40 km altitude, covering 2.7 ± 0.7 % of the south polar region.

3.5.3 Surface albedo

The opacity of Titan's atmosphere due to CH_4 and H_2 is sufficiently low at $\lambda < 2.12$ μm for images and spectra of Titan to record light scattered at the surface. Uncertainty in

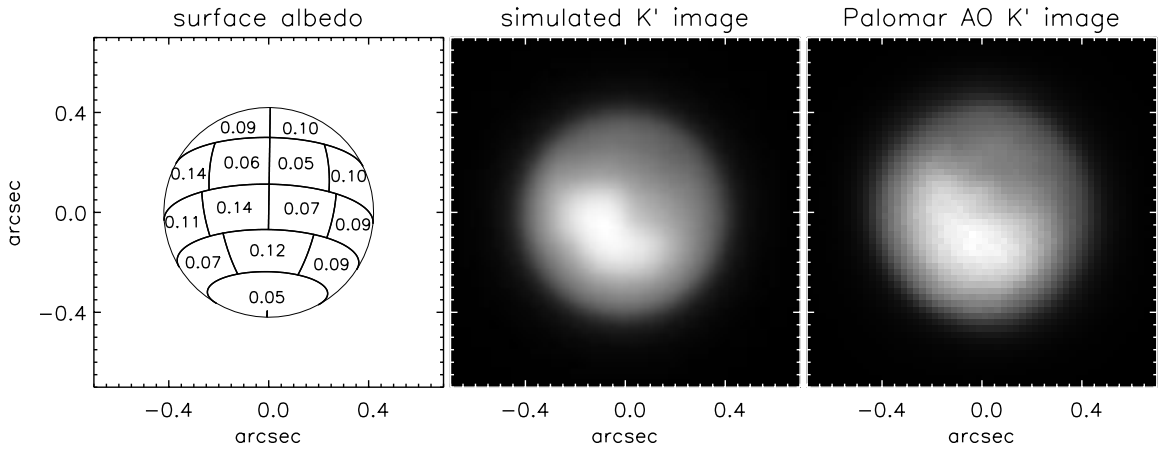

Figure 3.8: *left:* Titan's surface albedo at 2.04 μm, determined by optimizing a radiative transfer model to 89 spectra taken on 26 Septmber 1999. The locations of the 14 independent surface regions is arbitrarily. The atmosphere is divided into 5 zonal bands, in which the vertical haze distribution in 5 layers was simultaneously fit. The estimated uncertainty is 15%, dominated by the poor photometric calibration of the spectra. *center:* Model spectra at each location on Titan's disk were multiplied by the K$'$ transmission spectrum and spatially convolved by the estimated PSF, to produce this simulated K$'$ image. *right:* Actual Palomar AO K$'$ image of Titan taken at 07:24 UT on 26 September 1999.

the collision-induced absorption coefficients of H_2–N_2 leads to poor fits between the model spectra and those of Titan between 2.05–2.12 (Griffith *et al.*, 1998). Only our 26 September 1999 spectral observations recorded the region $\lambda < 2.05$ μm over which we can reliably determine Titan's surface albedo.

The surface albedo distribution determined by optimizing the full surface and atmospheric model described in Section 3.4.4 is presented in Fig. 3.8. Atmospheric parameters remain essentially unchanged from the atmosphere-only model fit, and no scattering layer between 5 and 30 km altitude is necessary to fit the spectra. The spectra provide no distinction between a bright surface and bright clouds below 5 km altitude.

Despite the coarse resolution and arbitrary locations of the patches into which Titan's surface has been divided, the derived albedo distribution does an excellent job of reproducing the spectra observed on 26 September 1999. Several sample fits are presented in Fig. 3.9. A further encouraging result is the quantitative similarity between a simulated K$'$ image of Titan computed from the surface albedo and haze distributions, and an actual image take the same night (Fig. 3.8).

Titan's surface displays strong albedo contrasts of at least a factor of two at regional

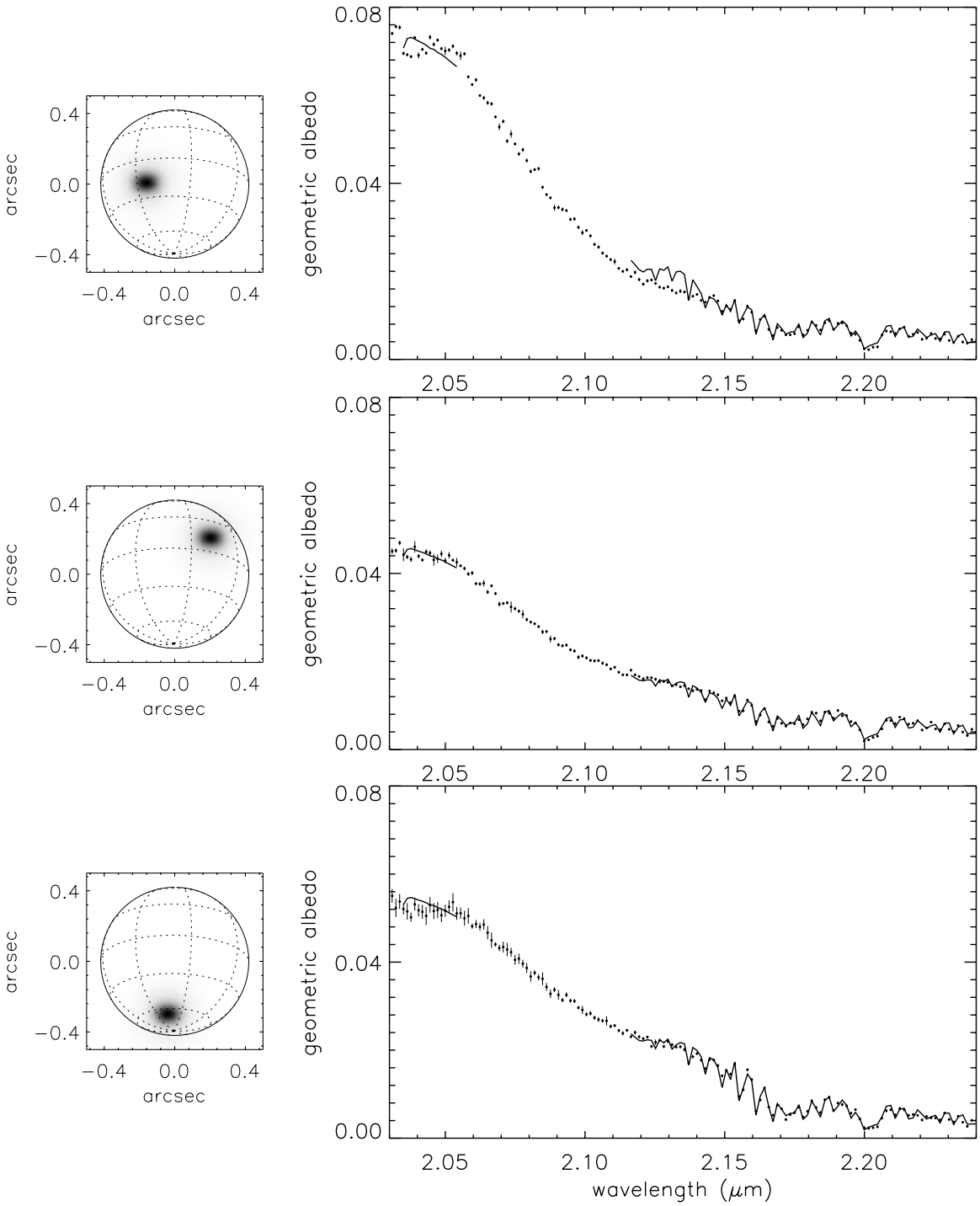

Figure 3.9: Sample model fits to three spectra taken 26 September 1999. The observed spectra are displayed as points, with 1-σ error bars which do not include the 15% photometric calibration uncertainty. The spatial weighting function of each spectrum is shown on the left. Optimized model spectra are indicated by solid lines. These three spectra were chosen to illustrate bright and dark surfaces (*top* and *center*) and the hazy south polar region (*bottom*).

spatial scales, despite the inevitable reduction in contrast imposed by a extended PSF. Though we attempt to correct for the PSF in our analysis by comparing a convolved synthetic images to the observations, the coarse resolution with which we parametrize the surface similarly reduces the recovered contrast. It is therefore quite startling that we find a range of albedos of nearly a factor of 3, from 0.05 ± 0.01 to 0.14 ± 0.02.

3.6 Discussion

3.6.1 Seasonal change in Titan's haze

The gradual northward movement of haze in the main layer above 40 km altitude appears to be an expression of the advection of haze in Titan's stratosphere by meridional winds. General circulation models indicate that pole-to-pole thermally direct winds probably dominate Titan's stratospheric meridional circulation during most of the year (Hourdin *et al.*, 1995; Rannou *et al.*, 2002). Titan's seasonally varying north-south brightness asymmetry at visible wavelengths is one consequence of haze advection by meridional winds.

Since 1994, Titan's northern hemisphere has been darkening in the blue, evolving back towards the state observed by Voyager in 1980 and indicative of a thickening high haze layer (Lorenz *et al.*, 1999). By 1997, the optical thickness of high haze (> 160 km altitude, appearing dark in blue filters and bright in CH_4 bands) in the north exceeded that in the south, while the layers below appeared to lag behind (Lorenz *et al.*, 2001). More recent visible adaptive optics observations of Titan confirm this picture, finding the main haze layer (< 90 km) globally uniform as late as November 2001 (Ch. 2).

The spectral observations presented here are more sensitive to changes in the total optical thickness of the main haze layer than visible-light images, and they record subtle changes between September 1999 and December 2001. While the optical depth of haze above Titan's tropopause appears to have remained constant in the south polar and equatorial regions, it has increased by $20 \pm 5\%$ at 45°N. Rannou *et al.* (2002) suggest an elegant mechanism for the thickening of the main haze layer in the mid-latitudes of the winter hemisphere. The pole-to-pole meridional winds act as a conveyor belt for aerosols created high in the equatorial stratosphere, carrying them first north (during southern summer) along the detached haze layer, then down towards the winter pole. The thickening haze would then circulate southward at lower altitude, causing the observed increase in main

layer's optical depth in the northern mid-latitudes.

3.6.2 Tropopause cirrus

The brightly scattering region near Titan's south pole has been noted previously in both visible (Lorenz *et al.*, 1999; Young *et al.*, 2002; Ch. 2) and near-infrared (Coustenis *et al.*, 2001; Roe *et al.*, 2002) images of Titan, but its altitude was misinterpreted or constrained only to lie within the troposphere. We have demonstrated that the spectral signature of this scattering layer reveals it to be at the very top of the troposphere, at 35 ± 10 km. Significantly, this is well above the transient tropospheric clouds which populate the same region. The tops of the transient clouds, interpreted to be convective towers initiated by surface heating, were found to lie at 16 ± 5 km (Brown *et al.*, 2002), near the level expected for moist convection (Griffith *et al.*, 2000).

A surprising feature of the tropopause scattering layer is its apparent stability, despite the seasonal changes taking place in the main haze layer above. It changed in neither thickness nor extent between 1999 and 2001, remaining restricted south of $\sim 30°$S. This same behavior was noted in the analysis of visible AO images of Titan in Ch. 2. The stability suggests that the aerosols which comprise the layer are either long-lived, or continuously replenished by a process which is not undergoing significant seasonal evolution.

Early suggestions that the layer might represent CH_4 or C_2H_6 condensation onto C_4N_2 ice-covered haze particles (Samuelson *et al.*, 1997) now seem unlikely, since the C_4N_2 source is expected to diminish rapidly as stratospheric temperatures rise in late spring. It also seems unlikely that the settling of haze from the main layer could lead to such a stable feature, during a season in which significant upward vertical motion is predicted (Hourdin *et al.*, 1995; Tokano *et al.*, 1999). The presence of tall convective clouds beneath the scattering layer, and a steady pole-to-pole circulation pattern, suggest another possibility. The tropopause scattering layer may be a region of cirrus-like CH_4 condensation clouds, related either to the upwelling of moist air in the convective plumes, or the regional upwelling of the summer pole. The later case would be analogous to optically thin tropical cirrus on the Earth, which form at the tropopause in the rising cell of the Hadley circulation (Kärcher, 2002). Higher spatial resolution observations will be required to distinguish between these various possibilities.

3.6.3 Surface

Resolved images of Titan through low-opacity spectral windows from 0.6 to 2 μm reveal high contrast, apparently permanent albedo features on its surface. However, the difficulty of analyzing broad-band (frequently deconvolved) images taken through an absorbing and scattering atmosphere has led to a lack of consensus on both the absolute albedos of features, and the contrast exhibited between bright and dark regions.

Early HST images of Titan's surface (Smith *et al.*, 1996; Meier *et al.*, 2000) were corrected for light scattered in Titan's stratosphere by subtracting a zonally averaged image, leaving no hope of recovering the absolute surface albedo. Most ground-based observers have instead relied on subtracting an image of Titan taken at a nearby wavelength sensitive only to the haze, but have stopped short of correctly modeling the absorption experienced by the residual light scattered from the surface (Combes *et al.*, 1997; Coustenis *et al.*, 2001; Ch. 2). Gibbard *et al.* (1999) estimate the absolute albedo of Titan's surface using a simple 3-layer radiative transfer model to interpret speckle interferometric images on two night. Though an improvement over the previously described techniques, one weakness of theirs is in the optimization of the haze model, for which they effectively assume Titan's surface to have zero albedo near the edges of the disk. Consequenly, the haze optical depth is overestimated to some degree, leading to an underestimate of the surface albedo and a possible overestimate of the surface contrast. Nevertheless, they find that the albedo of Titan's surface at 2.0 μm ranges from 0.05 to 0.13 at a spatial resolution of $\sim$ 240 km.

The spectral modeling technique which we have developed in this chapter allows both the surface albedo and three-dimensional haze distribution overlying the surface to be determined simultaneously, at the expense of a loss of spatial resolution (due primarily to the reduced spatial resolution generally achieved with the longer exposures required for spectroscopy.) We find that the 2.0 μm surface albedo of the hemisphere centered on coordinates 57°W, 21°S ranges from 0.05 ± 0.01 to 0.14 ± 0.02 when averaged over spatial scales of $\sim$ 1200 km. The mean surface albedo of this hemisphere of Titan (weighted by projected area) is 0.09 ± 0.01.

The hemisphere of Titan viewed on 26 September 1999 includes the eastern extension of the bright, continent-like feature centered at approximately 100°W and the very dark region to its north-east. Though there is little actual overlap with the surface albedo maps

of Gibbard *et al.* (1999), we derive a consistent albedo for the bright region (of which they viewed the western half), and similar values for the darkest areas surrounding it. We therefore concur with their surprising result that the 2.0 μm albedo of the large bright region is similar to that of the icy Galilean satellites, whose geometric albedos range from 0.10 (Europa) to 0.18 (Ganymede). The albedo of pure H_2O ice at 2.0 μm varies widely as a function of grain size, but spans the range 0.10–0.25 at the conditions found on the icy Galilean satellites (Clark and Mc Cord, 1980). If the bright region on Titan represents exposed water ice with a similar grain structure, then its relatively high albedo argues that extensive regions must be kept free of the accumulation of dark atmospheric sediments, by either topography or active meteorological processes. In contrast, dark areas surrounding the bright surface feature have a 2.0 μm albedo which is consistent with a surface covered by either hydrocarbons or expected atmospheric precipitates (Khare *et al.*, 1984, 1990).

3.7 Conclusions

The observations presented in this chapter comprise the first spatially resolved spectra of Titan at near-infrared wavelengths. They combine spatial and spectral resolution sufficient to simultaneously determine the vertical distribution of aerosols in Titan's atmosphere and the albedo of the underlying surface.

Over the period of September 1999 to December 2001 (late southern spring on Titan), the changing distribution of aerosols in Titan's stratosphere appears consistent with recent models in which haze is advected by thermally-direct meridional winds (Rannou *et al.*, 2002). However, a distinct scattering layer near the tropopause at high southern latitudes is not accounted for by current models, and may represent an optically thin CH_4 cloud layer condensing in a region of gentle uplift. Below this thin cloud layer, Titan's troposphere appears clear, as these observations did not achieve the spatial resolution necessary to detect the transient CH_4 clouds recently identified near Titan's south pole (Brown *et al.*, 2002; Roe *et al.*, 2002).

Below this complex and variable atmosphere, Titan's surface exhibits a striking range of surface albedo at 2.0 μm, varying between 0.05 and 0.14 at a projected spatial resolution of $\sim$ 1200 km. Only one other body in the solar system exhibits similarly strong surface albedo contrast on such large spatial scales; the Earth.

Chapter 4

Titan's stratospheric winds

4.1 Introduction

This chapter presents observations and analysis of a binary stellar occultation by Titan, imaged with high spatial resolution using the Palomar adaptive optics (AO) system on 20 December 2001. These observations are the first of their kind, simultaneously recording both the flux and angular deflection of starlight passing through the atmosphere of a small planetary body. While typical occultation lightcurve analyses are restricted to measuring atmospheric parameters local to the apparent location of ingress and egress of the star, this unique event probed Titan's stratosphere at two altitudes over most of the satellite. The combination of adaptive optics and the fortuitous alignment of Titan and a binary star has provided a dataset which is as rich scientifically as it is visually spectacular (Fig. 4.1).

This chapter has two goals. The first is to present a detailed description of the event and the data collection and processing steps used, so as to provide a useful dataset for future investigations. Both the raw and processed data are made available in the appendices. Second, I present an initial analysis of these unique observations, developing a new technique for tracing rays through a complex atmosphere, in order to determine the zonal wind field in Titan's stratosphere. I demonstrate that Titan's zonal winds are far from symmetric about the equator, and in some ways resemble those of the Earth and Mars, with a strong jet at high winter latitudes.

4.1.1 Stellar occultations

Occultations provide one of the principal tools with which we can remotely probe the upper atmospheres of solar system planets and satellites. Starlight (or a spacecraft's radio signal)

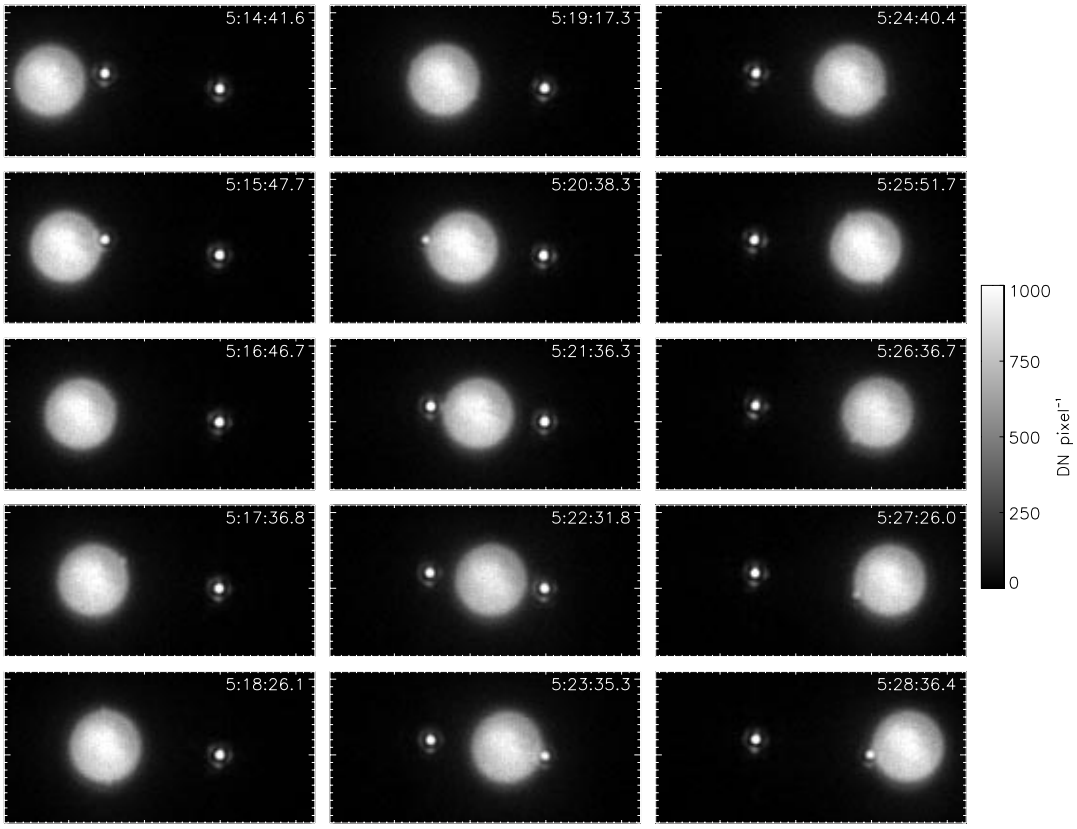

Figure 4.1: Titan occulting a binary star on 20 December 2001. This selection of bias- and gain-corrected 437-ms integrations was chosen to illustrate several observed phenomena and be approximately evenly spaced in time. They are displayed in a fixed stellar reference frame, with tick marks along the axes spaced every 0.″1. The both near and far-limb refracted stellar images can be recognized in many of the frames. The UTC midpoint time of each frame is marked.

traversing an atmosphere will be deflected in the plane of the local refractivity gradient, affecting its direction of propagation and its intensity. It may furthermore be scattered or absorbed by the gas or by aerosols suspended in the atmosphere. Rays initially tangent to the planet or satellite's limb may experience only a slight deflection, escaping the atmosphere to be detected by an observer beyond. The angular deflection and flux of the emergent starlight can reveal the density, composition, and aerosol content of the atmosphere (see review by Elliot and Olkin, 1996).

Most previous observations of stellar occultations have been restricted to measuring the refracted stellar flux as a function of time (the lightcurve), as an observer on Earth follows a chord across the planetary shadow. At any location within the shadow there exist at

least two points on the limb for which the observer lies within the plane containing by the star and the local refractivity gradient. Therefore, starlight refracted at both the near and far limb, defined with respect to the apparent position of the star behind the planet, will generally contribute to the observed flux. The primary cause of the dimming of starlight in the shadow is the increasing divergence of the beam of starlight as deeper regions of the atmosphere (where the refractivity gradient is higher) are traversed (Baum and Code, 1953). If the atmospheric composition is known and the opacity is negligible, the lightcurve observed along a chord through the shadow can be inverted to derive temperature and density profiles at the points of ingress and egress of the star on the planet's limb (French *et al.*, 1978).

Near the center of a planet or satellite's shadow, a central flash may be observed as the center of curvature of a portion of the limb is approached. A spherically symmetric atmosphere would focus light to the geometric center of the shadow, while the central flash of an oblate or otherwise non-spherical atmosphere has a more complex structure. The central flash was first recorded in unresolved photometry of the occultation of ϵ Gem by Mars on 8 April 1976. The flux recorded in the caustic was used to derive the mean opacity of the lower Martian atmosphere near the south pole, the region inferred to have been traversed by the magnified rays (Elliot *et al.*, 1977). Central flashes have since been recorded photometrically during stellar occultations by Titan (Hubbard *et al.*, 1993, hereafter H93), Neptune (French *et al.*, 1998), and Triton (Elliot *et al.*, 1998).

While much can be inferred from an occultation lightcurve alone, the complementary measurement of the angular deflection of the starlight has rarely been attempted. The only previous spatially resolved observations of an occultation were reported by Nicholson *et al.* (1995, hereafter N95), who acquired a sequence of near-infrared images of the occultation of 28 Sgr by Saturn on 3 July 1989. They observed a central flash, resolved into four separate refracted images of the star moving along Saturn's northern and southern limbs. The plane of the starlight's angular deflection (or the apparent position angle of the refracted stellar images on Saturn's limb) is sensitive to the projected shape of surfaces of constant number density, which will be function of planetary rotation and the zonal wind speed. N95 used the location of the central flash images to demonstrate that the mid-latitude tropospheric winds measured by cloud tracking decay with height to a global stratospheric flow whose speed is equal to the mean of the tropospheric values.

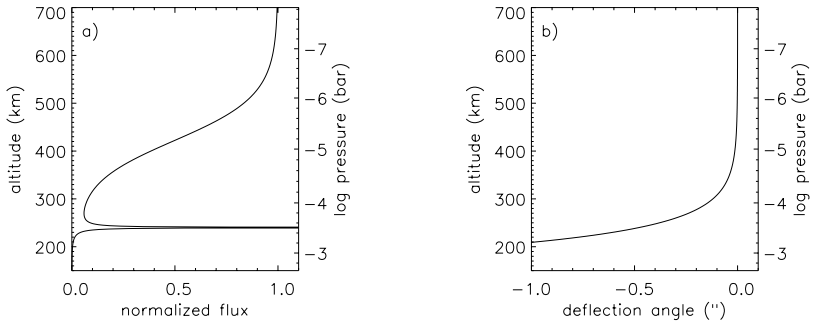

Figure 4.2: The predicted flux (a) and angular deflection (b) of starlight during and occultation by Titan, with respect to the minimum altitude or pressure reached. A pure N_2, spherically symmetric, isothermal stratosphere at $T = 165$ K was assumed, with the number density normalized to $n(r_0) = 3.1 \times 10^{22}$ cm^{-3} at $r_0 = 2775$ km (Yelle *et al.*, 1997). The central flash is produced when light penetrating to 240 km altitude is refracted by $0\farcs44$, concentrating it at the geometric center of Titan's shadow. See Section 4.4 for details.

4.1.2 Region of atmosphere probed

Stellar occultations observed from Earth probe the stratospheric regions of most planets. In the case of Titan, the first detectable drop in the flux of an occulted star due to differential refraction occurs when the tangential ray penetrates to an altitude of ~ 600 km ($\sim 10^{-7}$ bar, Fig. 4.2a). Starlight reaching deeper into the stratosphere is refracted at progressively greater angles, reaching $0\farcs44$, the apparent radius of Titan on 20 December 2001, near 240 km altitude (3×10^{-4} bar, Fig. 4.2b). The central flash is therefore produced by light penetrating to this region of the atmosphere, while far-limb images sample the atmosphere at only a slightly greater depth.

The occultation observations presented in this chapter are therefore sensitive to the broad region of Titan's stratosphere extending from roughly 200 to 600 km above Titan's surface. The flux and angular deflection are each most sensitive to different zones, with measurable changes to the flux occurring well before significant angular deflection of the starlight. The half-light level, roughly the point at which scintillation due to pressure inversions begins to degrade the usefulness of the flux as a measure of atmospheric scale height, occurs near 420 km altitude (7×10^{-6} bar). Coincidentally, this is also the level at which our observations become sensitive to the angular deflection. Haze opacity for a tangential ray of light becomes significant below 350 km, though it is likely to be seasonally variable and a strong function of latitude (Rages and Pollack, 1983; H93).

4.1.3 3 July 1989 Titan occultation

The only previous widely observed stellar occultation by Titan took place on 3 July 1989 when Titan passed in front of the bright star 28 Sgr, 15 hr after its occultation by Saturn (H93; Sicardy *et al.*, 1999). Lightcurves were recorded at 15 observing stations in Europe and Asia, and their analysis has provided a nearly global measure of the pressure and temperature structure between 350 and 500 km altitude (10^{-4} to 10^{-6} bar), a range of altitudes to which Voyager instruments were mostly insensitive. This region of Titan's stratosphere was found to be roughly isothermal over both altitude and latitude, with a temperature between 150 and 170 K, in agreement with radiative transfer models (Lellouch *et al.*, 1989; Yelle *et al.*, 1997). However, two distinct and apparently global pressure inversions were identified at 425 and 450 km altitude, corresponding to temperature fluctuations of 10 K over a vertical scale of $\sim$ 10 km.

H93 analyzed the central flash of the 28 Sgr occultation, recorded photometrically at 9 sites in northern Europe. The detailed appearance of the flash is a non-unique but sensitive function of the shape of surfaces of constant refractivity along Titan's limb, at the altitude at which light is deflected by the apparent radius of the satellite ($\sim$ 240 km). H93 found Titan's limb to exhibit a flattened equatorial bulge, 14 km higher at the equator than at 65°S, the highest latitude to which they were sensitive (Fig. 4.3a). The distribution of observing stations, and higher haze opacity in Titan's northern hemisphere, prevented similar measurement of the northern limb. In the absence of temperature gradients, such variations in pressure at a given altitude must be centrifugally supported by zonal winds, which thus appear strongest at high southern latitudes (Fig. 4.3b). Our observations were partly motivated by these elegant results, and the realization that AO-compensated imaging of an occultation would provide a means to test and extend this measurement of Titan's zonal wind structure.

4.1.4 20 December 2001 Titan occultation

Little was known about the stars which Titan occulted on 20 December 2001 prior to the event. In fact, the binary nature of the system was not recognized until the first AO-resolved images were taken at Palomar, one hour prior to the ingress of the eastern component. The star system (assumed single) is identified as NV0435215+200905 in the 2MASS catalogue,

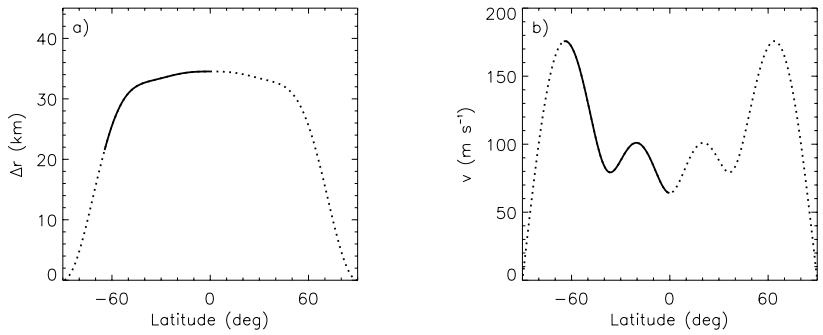

Figure 4.3: The shape of surface of constant refractivity (a) and inferred zonal wind field (b) in Titan's stratosphere, inferred from the central flash observed during the occultation of 28 Sgr (Hubbard *et al.*, 1993). The zonal wind field is that required to cyclostrophically balance the observed limb shape (balancing both the centrifugal acceleration and pressure gradient). Observations were sensitive only between the equator and 65° S, marked with a solid line. The limb shape and wind field have been extrapolated beyond this region assuming symmetry across Titan's equator.

with magnitudes $J = 11.447 \pm 0.033$, $H = 10.739 \pm 0.034$, and $K = 10.612 \pm 0.031$, consistent with stellar types K9V or K4III (Young, 2001). The USNO-A2.0 visible magnitudes are $B = 14.5$ and $R = 12.4$.

Predictions of the occultation provided by Leslie Young placed Palomar Observatory 100 ± 100 km from the centerline of Titan's shadow. In retrospect, this appears to have been an accurate prediction of the shadow cast by the photocenter of the binary. The actual centerline tracks, calculated from the positions of the the binary components determined from our observations using equations given in Smart (1931), are displayed in Fig. 4.4.

In addition to the results described in this chapter, the 20 December 2001 occultation was observed with adaptive optics on the 3.6-m AEOS and the 10-m Keck-II telescope. Though near the centerline of the first star's shadow, these observations were adversely affected by the high airmass at which Titan was viewed from Hawaii, and various technical difficulties. The Keck observations have, however, provided multi-wavelength photometry of the occulted stars from 1.2 μm to 2.3 μm (Roe, 2002b). The event was also observed using conventional near-infrared photometric techniques at the 2.3-m Wyoming Infrared Observatory, the 1.8-m at Lowell Observatory, and the NASA's 3-m Infrared Telescope Facility. The synthesis of the photometric observations is being coordinated by Leslie Young.

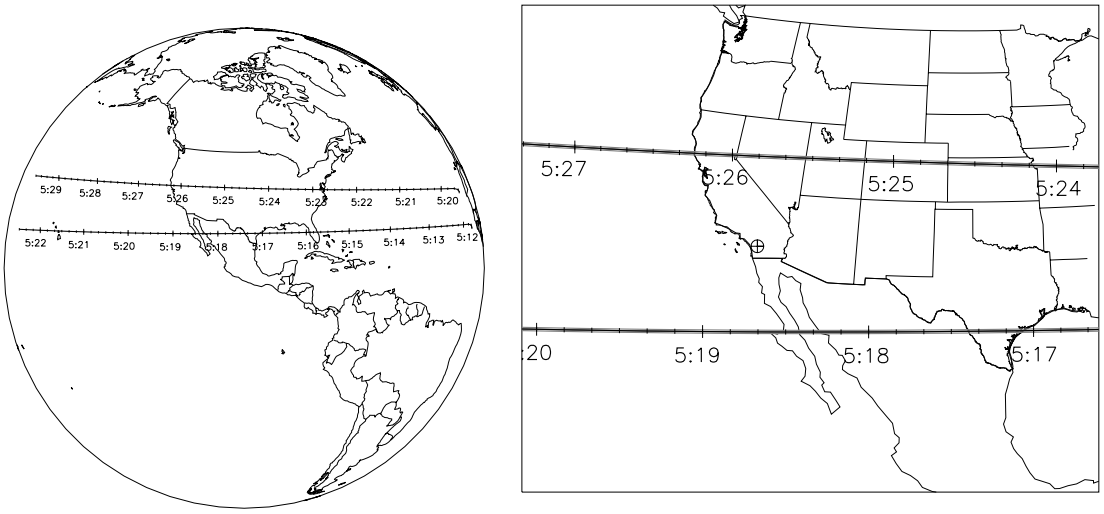

Figure 4.4: Tracks of the center of Titan's shadow on the surface of the Earth, displayed on an orthographic projection centered on the sub-Titan point at 5:22 UT. The tracks were computed from the stellar positions, relative to the known position of Titan, derived by fitting an atmospheric model with uniform super-rotation to the flux and angular deviation of near- and far-limb refracted stellar images of both occultations (see Section 4.4.8 for details.) The 1-σ uncertainty in the position of each track is indicated by the width of the underlying gray line. Ticks mark 10 s and 1 minute intervals. The location of Palomar Observatory is marked with a circled cross.

4.2 Observations

4.2.1 Adaptive optics

The observations were performed using the JPL adaptive optics system (Dekany, 1996) coupled to the Cornell-built PHARO near-infrared camera (Hayward *et al.*, 2001) at the Cassegrain focus of the 5-m Palomar Hale telescope. Titan ($V \approx 8.2$) acted as the reference source with which the phase aberrations induced by Earth-atmospheric turbulence were measured. The deformable mirror and tip-tilt mirror were both run at the maximum possible update frequency of 500 Hz. The relative faintness of the occulted stars in the visible rendered them effectively invisible to the Shack-Hartmann wavefront sensor. Prior to the first occultation, the AO correction quality was optimized for the color and angular size of Titan by adjusting the locations to which the Shack-Hartmann spots were driven.

All images were taken through a K' filter (1.945–2.296 μm) to maximize the AO correction quality and the photons collected from the very red stars. The Strehl ratio S, the ratio of the peak brightness measured on a point source to that of a diffraction-limited optical

system, fluctuated in the range $0.21 < S < 0.47$ due to changing Earth-atmospheric conditions, with a median during the occultations of $S_{\rm med} = 0.33$. Intermittent thin cirrus were present throughout the observations, but they did not significantly impact AO performance.

4.2.2 Timing

Operating without a shutter, integration times on PHARO's 1024×1024 pixel HgTeCd HAWAII detector are determined by the time elapsed between non-destructive readouts. Balancing the requirements of a sufficiently wide field-of-view, short integrations, and a reasonable duty cycle, we chose to read out only an $8'' \times 4''$ (320×160 pixels at 25 mas pix^{-1}) region near the center of the detector. Each integration cycle consisted of a "reset-read" in which each line the sub-array is reset to the bias voltage and the potential of each pixel then read to memory (340 ms), a 100 ms pause, a second readout (340 ms), and a final 100 ms pause during which the reset-read frame is subtracted from the final frame and the difference saved to disk. The effective integration time of each pixel is thus 440 ms, and the time elapsed between the start of successive integrations is 880 ms. The serial nature of the readout causes the images to be asynchronous, with the integration midpoint differing by up to 340 ms from the lower to the upper edge of the sub-array. However, the maximum delay between integration midpoints across Titan's disk is only 75 ms.

Precise timing of each frame in the occultation imaging sequence was assured by synchronizing the data-taking computer's system clock to Coordinated Universal Time (UTC) using Network Time Protocol software, accurate to approximately 0.1 s. The system time at the start of integration of each frame was written to the image header, rounded down to the nearest second. However, within each set of 256 frames the relative timing of the integrations is known to 1 ms. We therefore linearly interpolated the start times within each set (adding 0.5 s to each recorded time), leading to a final conservatively estimated timing accuracy of 0.2 s. All times quoted in this chapter refer to the integration midpoint of the central pixel of the sub-array.

Images were taken continuously from 4:48 UT to 5:58 UT, in sets of 256 with a gap of 3.68 s between sets, for a total of 4700 frames. Since Titan acted as the reference source tracked by the wavefront sensor, the satellite remained roughly fixed on the detector while the stars appeared to drift by from west to east. In each 3.68-s gap between exposure sets, we offset Titan by a fraction of an arcsecond eastward, to keep the field of view roughly

centered on the midpoint between Titan and the stars. To the amazement of all those present at the telescope, 4700 frames spanning both occultations were acquired without a single failure of either the telescope control system, AO system, or PHARO camera. Everything went perfectly.

4.3 Data reduction

The goal of the reduction steps performed on the 4700 images is to determine the relative position and flux of the stars (and stellar images refracted by Titan's atmosphere) with the highest possible accuracy. In effect, this requires fitting a model to each image composed of Titan and two (or more) point sources, convolved by a single PSF which varies from each frame to the next. For convenience and clarity, we perform this fit in four distinct steps. We first correct for detector bias and non-linearity in every frame. Next, we calculate a deconvolved model of Titan's disk using a convenient subset of the images. Third, we solve for the varying PSF and subtract a convolved model of Titan's disk from each frame. In a final step, we determine the relative locations and flux of any stellar images which remain.

4.3.1 Bias and gain correction

The images were processed using standard near-infrared image reduction techniques, including the subtraction of a median dark frame, division by a mean of twilight sky observations (a map of pixel gains), and correction for insensitive pixels. However, the operation of the PHARO camera at such an unusually phrenetic pace led to some electronic glitches which needed to be compensated for in the reduction process. The first 3–4 frames of each set of 256 exhibited a variable bias level, which appeared ramped along the slow-scan direction (north-south) of the detector. These frames were eliminated from the sets of dark exposures and twilight sky frames. The equivalent frames in the occultation imaging sequence were corrected by subtracting the median of pixels along the east and west margins of the frame from each row, then subtracting a similarly modified standard dark frame, before dividing by the pixel gain map. In a final step, the mean sky brightness measured far from Titan and the stars was subtracted from each frame. A series of representative reduced images is displayed in Fig. 4.1.

4.3.2 Titan disk model

A model of Titan's disk was first calculated by running the blind deconvolution program IDAC (Jefferies and Christou, 1993) on 400 independent sets of 4 consecutive frames, in which the stars were well separated from Titan's disk. Given N images of the same field acquired with a varying PSF, IDAC iteratively determines the single deconvolved image and N PSF maps which best fit the data in a least-squares sense, using prior information such as positivity and a band-limited PSF to break the degeneracy inherent in solving for $N + 1$ quantities. The relative motion between Titan and the stars over 4 frames is only 0.34 pix, allowing the field to be treated as unchanging in this context. The 400 independent deconvolved images of Titan were co-aligned by cross-correlation with a blank disk and averaged to create our disk model, shown in Fig. 4.5. We did not use the PSFs recovered by IDAC in further processing, as they were typically somewhat broader than those measured directly from the companion star.

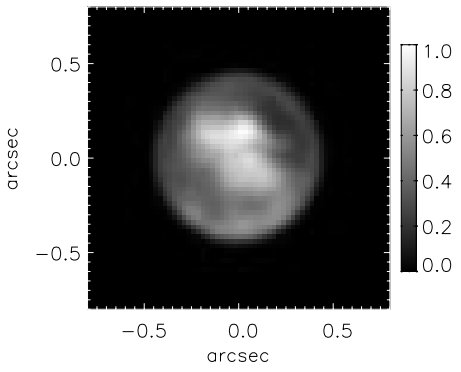

Figure 4.5: Deconvolved model of Titan's disk, created from 400 frames in which the stars were well separated from Titan. This model, convolved by the PSF of the most distant star, was then subtracted from each frame in the imaging sequence. Complex bright and darks surface markings dominate this view of Titan's leading hemisphere, but the unresolved bright features along the southern limb are most likely tropospheric clouds (compare to Roe *et al.* (2002), Fig. 4b.) The deconvolution process leads to some spurious brightening of the entire limb.

4.3.3 PSF determination

The extraction of the PSF of the star most distant from Titan in each frame also followed an iterative procedure, since the broad seeing-limited wings of Titan and the star were superimposed on one another. In each frame, a preliminary PSF was first extracted after the subtraction of Titan's mean radial profile. Each star was then precisely located and subtracted from the original image, using a non-linear least-squares minimization between the PSF model and the radially-subtracted image to solve for their relative offsets and

flux ratios. Next we convolved our IDAC-derived model of Titan's disk by the preliminary PSF, and performed an identical least-squares fit between this model image and the star-subtracted image, to determine the relative location and flux of Titan's disk. Finally, the convolved, shifted, and scaled model of Titan was subtracted from the original frame and the entire process repeated, until the extracted PSF showed no azimuthal asymmetries due to the incorporation of light from Titan. All image translations in this process were performed by adding a phase ramp to the imaginary part of the image's Fourier transform, then transforming back to the image domain. This technique preserves the spatial frequency content of the image, while allowing precise shifts of a fraction of a pixel.

The end result of this modeling and subtraction procedure was a set of 4700 Titan-subtracted frames, and an accurate PSF model for each. The sample Titan-subtracted frames are displayed in Fig. 4.6. Though no coherent residual remains at Titan's location, flat-fielding errors and photon noise are both elevated in the region of Titan's disk, leading to a factor of ~ 4 increase in the noise over the background level of 6.2 DN pix^{-1}.

4.3.4 Relative position and flux of stars

Finally, the accurate subtraction of Titan allows us to precisely determine the relative positions and flux ratios of the stars and refracted stellar images which remain. The star furthest from Titan acts as the astrometric and flux reference, against which the other stellar images are cross-correlated. In each frame, we minimized the square of the difference between the reference star and each other stellar image, solving for their relative offset in pixels (using the Fourier shift technique) and flux ratio (Fig. 4.7).

The uncertainty in these quantities was estimated by performing Monte Carlo simulations for each frame, reproducing the uneven background level, noise distribution, and flux for each stellar image, and repeating the fit on 100 synthetic frames. Far from Titan, the relative position of the stars is measured to better than 0.01 pix (0.25 mas), while the relative flux is determined to 1% . For fainter refracted stellar images on Titan's limb, the uncertainty in relative position sharply increases to ~ 0.15 pix in typical frames.

Even in the absence of Titan, the measured relative position of the two components of the binary would vary slowly as a function of location on the detector (due to optical distortion) and terrestrial airmass (due to differential refraction). Similarly, the measured relative flux might also evolve slowly due to optical distortions, airmass, and perhaps stellar

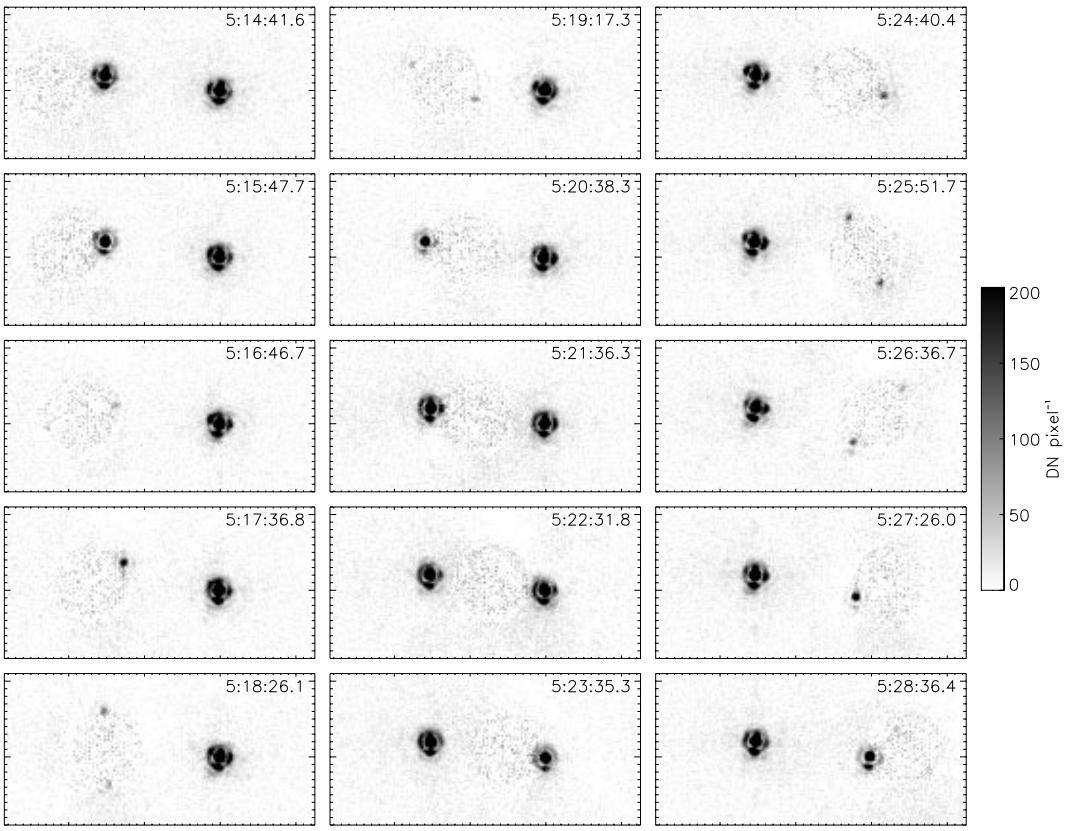

Figure 4.6: The same series of images displayed in Fig. 4.1, after subtraction of Titan's image. The stretched and inverted gray-scale highlights the absence of a coherent residual at Titan's location. Faint, variable refracted images of the occulted star are now visible in nearly all of the images.

variability. As noted in Section 4.4.8, the precision of these measurements is such that we do detect several of these effects, but they are at least two orders of magnitude smaller than the more rapid changes caused by the passage of Titan's atmosphere thought the line of sight.

The cross-correlation of stellar images was in fact performed twice. In a first iteration, we visually identified and measured only the obvious near-limb refracted stellar images, ignoring the far-limb images and any frames in which no refracted images were readily apparent. After optimizing an atmospheric model to these initial measurements (see Section 4.4.8 for details), we then predicted the positions of near- and far-limb refracted images in every frame, and fit the shifted and scaled reference PSF to every one of these locations. In some cases, noise spikes near the predicted locations were incorrectly identified as refracted

images, but the uncertainties determined by the Monte Carlo technique correctly quantify the irrelevance of such identifications. We furthermore carefully confirmed that no obvious refracted images were missed by the automated technique due to inaccuracies in the initial atmospheric model.

The end result of the data reduction is a list of the relative position and flux of every stellar image detected in each frame, with respect to the star furthest from mid-occultation. This table is reproduced in its entirety in Appendix A. We also display the relative positions and fluxes graphically in Fig. 4.7.

4.4 Model

4.4.1 General approach

The observable quantities which we use in this analysis are the relative position of the two stars in detector coordinates and the ratio of their flux, both as a function of time. The relative position, in particular, can be measured with extraordinary precision. The angular deflection and flux of starlight which interacts with Titan's atmosphere will be a function of the geometry of the occultation and atmospheric properties of Titan such as composition, scale height, zonal wind field, etc. In addition, since we are not in fact measuring the angular deflection or flux of the starlight directly but rather the relative separation and recorded flux of two stars on a detector, several other instrumental parameters must also be considered. We will ignore these instrumental effects for now, and present first a model for the propagation of starlight through Titan's atmosphere and to an observer on Earth. Instrumental effects are addressed in Section 4.4.7.

Our primary interest in this chapter is to determine the zonal winds in Titan's stratosphere, whose presence is reflected both in the position of refracted images on Titan's limb and, to a far lesser extent in the flux of these images. We also consider the effects of temperature and haze. Other observed phenomena, such as scintillation due to kilometer-scale pressure variations in Titan's stratosphere, are ignored and treated only as a source of noise. The model proves far too complex to allow a direct inversion of the measured stellar positions and fluxes to retrieve atmosphere parameters. Instead, we compute predicted observables, effectively creating a synthetic dataset based on a small set of parameters, and optimize the parameters to minimize deviations between the synthetic and actual observations.

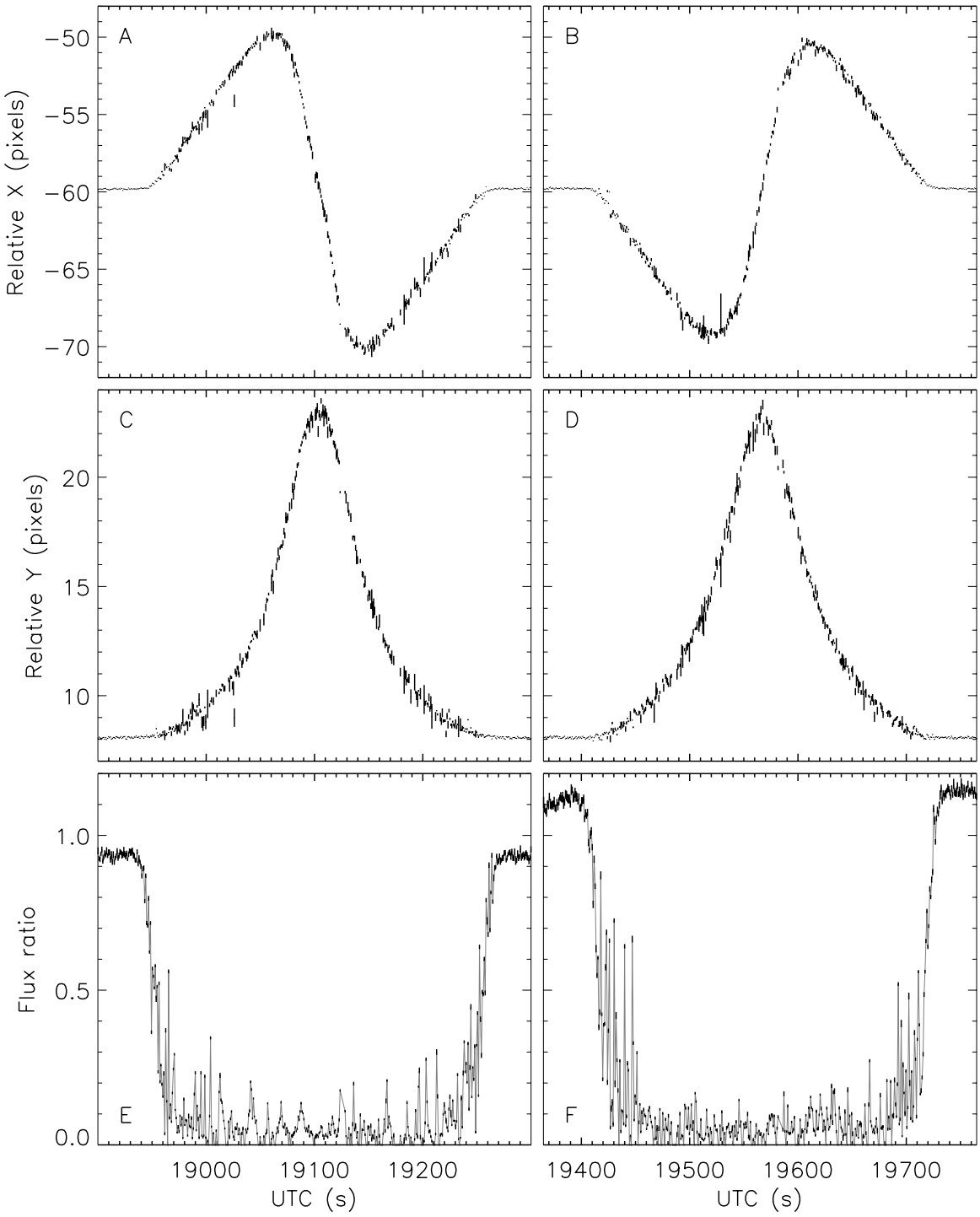

Figure 4.7: Relative position and flux of stars during successive occultations by Titan, in detector coordinates $x_{\rm det}$ and $y_{\rm det}$.

We use a numerical technique based on previous analytic models of stellar occultations by Pluto, Saturn, and Titan. nocite1992AJ....103..991E Elliot and Young (1992, hereafter EY92), derived equations for the expected angular deflection and flux of light refracted through a weakly bound atmosphere, one in which the scale height is a non-negligible fraction of the body's radius. They include the effects of gradients in atmospheric temperature, composition, and opacity and assume the planet and its atmosphere are spherically symmetric. This model successfully reproduces most of the phenomena which we observe (with the notable exception of the scintillation), but significant deviations from the predicted stellar positions occur near deepest occultation of both stars, which we will demonstrate are caused by strong winds in Titan's stratosphere.

The effect of a non-spherically symmetric atmosphere on the propagation of starlight was addressed by both H93 and N95 in their analyses of the central flash produced by the Titan and Saturn occultations of 28 Sgr. Both authors, however, used the simplifying approximation that the central flash is produced by refraction at a single surface of constant refractivity in the atmosphere. The models of H93 and N95 therefore predict only the direction of the refraction of starlight, equivalent to predicting only the position angle of refracted images along the limb. We initially attempted to combine the techniques of EY92, H93, and N95 to develop an analytic model for both the direction and magnitude of the angular deflection of starlight incident on an axially symmetric (but non-spherical) atmosphere. However, the tilt of Titan's polar axis (the presumed axis of symmetry of the atmosphere) with respect to the direction of the incoming starlight renders integrals of atmospheric parameters along the path of the ray prohibitively complex. It proved simpler and more intuitive to calculate such integrals numerically.

Though the geometry of the current problem is complex, we can make several simplifying assumptions regarding Titan's atmosphere which could not be made in the aforementioned studies. First, Titan's atmosphere can be considered isothermal over the region of interest (240–600 km above Titan's surface). As shown in Fig. 4.4.1, radiative transfer models of Titan's atmospheric temperature structure based on Voyager observations (Lellouch, 1990; Yelle *et al.*, 1997) predict at most a 30 K difference in temperature between 10^{-7} and 3×10^{-3} bar. These models are supported by retrievals of the temperature profile from lightcurves measured during the occultation of 28 Sgr (H93), though the scintillations seen in both those lightcurves and the present observations demonstrate that fine scale temper-

Table 4.1: Variables used in the occultation model

Coordinate systems	
R, ϕ, λ	Planetocentric radius, co-latitude, longitude
ρ, θ, z	Cylindrical coordinates in planet plane
ρ', θ'	Polar coordinates in observer plane
x', y'	Cartesian coordinates in observer plane
α, δ	Relative right ascension and declination
$x_{\rm det}, y_{\rm det}$	Relative detector coordinates
Atmospheric parameters	
T, P, N	Temperature, pressure, number density
ν	Refractivity
Other important variables	
Θ, Φ	Deflection angle, normalized flux of starlight

ature structure does exist (Sicardy *et al.*, 1999). We furthermore assume the atmospheric composition to be unchanging over this region, as reflected in the mean molecular weight. Titan's homopause lies well above the region of interest, near 1000 km (Müller-Wodarg and Yelle, 2002).

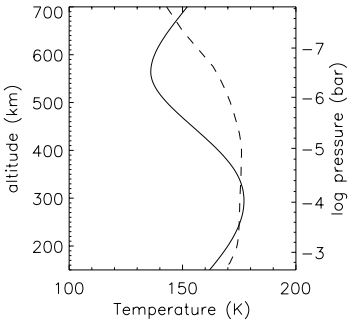

Figure 4.8: Radiative transfer models of the temperature structure in Titan's stratosphere by Yelle *et al.* (1997) (solid lines) and Lellouch (1990) (dashed line).

4.4.2 Coordinate systems

We first must define a set of coordinate systems in which the refraction and absorption of starlight by Titan's atmosphere can be described (Table. 4.1). We generally follow the notation of EY92 and N95, though changing variable as necessary to eliminate duplications.

The properties of Titan's atmosphere can best be described in spherical coordinates, in which R, ϕ, λ represent radius, planetocentric co-latitude (measured from the north pole), and east longitude, whose origin lies in the direction of the observer. The refraction of starlight is better described in a cylindrical coordinate system, represented by ρ, θ, and z, where z runs parallel to the axis of the shadow. ρ represents the radial distance from the

shadow axis, and θ is the angular coordinate, measured clockwise from the plane containing Titan's rotational axis and the star.

We can project Titan's shadow onto an observer plane, that containing the observer and perpendicular to the shadow axis at a distance $z = D$ from Titan's center. Locations in the observer plane are described by either their polar coordinates ρ' and θ' or Cartesian coordinates x' and y', centered on the shadow axis and with the y-axis coinciding with the origin of θ'. Finally, we also use the quaint yet traditional spherical coordinate system of right ascension α (increasing eastward) and declination δ to describe the relative locations of Titan and a star, and the variables $x_{\rm det}$ and $y_{\rm det}$ to describe relative positions on the detector.

Equations to convert from spherical to cylindrical coordinates are given by N95 (though note that they use planetocentric latitude, rather than co-latitude). The reverse transformation can be performed in the following three steps. We first define a rectangular set of coordinates X, Y, and Z centered on Titan, whose Z axis is aligned with that of the shadow and $X - Z$ plane contains Titan's rotational axis.

$$X = \rho \sin\theta, \tag{4.1}$$

$$Y = \rho \cos\theta. \tag{4.2}$$

We next define a second set rectangular coordinates U, V, W, rotated by an angle $\phi_{\rm se}$ around the $x = U$ axis to align the V axis with Titan's north pole. $\phi_{\rm se}$ is the co-latitude of the sub-Earth point on Titan at the time of the observations, equal to $115\overset{\circ}{.}53$.

$$U = X, \tag{4.3}$$

$$V = Y \sin\phi_{\rm se} + Z \cos\phi_{\rm se}, \tag{4.4}$$

$$W = -Y \cos\phi_{\rm se} + Z \sin\phi_{\rm se}. \tag{4.5}$$

We finally convert to planetocentric spherical coordinates by the following equations.

$$r = \sqrt{U^2 + V^2 + W^2}, \tag{4.6}$$

$$\phi = \cos^{-1}(V/r), \tag{4.7}$$

$$\lambda = \tan^{-1}(U/W). \tag{4.8}$$

4.4.3 Deflection angle and flux

With the coordinate systems defined, we write the basic equations for the bending angle Θ and the normalized flux Φ of a refracted beam of starlight. A ray of starlight penetrating an atmosphere along a line defined by cylindrical coordinates (ρ, θ) will experience a bending angle $\mathbf{\Theta}(\rho, \theta)$ (bold font denotes a vector quantity, in this case with components in the $\hat{\rho}$ and $\hat{\theta}$ directions) given by the gradient of the refractivity $\nu(r, \phi)$ integrated along the path of the ray. Since the bending angle in the present situation is always small ($\Theta < 0\farcs9$), the path of the integration can to a very good approximation be considered a straight line parallel to the z axis,

$$\mathbf{\Theta}(\rho, \theta) = \nabla \int_{-\infty}^{\infty} \nu(r, \phi) dz. \tag{4.9}$$

The complexity of the case of a non-spherical atmosphere tilted with respect to the line of sight arises from the range of latitudes ϕ and the varying plane of refraction $\mathbf{\Theta}/|\Theta|$ experienced by each ray.

The observed flux of starlight which has penetrated Titan's atmosphere is a function of three competing factors. These can be expressed simply for a spherically symmetric atmosphere, as follows (EY92). The spreading of a bundle of rays by differential refraction as it traverses the atmosphere will lead to a reduction of the flux by a factor of $d\rho/d\rho'$. The flux may be further reduced by absorption or scattering in Titan's atmosphere, which can be expressed as the exponential of the negative of the total opacity integrated along the path of the ray $\tau_{\rm obs}(\rho)$. Finally, the curvature of Titan's limb in the plane perpendicular to the starlight will cause rays to converge within the shadow, enhancing the flux by a factor proportional to the radius of curvature divided by the distance of the observer from the center of curvature ρ/ρ'. Combining these terms, the flux of starlight emerging from a spherically symmetric atmosphere, normalized to that incident, will be

$$\Phi(\rho) = \frac{\rho}{\rho'} \frac{d\rho}{d\rho'} \exp[-\tau_{\rm obs}(\rho)]. \tag{4.10}$$

In the absence of spherical symmetry, it is perhaps more intuitive to think of the normalized

flux as the ratio of the area of a bundle of rays in the planet plane $\rho d\rho d\theta$ to the area of the bundle in the observer plane $\rho' d\rho' d\theta'$, attenuated by the gas or scattering opacity,

$$\Phi(\rho,\theta) = \frac{\rho d\rho d\theta}{\rho' d\rho' d\theta'} \exp[-\tau_{\rm obs}(\rho,\theta)]. \tag{4.11}$$

To evaluate Eq. 4.11, we must first calculate the deflection angle $\mathbf{\Theta}(\rho,\theta)$, then trace the deflected rays to their destination (ρ',θ') in the observer plane. In terms of the components of $\mathbf{\Theta}$ in the $\hat{\rho}$ and $\hat{\theta}$ directions, this transformation can be expressed as

$$x'(\rho,\theta) = \rho\sin\theta + \Theta_\rho \sin\theta + \Theta_\theta \cos\theta, \tag{4.12}$$

$$y'(\rho,\theta) = \rho\cos\theta + \Theta_\rho \cos\theta - \Theta_\theta \sin\theta, \tag{4.13}$$

$$\rho'(\rho,\theta) = \sqrt{x'^2 + y'^2}, \tag{4.14}$$

$$\theta'(\rho,\theta) = \tan^{-1}(x'/y'). \tag{4.15}$$

4.4.4 Atmospheric model

In order to determine the deflection angle of a ray penetrating Titan's atmosphere (Eq. 4.9), we need a model for the refractivity $\nu(r,\phi)$ as a function of radius and co-latitude. The model must include the effects of planetary rotation and zonal wind, as well as the varying force of gravity over this broad region of Titan's atmosphere. We can describe the rotation of the atmosphere as the sum of the rotation rate of Titan $\omega_{\rm s}$ and that of zonal winds with a speed $V_{\rm w}(r,\phi)$,

$$\omega(r,\phi) = \omega_{\rm s} + \frac{V_{\rm w}(r,\phi)}{r\sin\phi}. \tag{4.16}$$

In hydrostatic equilibrium, the pressure gradient will balance the sum of the gravitational and centrifugal accelerations experienced by a parcel of this atmosphere times the mass density $\rho(r,\phi)$ of the gas. We can express the r and ϕ components of this force balance as

$$\left(\frac{\partial P}{\partial r}\right)_\phi = \rho\left(-g + \omega^2 r\sin^2\phi\right), \tag{4.17}$$

$$\left(\frac{1}{r}\frac{\partial P}{\partial \phi}\right)_r = \rho\omega^2 r\sin\phi\cos\phi, \tag{4.18}$$

where $g = GM/r^2$ and the partial derivatives are taken at constant ϕ and r, respectively.

For any realistic zonal winds, the gravitational acceleration will be much larger than the radial term of the centrifugal acceleration, so we can approximate Eq. 4.17 with the more familiar equation

$$\left(\frac{\partial P}{\partial r}\right)_{\phi} = -\rho g. \tag{4.19}$$

Rearranging this expression,

$$\frac{1}{\rho} = -g\left(\frac{\partial r}{\partial P}\right)_{\phi}, \tag{4.20}$$

we substitute it into Eq. 4.18,

$$-g\left(\frac{\partial r}{\partial P}\right)_{\phi}\left(\frac{\partial P}{r\partial \phi}\right)_{r} = \omega^2 r \sin\phi\cos\phi, \tag{4.21}$$

leading to the following partial differential equation which describes the shape of surfaces of constant pressure;

$$\left(\frac{\partial r}{\partial \phi}\right)_{P} = -\frac{1}{g}\omega^2 r^2 \sin\phi\cos\phi. \tag{4.22}$$

Equation 4.22 can be integrated along surfaces of constant pressure to determine their radius as a function of co-latitude. If these surfaces deviate only slightly from spherical, then we can move r^2 and g out of the integral, leading to the following approximate solution (Ingersoll, 1970)

$$r(P,\phi) \approx r(P,\phi_0)\left(1 - \frac{r(P,\phi_0)^3}{GM}\int_{\phi_0}^{\phi}\omega(P,\phi')^2 \sin\phi'\cos\phi' d\phi'\right). \tag{4.23}$$

An exact solution for $r(P,\phi)$ is given by Lindal *et al.* (1985), but Eq. 4.23 represents a sufficiently good approximation at Titan's slow rotation rate. The integral in Eq. 4.23 describes the shape of surfaces of constant pressure, which for constant composition and temperature will coincide with surfaces of constant refractivity. In the context of this simplified model, Eq. 4.23 can be thought of as an altitude correction to the pressure structure of Titan's atmosphere, due to the presence of zonal winds.

We compute the pressure as a function of radius at any fixed co-latitude ϕ by substituting the ideal gas law into Eq. 4.19 and expanding g,

$$\frac{1}{P}\frac{dP}{dr} = -\frac{\mu}{kT}\frac{GM}{r^2}, \tag{4.24}$$

where k is Boltzman's constant and μ is the mean molecular weight. Solutions to this differential equation will be of the form

$$P(r,\phi) = P_0 \exp\left[\frac{\mu GM}{kT}\left(\frac{1}{r} - \frac{1}{r(P_0,\phi)}\right)\right], \tag{4.25}$$

where the pressure is normalized to P_0 on a reference surface $r(P_0,\phi)$ whose shape is given by Eq. 4.23. The refractivity $\nu(r,\phi)$ can be expressed in terms of the pressure $P(r,\phi)$ and the refractivity of a gas of identical composition at standard temperature and pressure $\nu_{\rm STP}$ as

$$\nu(r,\phi) = \frac{P(r,\phi)}{kT}\frac{\nu_{\rm STP}}{L}, \tag{4.26}$$

where L is Loschmidt's constant. Substituting Eq. 4.25 into Eq. 4.26, we can compute the refractivity at any location in the isothermal region of Titan's stratosphere.

4.4.5 Wind model

There are several possible strategies for parametrizing the zonal winds, and their effect on Titan's stratospheric structure. Rather than use our model to solve directly for the wind velocities, we follow the example of H93, solving instead for the shape of surfaces of constant refractivity in Titan's stratosphere. The choice is motivated by the fact that it the shape of Titan's limb to which these observations are most directly sensitive, not the wind field. Following H93, we express the radius of surfaces of constant pressure (equivalent to surfaces of constant refractivity for constant composition and temperature) as

$$r(P,\phi) = b[1 + f(b,\phi)], \tag{4.27}$$

where $b = r(P,\phi_0)$ is the radius at a reference co-latitude ϕ_0. Substituting Eq. 4.27 into Eq. 4.23, we find

$$f(b,\phi) \approx -\frac{b^3}{GM}\int_{\phi_0}^{\phi} \omega(P,\phi')^2 \sin\phi' \cos\phi' d\phi'. \tag{4.28}$$

We then parametrize $f(b,\phi)$ in terms of the coefficients $f_l(b)$ of a truncated sum of Legendre polynomials,

$$f(b,\phi) = \sum_{l=0}^{N} f_l(b) P_l(\cos\phi). \tag{4.29}$$

The function with which we describe the shape of constant pressure surfaces must fulfill

several requirements, placing restrictions on the possible combinations of coefficients f_l. Regardless of its direction, any zonal flow in the atmosphere will contribute a centrifugal acceleration term to the local pressure balance oriented radially outward from Titan's rotation axis and parallel to the equatorial plane. In an isothermal stratosphere in hydrostatic equilibrium, this equator-ward force must be balanced by an equator-ward positive pressure gradient along constant-altitude surfaces. Therefore, in the presence of zonal winds, surfaces of constant pressure can only slope monotonically downward from equator to pole. This requirement is illustrated mathematically be rewriting Eq. 4.22 as

$$\frac{1}{\sin 2\phi}\left(\frac{\partial r}{\partial \phi}\right)_P = \frac{\omega^2 r}{2g} \geq 0. \tag{4.30}$$

H93 incorrectly conclude from Eq. 4.30 that the function f must be symmetric across Titan's equator, and consequently require that all odd coefficients $f_1, f_3, \ldots$ in their expansion be equal to zero. Though this strict requirement does ensure the satisfaction of Eq. 4.30, it is not a necessary condition. It is furthermore deceptive, leading H93 to infer the zonal wind patterns of the northern hemisphere in the absence of any observations of this region.

We include both even and odd coefficients in our expansion of f, but set the following requirements on f_1 and f_2 to ensure the satisfaction of Eq. 4.30. To ensure that $\partial f/\partial\phi = 0$ at the equator, we require

$$f_1(b) = \frac{\partial}{\partial \phi}\left[\sum_{l=2}^{N} f_l(b) P_l(0)\right]. \tag{4.31}$$

In practice, the sum needs only be taken over odd terms $l = [3, 5, \ldots]$. The positive and negative slope of f in the northern and southern hemispheres, respectively, can be assured by substituting Eq. 4.29 into Eq. 4.30 and solving for f_2,

$$\frac{\frac{\partial}{\partial\phi}\left[\sum_{l=0}^{N} f_l(b) P_l(\cos\phi)\right]}{\sin 2\phi} \geq 0, \tag{4.32}$$

$$\frac{\frac{\partial}{\partial\phi}\left[f_1(b)\cos\phi\right] + \frac{\partial}{\partial\phi}\left[\sum_{l=3}^{N} f_l(b) P_l(\cos\phi)\right]}{\sin 2\phi} \geq \frac{-\frac{\partial}{\partial\phi}\left[f_2(b)\left(\frac{3}{2}\cos^2\phi + \frac{1}{2}\right)\right]}{\sin 2\phi}, \tag{4.33}$$

$$\min\left[\frac{-f_1(b)\sin\phi + \frac{\partial}{\partial\phi}\left[\sum_{l=3}^{N} f_l(b) P_l(\cos\phi)\right]}{\sin 2\phi}\right]_b \geq \frac{3}{2} f_2(b). \tag{4.34}$$

The coefficient f_0 provides the altitude normalization of the pressure structure of the

atmospheric model, and is fixed with respect to higher coefficients by

$$f_0(b) = -\sum_{l=1}^{N} f_l(b) P_l(\cos\phi_0). \tag{4.35}$$

We normalize the pressure in the model atmosphere to that at the reference radius $r_0 =$ 2775 km, extrapolating in altitude and latitude using Eq. 4.25 and 4.28. In practice then, only coefficients $l > 3$ are allowed to vary freely to fit the observations, while f_0 and f_1 are fixed by Eqs. 4.35 and 4.31, and a strict upper limit is placed on f_2 (Eq. 4.34).

We next make the simplifying assumption that the wind field is constant with altitude: $\omega(P, \phi) = \omega(\phi)$. This is necessary to make the problem tractable, and justified by the rather narrow altitude range over which these observations are sensitive to the wind. We will test this assumption by comparing the wind field derived from near and far-limb refracted stellar images, which sample each hemisphere of Titan at slightly different altitudes. Thus, we seek only a single set of N Legendre polynomial coefficients $f_l(b) = f_l$.

Finally, the wind speed as a function of co-latitude and radius can be recovered by differentiating the limb shape with respect to co-latitude,

$$\omega(\phi)^2 = -\frac{GM}{b^3 \sin\phi\cos\phi}\frac{d}{d\phi}\left(\sum_{l=0}^{N} f_l P_l(\cos\phi)\right). \tag{4.36}$$

4.4.6 Numerical solution

We now have the equations necessary to compute the refractivity at every point in an isothermal atmosphere with an arbitrarily complex (but constant with respect to altitude) wind field. We next need to integrate the refractivity along the path of a ray and trace its subsequent trajectory to the Earth. While analytically solving the path integral in Eq. 4.9 would be arduous, computing it numerically proves simple and intuitive. We choose a set of grid points with cylindrical coordinates (ρ_i, θ_j) which represent the locations surrounding Titan's limb at which the line-of-sight refractivity will be computed. Each of these possible trajectories through Titan's atmosphere is further divided into k segments at locations z_k. Replacing the gradient operator and integral in Eq. 4.9 with their finite difference

equivalents, we can write

$$\mathbf{\Theta}(\rho_i, \theta_j) \approx \left(\frac{\Delta}{\Delta \rho_i} \hat{\rho} + \frac{1}{\rho} \frac{\Delta}{\Delta \theta_j} \hat{\theta} \right) \sum_k \nu[r(\rho_i, z_k), \phi(\rho_i, \theta_j, z_k)] \Delta z_k, \tag{4.37}$$

where Δ represents the difference between neighboring grid points. Cylindrical coordinates (ρ_i, θ_j, z_k) are converted to spherical coordinates (r_l, ϕ_m, λ_n) using Eqs. 4.6–4.8. We illustrate these calculations in Fig. 4.9, which displays the refractivity summed along lines of sight through a Titan-like atmosphere with rapid, uniform rotation. In this case, the refractivity has been summed on a Cartesian grid with spacing of 20 km.

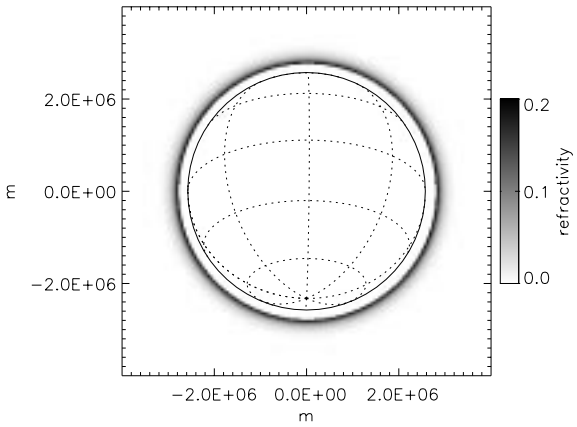

Figure 4.9: Illustration of path-integrated refractivity through a Titan-like atmosphere with uniformly rotation $\omega = 1.2 \times 10^{-4}$ s^{-1}, corresponding to an equatorial wind speed of $V_{\rm w} = 340$ m s^{-1}. Surfaces of constant refractivity bulge outward by 50 km over the equator. The calculation was cut off at 200 km above Titan's solid surface, shown as a latitude-longitude grid.

The extension of the Eq. 4.11 describing the normalized flux to this finite difference model is equally straightforward,

$$\Phi(\rho_i, \theta_j) \approx \frac{\rho_i \Delta \rho_i \Delta \theta_j}{\rho' \Delta \rho' \Delta \theta'} \exp[-\tau_{\rm obs}(\rho_i, \theta_j)]. \tag{4.38}$$

Fig. 4.10 displays the normalized observer-plane flux for the same uniform-rotation model atmosphere. Note, however, that only the flux contributed by the near-limb refracted image is displayed, underestimating the strength of the central flash.

Equations 4.37 and 4.38 give the observer-plane location and flux of a ray incident anywhere on Titan's atmosphere. We must interpolate these results to predict the angular deflection and flux observed from any given location in the observer plane which does not correspond precisely with that of a traced ray. This technique requires an exceedingly dense grid of rays to first be traced through the atmosphere, since the divergence of these rays

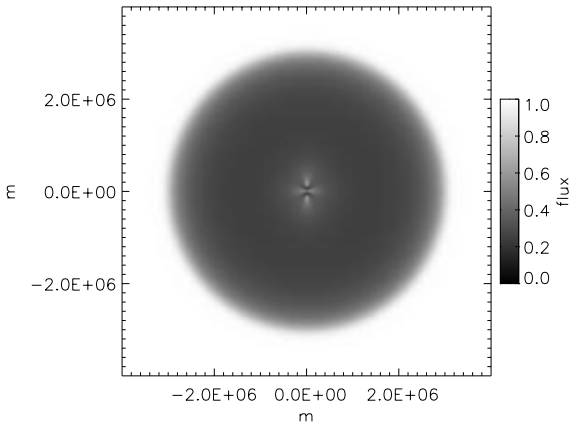

Figure 4.10: Normalized flux in the observer plane due to only the near-limb refracted image, for the same uniformly rotating atmosphere as Fig. 4.9. Light is focused to 4 points near the shadow center, at the centers of curvature of the projected limb. This is only one component of the central flash, which is further reinforced by an intensification of the far-limb image and the appearance of two further refracted beams within the evolute.

near the center (and far limb) of the shadow is substantial. The models presented in this chapter use a radial spacing of $\Delta\rho = 250$ m, angular spacing $\Delta\theta = 0.^{\circ}5$, dividing the rays into segments of length $\Delta z = 20$ km, for a total of $N \approx 3 \times 10^7$ grid points. At a given location in the observer plane (i.e. that of Palomar Observatory at a particular time), we bi-linearly interpolate the planet plane coordinates and observer plane flux of the nearest traced rays, with respect to their planet plane coordinates (ρ', θ').

4.4.7 Geometric and instrumental effects

The atmospheric and ray tracing models presented in Sections 4.4.3–4.4.6 predict the planet plane origin and flux of a ray reaching any location in the observer plane. To compare these to the observed relative position and flux of stellar images on the detector, we must determine the location of Palomar Observatory in the observer plane as a function of time, and convert planet plane coordinates (defined with respect to Titan's center) to detector coordinates.

We approximate the trajectory of Palomar Observatory across Titan's shadow with two second-order polynomials for the observer plane coordinates x' and y', expressed in vector form as

$$\begin{pmatrix} x' \\ y' \end{pmatrix} = \begin{pmatrix} x'_0 \\ y'_0 \end{pmatrix} + \begin{pmatrix} x'_1 \\ y'_1 \end{pmatrix} t + \begin{pmatrix} x'_2 \\ y'_2 \end{pmatrix} t^2. \tag{4.39}$$

where t represents the time in hours since 0:00 UTC on 20 December 2001. We can equivalently describe Titan's apparent trajectory across the sky in terms of second-order polyno-

mials for the apparent right ascension α and declination δ of Titan's center,

$$\left(\begin{array}{c} \alpha \\ \delta \end{array} \right)_{\rm Titan} = \left(\begin{array}{c} \alpha_0 \\ \delta_0 \end{array} \right) + \left(\begin{array}{c} \alpha_1 \\ \delta_1 \end{array} \right) t + \left(\begin{array}{c} \alpha_2 \\ \delta_2 \end{array} \right) t^2. \tag{4.40}$$

Our trajectory in the observer plane corresponding to each star and the apparent trajectory of Titan on the sky are related by

$$\left(\begin{array}{c} x' \\ y' \end{array} \right) = D \left(\begin{array}{cc} -\cos\psi_{\rm NP} & \sin\psi_{\rm NP} \\ \sin\psi_{\rm NP} & \cos\psi_{\rm NP} \end{array} \right) \left[\left(\begin{array}{c} \alpha \\ \delta \end{array} \right)_{\rm star} - \left(\begin{array}{c} \alpha \\ \delta \end{array} \right)_{\rm Titan} \right], \tag{4.41}$$

where D is the distance to Titan, $\psi_{\rm NP}$ is the apparent position angle of Titan's north pole ($\psi_{\rm NP} = 356\overset{\circ}{.}39$, measured counter-clockwise from celestial north), and the rotation matrix has been modified to account for the opposing definitions of α and x'.

Titan's direction and rate of motion on the sky can be predicted with high accuracy, but its position relative to the two stars in question is effectively unknown. Furthermore, we cannot accurately determine Titan's position in our images to better than ~ 0.5 pix, due to the unknown biases induced by albedo features of Titan's surface and in its atmosphere. We are therefore compelled to treat the relative separation zero-points of Titan with respect to each star as free parameters in our model. In practice, we solve for the position the fainter eastern star (hereafter star B), and the position of Titan at 0:00 UTC, with respect to the position of the brighter western component of the binary (star A). We compute the trajectory coefficients $\alpha_1, \alpha_2, \delta_1, \delta_2$ from the apparent astrometric positions of Titan over the time interval 4:52–5:52 UTC predicted by the JPL Horizons WWW program.

In addition to predicting the observer plane coordinates, Titan's known motion vector on the sky proves useful for determining the platescale and position angle of the detector, which are not otherwise well constrained. Though we cannot accurately determine the center of Titan's disk in the images, we do measure the satellite's apparent motion from one frame to the next by cross-correlation with the PSF-convolved disk model. Since the AO system remained locked on Titan, any motion on the detector is due to differential refraction (Roe, 2002a), flexure of optical components, or the intentional offsets applied to the AO system pointing center every 256 frames. We convert these apparent relative offsets to an apparent motion vector with respect to the stars by subtracting the centroid location

of star A. We then fit the apparent trajectory of Titan across the detector (with respect to star A) with the known motion vector on the sky, approximated by the polynomial coefficients $\alpha_1, \alpha_2, \delta_1, \delta_2$, and solve for the platescale and detector position angle. We find that a platescale of $p = (25.354 \pm 0.017)$ mas pix^{-1} and a position angle of the y (slow-scan) axis of $\psi_{\rm det} = 0\overset{\circ}{.}846 \pm 0\overset{\circ}{.}039$, where the uncertainties are dominated by the limited accuracy of the astrometric coordinates returned by the Horizons program. The platescale which we derive differs by 0.7% from that determined by Metchev *et al.* (2003) from observations of a single binary star of known separation, while the position angle is within the expected mechanical uncertainty.

In the final step of our model, we use the platescale and detector position angle derived above to convert planet plane positions to pixel locations of the detector. A refracted stellar image predicted to appear at planet cylindrical coordinates $(\rho\ \theta)_{\rm refr}$, viewed from observer plane Cartesian coordinates $(x'\ y')$, will have apparent sky coordinates

$$\begin{pmatrix} \alpha \\ \delta \end{pmatrix}_{\rm refr} = \begin{pmatrix} \alpha \\ \delta \end{pmatrix}_{\rm star} + \frac{1}{D} \begin{pmatrix} -\cos\psi_{\rm NP} & \sin\psi_{\rm NP} \\ \sin\psi_{\rm NP} & \cos\psi_{\rm NP} \end{pmatrix} \left[\begin{pmatrix} \rho\sin\theta \\ \rho\cos\theta \end{pmatrix}_{\rm refr} - \begin{pmatrix} x' \\ y' \end{pmatrix} \right]. \tag{4.42}$$

To determine its location on the detector, we rotate the coordinate system counter-clockwise by the detector position angle $\psi_{\rm det}$ and scale by the reciprocal of the platescale p,

$$\begin{pmatrix} x_{\rm det} \\ y_{\rm det} \end{pmatrix}_{\rm refr} = \frac{1}{p} \begin{pmatrix} -\cos\psi_{\rm det} & -\sin\psi_{\rm det} \\ -\sin\psi_{\rm det} & \cos\psi_{\rm det} \end{pmatrix} \begin{pmatrix} \alpha \\ \delta \end{pmatrix}_{\rm refr}. \tag{4.43}$$

The rotation matrices in Eqs. 4.42 and 4.43 have again been modified to account for conflicting sign conventions.

As emphasized in Section 4.2, we measure the *separation* of the binary components on the detector with far greater precision than their actual positions (e.g., their centroid locations.) Therefore, the final comparison of data to model is done against the difference in the predicted detector positions of the two stars. For example, during the occultation of star B (the first occultation), we measured the location of refracted images on Titan's limb in terms of their offset from the detector location of star A, which we will refer to here as $(x_{\rm det}\ y_{\rm det})_{\rm B-A}$. Combining Eqs. 4.42 and 4.43, and abbreviating the above rotation

matrices as $\mathbf{R}(\psi_{\rm NP})$ and $\mathbf{R}(\psi_{\rm det})$, we can express this as

$$\left(\begin{array}{c} x_{\rm det} \\ y_{\rm det} \end{array} \right)_{\rm B-A} = \frac{\mathbf{R}(\psi_{\rm NP})}{p} \left\{ \left(\begin{array}{c} \alpha \\ \delta \end{array} \right)_{\rm B-A} + \frac{\mathbf{R}(\psi_{\rm det})}{D} \left[\left(\begin{array}{c} \rho \sin\theta \\ \rho \cos\theta \end{array} \right)_{\rm refr} - \left(\begin{array}{c} x' \\ y' \end{array} \right) \right] \right\}. \quad (4.44)$$

where $(f\ g)_{\rm B-A}$ is the unocculted separation of the two stars.

4.4.8 Model fitting

The model presented in this section includes a simplified characterization of Titan's atmospheric structure, geometric factors which describe the motion of an observer across two shadows cast by Titan, and instrumental effects. Analysis of photometric occultation observations typically proceeds in several distinct stages. Instrumental parameters are first determined (the unocculted flux of the star, etc.), then the geometry of the event (e.g., by fitting the half-light times of several lightcurves), after which inferences regarding the nature of the occulting body itself can be made. We follow a different approach, solving simultaneously for most of the free parameters in the model. This method has the advantage of allowing us to correctly estimate the true uncertainties in correlated parameters. For example, a hemispheric contrast in the stratospheric zonal winds will be highly correlated with the inferred location of the observer in the plane of Titan's shadow. Since they rely on a different set of measurements, we do solve fot the platescale and detector position angle separately, as describe in the previous subsection.

The free and fixed parameters which define our occultation model are listed in Table 4.2. We solve for the free parameters by fitting the observed and model-predicted separation and flux ratio between near- and far-limb refracted stellar images and the unocculted star, optimizing the free parameters to minimize the square of the difference between observation and model divided by the estimated uncertainty of the observations. However, the estimated uncertainty in the flux ratio was first multiplied by a factor of 10 to reduce the model's sensitivity to the scintillation of the refracted stellar images. We used the Levenberg-Marquardt algorithm (Moré *et al.*, 1980), implemented in the IDL language by Markwardt (2003). This numerical optimization technique is robust and converges rapidly to a local minimum in the multi-dimensional χ^2 surface. We insure that this represents a global minimum by randomly varying the initial parameters.

Table 4.2: Free and fixed occultation model parameters

Description	Variable	Free	Value when fixed
Instrumental parameters			
Platescale	p	No	$25\farcs354 \pm 0\farcs017$ pix^{-1}
PA of y_{det} axis	$\psi_{\rm det}$	No	$0\fdg846 \pm 0\fdg039$
Stellar flux ratio	Φ_B/Φ_A	Yes	
Sky coordinates with respect to star A			
R.A. of star B	$\alpha_{\rm B-A}$	Yes	
Dec. of star B	$\delta_{\rm B-A}$	Yes	
R.A. of Titan	α_0	Yes	
	α_1	No	$-11\farcs4458 \pm 0\farcs0077$ hr^{-1}
	α_2	No	$-0\farcs032248 \pm 0\farcs00072$ hr^{-2}
Dec. of Titan	δ_0	Yes	
	δ_1	No	$0\farcs3067 \pm 0\farcs0063$ hr^{-1}
	δ_2	No	$-0\farcs01199 \pm 0\farcs00059$ hr^{-2}
Other geometric parameters			
P.A. of Titan N. Pole	$\psi_{\rm NP}$	No	$356\fdg39 \pm 0\fdg01$
Sub-Earth co-latitude	$\phi_{\rm se}$	No	$115\fdg53 \pm 0\fdg01$
Range to Titan center	D	No	$1.2153760 \times 10^{12} \pm 10^5$ m
Atmospheric parameters			
Reference altitude	r_0	No	2775 km
Reference co-latitude	ϕ_0	No	$83\fdg8$
N_2 refractivity	$\nu_{\rm STP}$	No	0.00029
Pressure at (r_0, ϕ_0)	P_0	Yes	
Mean molecular weight	μ	No	28.0 amu
Temperature	T	Yes	
Limb shape coefficients	f_l	Yes	

The random errors in the measured relative position and flux of the refracted stellar images (determined by Monte-Carlo simulations of each frame) have been propagated through the model to provide an estimate of the random uncertainty in the best-fit model parameters (Press *et al.*, 1992). This uncertainty, however, does not include the effect of the uncertainty in the various fixed model parameters such as timing errors, the platescale, and the detector orientation. Since we are fitting a large number of high signal-to-noise observations with a small number of model parameters, the averaged effect of the random errors is small, and that due to systematic errors dominates. For example, though the platescale in known to 0.07% , this nevertheless proves to be the largest source of uncertainty for the derived stratospheric temperatures. We determine the effect of systematic errors on the derived parameters by performing another Monte-Carlo simulation, this time choosing 20 random sets of Gaussian-distributed fixed input parameters to the model and calculating the resulting best-fit free parameters. The true uncertainty in the best-fit free parameter

Table 4.3: Uniform wind model

Description	Variable	Value[a]
Star flux ratio	Φ_B/Φ_A	0.905 ± 0.010
R.A. of star B	$\alpha_{\mathrm{B-A}}$	$1\farcs5190 \pm 0\farcs0008$
Dec. of star B	$\delta_{\mathrm{B-A}}$	$0\farcs1823 \pm 0\farcs0008$
R.A. of Titan	α_0	$63\farcs17 \pm 0\farcs06$
Dec. of Titan	δ_0	$-1\farcs20 \pm 0\farcs03$
Pressure normalization	P_0	0.84 ± 0.04 mbar
Temperature	T	177 ± 2 K
Limb shape coef.	f_0	-0.0038 ± 0.0007
	f_2	-0.0076 ± 0.0007
Reduced χ^2		3.04

a. Uncertainties include both random and systematic terms.

value is then taken to be its standard deviation over the 20 fits, added in quadrature to the uncertainty in that parameter due to random error in the observations.

4.5 Results

4.5.1 Uniformly rotating atmosphere

We first present our best-fit model of the occultation geometry and atmospheric parameters, for the simplified case of a uniformly rotating atmosphere with zero opacity. The altitude of surfaces of constant pressure in such an oblate, ellipsoidal atmosphere, can be described by setting all but the f_0 and f_2 coefficients of the Legendre series in Eq. 4.28 to zero. However, the normalization term f_0 is fixed to the value of f_2 (Eq. 4.35). In addition to the parameters describing the geometry of the occultation and the flux ratio of the stars, we allow the pressure normalization P_0 and the stratospheric temperature T to vary to best fit the observations, leaving us with 8 free parameters. The derived values can be compared to those determined from the Voyager 1 ingress radio occultation profile, $P_0 = 0.75$ mbar and $T = 169.4$ K at $r_0 = 2775$ km and $\phi_0 = 83\fdg8$ (Lindal *et al.*, 1983). The values of the parameters which best fit our observations are given in Table 4.3.

Figure 4.11 presents a graphical comparison of the predicted and observed position and flux of the refracted stellar images, relative to the unocculted star. The residuals (observation minus model) of these same data are displayed in Fig. 4.12. The observed position of the refracted stellar images closely matches that predicted throughout most of each occultation, but significant deviations occur near the midpoint of each, for both the

near- and far-limb images. Below approximately the half-light point, the observed flux of the refracted images deviates from that predicted, both due to scintillation in Titan's atmosphere, and attenuation of the starlight by haze.

The altitude of a surface of constant refractivity and the inferred zonal wind field corresponding to the best-fit values of the shape parameters f_0 and f_2 for the inform wind case are displayed in Fig. 4.13. Under the assumptions made, surfaces of constant refractivity Titan's atmosphere rise approximately 30 km from 65° north and south (the highest latitudes to which we are sensitive) to the equator, implying zonal winds reaching 270 ± 15 m s^{-1} above the equator. This approximately equal to the sound speed at this level (H93). These results are roughly consistent with the uniform rotation model best fit to the central flash observed during the 28 Sgr occultation by Titan (H93). As with those authors, however, we can discount this model since it does not successfully match the details of the observations.

To illustrate the region of Titan's stratosphere which is *not* well described by uniform rotation, we display the measured refracted stellar positions and model residuals for the near-limb refracted images only in the planet plane (Fig. 4.14). The large negative, then positive residuals seen near the midpoint of the first occultation in detector coordinates (Fig. 4.11A) occur as the light of the Eastern star passes thought the region of Titan's stratosphere viewed along the northern limb (Fig. 4.14). As the refracted image of this star climbs up and around Titan's northern limb (from celestial west to east), it follows the predicted location closely until it reaches approximately 40°N latitude. At this point, the trajectory of the refracted image markedly deviates from that predicted for a uniformly rotating (elliptical) atmosphere, accelerating towards the pole, lingering there, and finally accelerating to catch up to the predicted location again near 40°N latitude. No comparable deviations from the uniform wind model are seen above Titan's southern limb, despite the exact symmetry of the lines of sight. We can therefore immediately conclude that the atmospheric feature which causes this apparent deviation from the uniform wind model is asymmetric across Titan's equator, expressed primarily north of 40° N latitude. As we will demonstrate below, these residuals are precisely those expected in the presence of a strong jet at mid to high northern latitudes.

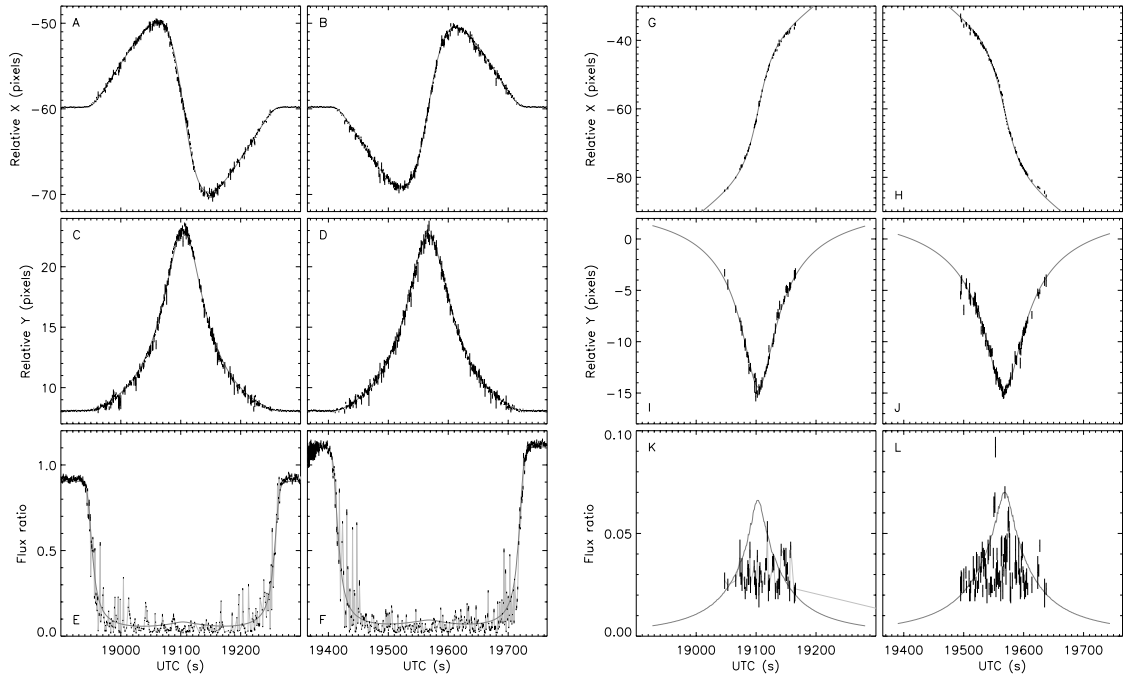

Figure 4.11: Measured and predicted position and flux of near-limb (*right*) and far-limb (*left*) refracted stellar images, with respect to that of the unocculted star, in detector coordinates. Observations are plotted in black with 1-σ error bars, while the predicted trajectory and flux of the refracted images for a uniformly rotating atmosphere is shown with a gray solid line. Residuals are shown in Fig. 4.12.

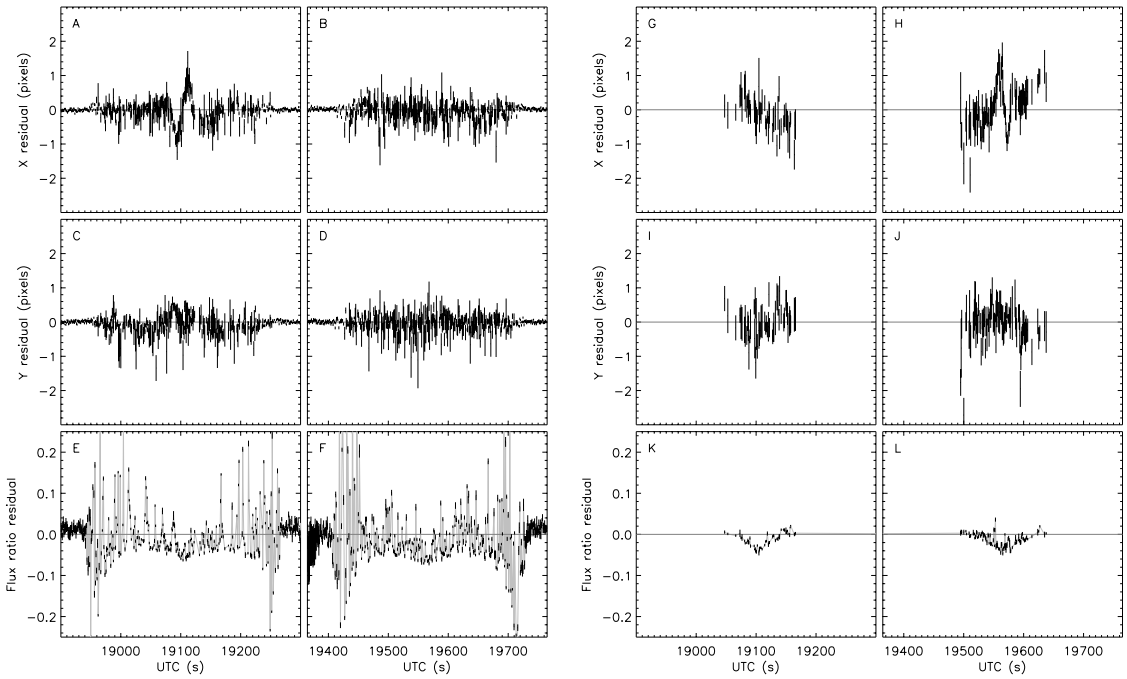

Figure 4.12: Residual between observed and predicted relative position and flux of the near-limb (*right*) and far-limb (*left*) refracted stellar images for the best-fit uniformly rotating atmosphere.

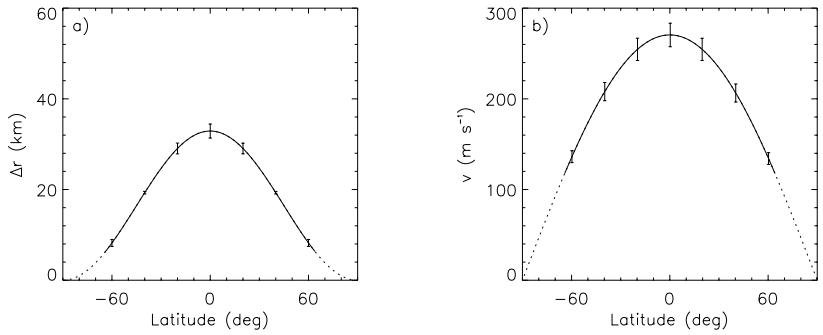

Figure 4.13: The shape of surface of constant refractivity (a) and inferred zonal wind field (b) in Titan's stratosphere, for uniform wind case. 1-σ error bars include both random and systematic errors. Solid lines indicate region over which Titan's limb is sampled.

4.5.2 Non-uniform wind model

The poor fit of the uniform wind model near Titan's north pole leads us to consider a more complex zonal wind field. As more Legendre terms are added to the series describing the shape of surfaces of constant pressure f, the fit to observed refracted stellar positions rapidly improves. The reduced χ^2 computed for the best-fit model parameters drops from $\chi^2 = 3.04$ when $l \leq 2$ (uniform wind field) to $\chi^2 = 2.72$ when $l \leq 4$, $\chi^2 = 2.63$ when $l \leq 6$, and $\chi^2 = 2.61$ when $l \leq 8$. More subjectively, we find that 8 terms are required to fit the horizontal scale of the departures from ellipticity which are observed. The best-fit parameters for such a model are given in Table 4.4.

Figures 4.15 and 4.16 present the fit and and residuals of the observations with respect to a non-uniform wind model of Titan's atmosphere, to Legendre order $l = 8$. The fine-scale detail of the motion of both the near- and far-limb refracted images over the *northern* limb of Titan can be correctly described by this non-uniform wind model, as is demonstrated by the obvious reduction in the model residuals in both the $x_{\rm det}$ and $y_{\rm det}$ dimensions (compare Fig. 4.12a and 4.12c to Fig. 4.16a and 4.16c for near-limb images, Fig. 4.12h and 4.12j to Fig. 4.16h and 4.16j for far-limb images). Unlike the northern limb, no deviation from ellipticity is detected along Titan's southern limb, to within the uncertainty of the observations. The trajectory followed by both the near- and far-limb refracted stellar images along Titan's southern limb matches that predicted by the uniform and non-uniform wind models equally well.

The shape of surfaces of constant refractivity which best matches the observed trajec-

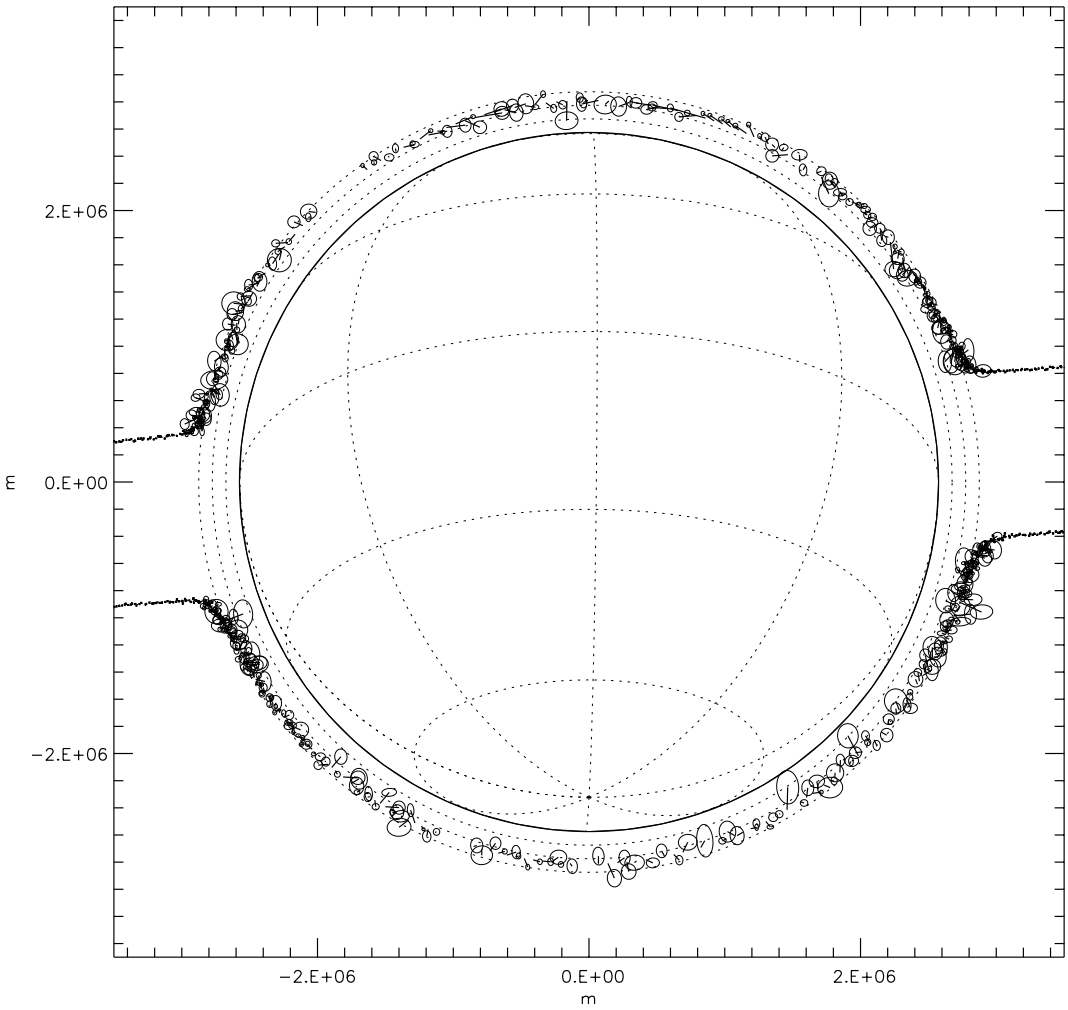

Figure 4.14: Measured and predicted position of near-limb refracted stellar images, displayed in the planet plane. Observations are plotted with 1-σ error ellipses, and a vector connects the measured position to that predicted for an atmosphere in uniform rotation. In effect, this displays the location in Titan's atmosphere from which each ray of starlight detected at Palomar Observatory originated, compared to that from which we would expect to have detected light if the atmosphere were in uniform rotation. A latitude-longitude grid marks the location of Titan's surface, with lines drawn every 30° of latitude and every 45° of longitude. Dotted lines above Titan's solid limb mark apparent altitudes of 100, 200, and 300 km above the surface.

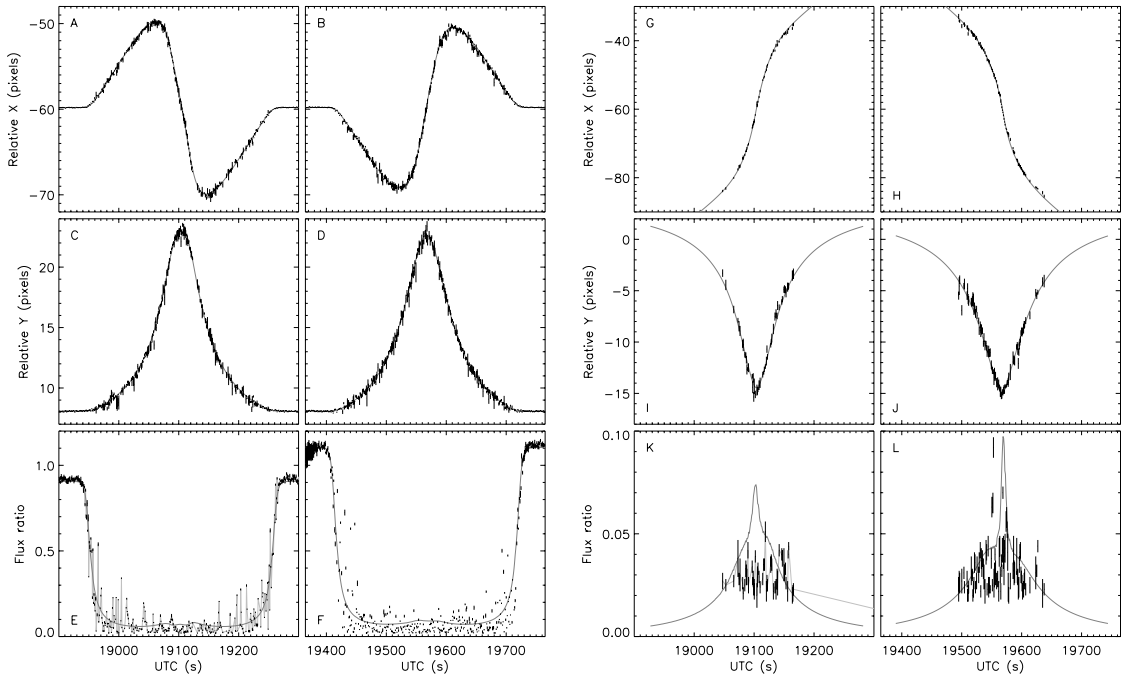

Figure 4.15: Measured and predicted position and flux of near-limb (*right*) and far-limb (*left*) refracted stellar images, with respect to that of the unocculted star, in detector coordinates. Predicted trajectory for the best-fit non-uniform ($l \leq 8$) wind field is shown with a gray solid line. Residuals are shown in Fig. 4.16.

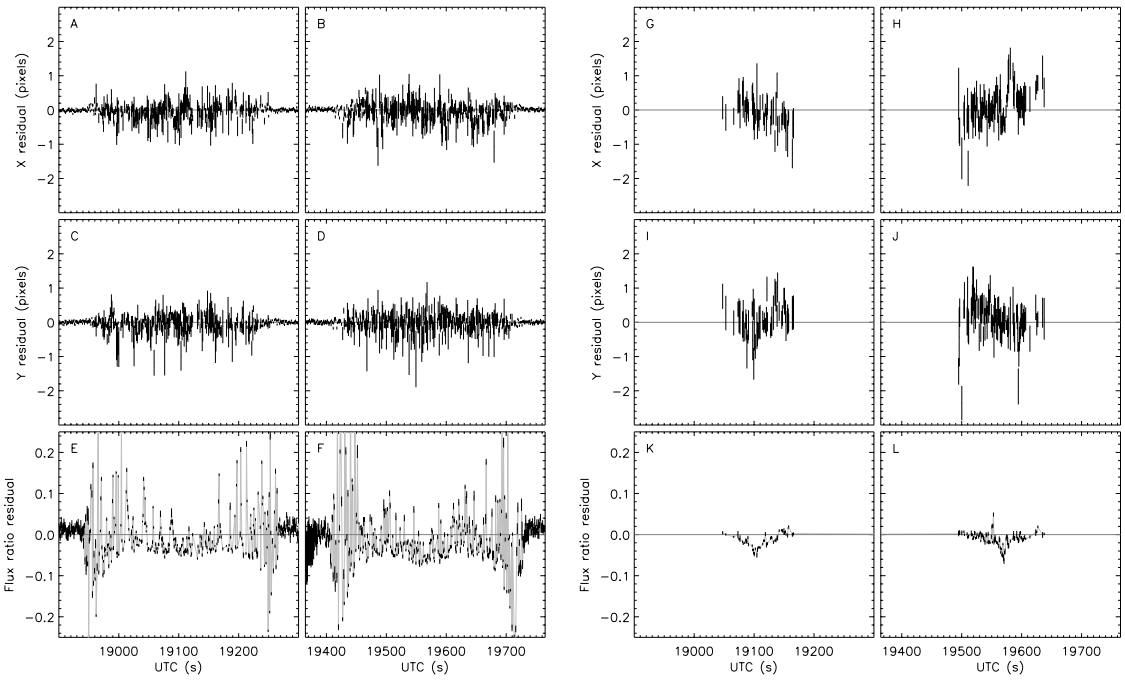

Figure 4.16: Residual between observed and predicted relative position and flux of the near-limb (*right*) and far-limb (*left*) refracted stellar images for the best-fit non-uniform ($l \leq 8$) wind model of Titan's atmosphere.

Table 4.4: Non-uniform wind model

Description	Variable	Value[a]
Star flux ratio	Φ_B/Φ_A	0.906 ± 0.010
R.A. of star B	$\alpha_{\mathrm{B-A}}$	$1\farcs5190 \pm 0\farcs0012$
Dec. of star B	$\delta_{\mathrm{B-A}}$	$0\farcs1824 \pm 0\farcs0010$
R.A. of Titan	α_0	$63\farcs166 \pm 0\farcs045$
Dec. of Titan	δ_0	$-1\farcs204 \pm 0\farcs031$
Pressure normalization	P_0	0.80 ± 0.04 mbar
Temperature	T	178.6 ± 1.9 K
Limb shape coef.	f_0	-0.00261[b]
	f_1	-0.00022[b]
	f_2	-0.00737[b]
	f_3	-0.00227 ± 0.00009
	f_4	-0.00379 ± 0.00011
	f_5	-0.00152 ± 0.00009
	f_6	-0.00162 ± 0.00010
	f_7	0.00015 ± 0.00008
	f_8	-0.00057 ± 0.00009
Reduced χ^2		2.61

a. Listed uncertainties include both random and systematic terms.
b. Value of coefficients f_0, f_1, f_2 are tied to $f_{l>2}$ by Eq. 4.31–4.35.

tories of the refracted stellar images is shown in Fig. 4.17a. In the magnified view provided by this binary stellar occultation, Titan's limb appears asymmetric, an oblate ellipsoid with a flattened north pole. The zonal winds implied by this figure are shown in Fig. 4.17b. The large uncertainties in wind speed in the equatorial region is entirely due to the geometry of this occultation. Due to the apparent trajectory of Titan with respect to the stars, no observations of Titan's atmosphere were made between 20°S and 5°N (see Fig. 4.14). Furthermore, observations made within less than $\sim$ 60 s of ingress or egress provide only a weak constraint due to the slight angular deflection of the starlight.

4.5.3 Stellar properties

Though the purpose of this analysis was the characterization of the shape of Titan's limb, the relative position and flux of the two components of the NV0435215+200905 star system are incidentally determined with considerable accuracy. The relative right ascension and declination of star B with respect to the brighter star A are given in Table 4.4, corresponding to a separation of $1\farcs530 \pm 0\farcs002$ at a position angle of $96\fdg85 \pm 0\fdg04$ clockwise of true north. To reiterate, the platescale and position angle to which these values are tied were not assumed *a priori*, but derived from Titan's known ephemeris and its apparent motion on the detector

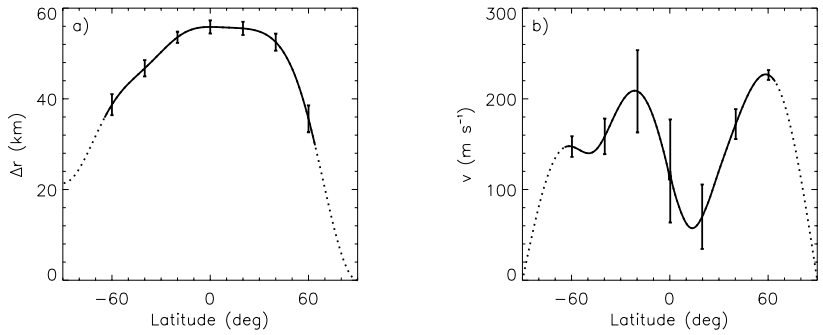

Figure 4.17: The shape of surface of constant refractivity (a) and inferred zonal wind field (b) in Titan's stratosphere, for the non-uniform wind case ($l \leq 8$). Error bars represent 1σ uncertainties which include the effect of systematic errors, such as the uncertain platescale, timing, and Titan's ephemeris.

with respect to the stars.

Though approximately constant during the two occultations, the measured flux ratio of the stars decreased gradually by 3% over the full hour of continuous observations. The primary cause of this variation appears to be optical distortion in the PHARO camera causing the platescale to vary by $\sim 0.3\%$ over the 360-pixel subaperture, which can lead to incorrect estimates of the flux ratio by the PSF cross-correlation technique (e.g., at locations on the detector where the platescale gradient is large). The occultations were fortuitously recorded at a location on the detector over which distortions were small, leading to a final estimate of the true K′ flux ratio of 0.906 ± 0.010. The separation, position angle, and K′ flux ratio of the stars determined here are consistent with the values given by Roe (2002b).

4.6 Discussion

The zonal wind field which best reproduces the positions and fluxes of the refracted stellar images detected during both occultations is displayed in Fig. 4.17b. A strong and narrow jet, with a peak wind speed of 230 ± 10 m s^{-1} at $\sim 60°$N, dominates the shape of Titan's northern limb. Though faster than previous estimates of Titan's zonal wind, this circumpolar jet is well below the 266 m s^{-1} sound speed in N_2 at 170 K (H93). Wind speeds drop to 110 ± 40 m s^{-1} at Titan's equator, and reach at least 140 ± 20 m s^{-1} over a broad region at mid to high southern latitudes. The peak at 20°S and the minimum at 15°N are probably not real, as the large error estimates in these regions attest. The wind direction remains

unconstrained by these observations, though the result of Kostiuk *et al.* (2001) suggest that it is probably prograde.

The northern hemisphere jet which we infer from the angular deflection of the light of two stars is similar to that deduced to exist in the southern hemisphere by H93 from photometry of the central flash of 28 Sgr (Fig. 4.3b). In common with Venus, the thermal wind balance in Titan's stratosphere is expected to be essentially cyclostrophic. Unlike Venus, however, Titan's 26.°7 obliquity leads to strong cooling of the winter polar stratosphere, ensuring seasonal variations in the zonal wind field and powering a jet in the winter mid-latitudes. At the time of the Voyager 1 flyby soon after northern spring equinox ($L_s = 9°$), a 17 K difference was detected between 70°N and 5°S at 0.4 mbar (Coustenis and Bezard, 1995), the northern pole remaining surprisingly cold despite the advancing season. Thermal contrasts are likely to be yet higher near solstice, when both occultations were observed.

The exact location of the peak wind speed in both occultation wind models is an artifact of the mathematical functions used to parametrize the wind field. However, its rough location and narrow appearance, its peak speed (H93 claim only an order of magnitude estimate), and the reduction of a factor of ~ 2 in wind speed between the jet and the equator, are all consistent. It is extremely encouraging, if somewhat surprising, that the zonal winds derived by these very different methods agree so closely, for opposite hemispheres in nearly opposite seasons ($L_s = 107°$ on 3 July 1989, $L_s = 259°$ on 20 December 2001).

H93 were unable to measure the zonal winds in Titan's summer hemisphere due to extinction of the starlight by Titan's haze and a lack of appropriately located observing stations. We find the winds in Titan's summer hemisphere to be both weaker, and less clearly focused in a circumpolar jet. This is consistent with the distribution of zonal winds predicted by some global circulation models of Titan. Hourdin *et al.* (1995) predict the existence at 1 mbar of a prograde jet with a peak speed of 120 m s^{-1} centered at 55° latitude in the winter hemisphere at solstice, and a prograde wind of 100 m s^{-1} at the equator tapering off towards the summer pole. An updated model in which the formation and transport of haze are coupled with the atmospheric dynamics predicts a similar zonal wind field with 30% higher speeds (Rannou *et al.*, 2002). The stronger circumpolar jet of this later model is caused by the concentration of haze at the winter pole, increasing the polar night cooling rate and thus the temperature gradient which supports the jet. The speeds which we measure are $\sim 40\%$ higher than those predicted by even this haze-coupled

circulation model, implying an even greater thermal contrast, due perhaps to Saturn's approaching perihelion in July 2003. In December 2001, Titan was being subjected to a 23% higher solar flux than at the time of the 28 Sgr occultation. Present global circulation models do not account for this potentially large asymmetry in Titan's seasons.

4.7 Conclusions

The high angular resolution achievable with adaptive optics on large-aperture telescopes is revolutionizing many areas of observational planetary science. The double occultation by Titan described in this chapter was an unusual event, particularly the convenient geometry and nearly equal brightness of the two stars. Though Titan regularly occults infrared-bright stars as seen from some location on Earth (1–2 yr^{-1} for stars with $K < 11$, some fraction of which will turn out to be multiple), the fixed location of large AO-equipped telescopes reduces this probability, for a given telescope, by roughly a factor of 10. Furthermore, the benign atmospheric conditions at Palomar Observatory on the night on 20 December 2001, and the flawless operation of both the AO system and near-infrared camera throughout the event, combined to produce a truly remarkable set of images of a unique astronomical phenomenon.

These observations record with exquisite detail the angular deflection of the starlight as Titan's atmosphere intervenes, a seldom-used but powerful probe of the atmospheric structure and wind field. The trajectory of refracted images of each star around Titan's limbs reveals the figure of surface of constant refractivity, which in turn are shaped by the zonal wind and temperature distribution in the stratosphere at $\sim 3 \times 10^{-4}$ bar (~ 240 km altitude). At the present season (late southern spring), Titan's stratospheric zonal wind field is strongly asymmetric across the equator. The winter hemisphere displays a powerful high latitude jet, reaching 230 ± 10 m s^{-1} at 60°N, faster than predicted by current global circulation models. This surprisingly high wind speed implies circulation around Titan pole in 11 hr. Zonal winds over the rest of the satellite are lower, and consistent in distribution, if not in magnitude, with the results of global circulation models.

The jet in Titan's winter stratosphere is cyclostrophically balanced against the strong temperature gradient at the edge of the polar night. The apparent underestimate of the wind speed by global global circulation models may be related to the inherent asymmetry

of Titan's seasons, which would lead to maximum stratospheric temperature contrasts at the present epoch.

Analogy between Titan's high latitude winter jet and the seasonal polar vortices of the Earth suggests that the jet may play an important role in the chemistry of the polar night region. A strong jet would act to restrict the diffusion of species built up during the polar night, possibly contributing to some of the unusually high concentrations of nitriles observed by Voyager 1 at Titan's north pole.

Finally, the strong winds which we infer to be present in Titan's stratosphere have clear operational implications for the Huygens probe, whose parachute is due to deploy at 180 km above Titan's surface in January 2005.

Chapter 5

Direct detection of variable tropospheric clouds near Titan's south pole

5.1 Introduction

Atmospheric conditions on Saturn's largest satellite Titan allow the possibility that Titan could possess a methane condensation and precipitation cycle with many similarities to the earth's hydrological cycle, a process which otherwise has no close analog within the solar system. Detailed study of Titan from the Voyager spacecraft and subsequent high resolution earth-based imaging, however, have shown no evidence for any tropospheric condensation clouds (Smith *et al.*, 1996; Combes *et al.*, 1997; Gibbard *et al.*, 1999; Coustenis *et al.*, 2001), even though recent low-resolution studies have provided indirect spectroscopic evidence for their transient existence (Griffith *et al.*, 1998, 2000). Here we present the first resolved images and spectra of Titan clearly showing transient cloud features, all of which are concentrated near the south pole. The discovery of these clouds demonstrates convincingly the existence of condensation and localized moist convection in Titan's atmosphere. Their location at the pole, near the current point of maximum solar heating, suggests that methane cloud formation is seasonally controlled by small variations in surface temperature and will move from the south to the north pole on a 15 year time scale.

Searching for clouds on Titan is best performed with high resolution images and spectra

[1]This chapter has been published as M.E. Brown, A.H. Bouchez, and C.A. Griffith, **Direct Detection of Variable Tropospheric Clouds Near Titan's South Pole**, *Nature*, 420, 795–797, 2002. It was written by M. Brown, with input from A. Bouchez. A. Bouchez performed the image processing and the radiative transfer modeling of the spectra, thereby calculating the altitude and aerial coverage of the clouds discovered near Titan's south pole.

at wavelengths between about 2.0 and 2.3μm. At these wavelengths, absorption of photons by Titan's methane ranges from negligible (2.00 to 2.05 μm) to nearly complete (2.17 to 2.29 μm), while absorption by Titan's haze is low (Griffith *et al.*, 1998, 2000). The transparent range allows images at these wavelengths to sense to the surface, while the complete range of methane absorption across the wavelength region allows spectra to probe all levels in Titan's atmosphere. High spatial resolution is critical to recognize any small distinct cloud against the surface of Titan.

5.2 Observations

Using the adaptive optics (AO) system at the W.M. Keck Observatory (Wizinowich *et al.*, 2000), we have obtained images with both the spatial resolution and spectral coverage critical for searching for clouds. AO achieves high spatial resolution by partially compensating for the smearing effect of turbulence in the earth's atmosphere and delivering a near diffraction- limited image. Images from five nights of observations (Fig. 5.1) demonstrate the remarkable spatial resolution achieved with the AO observations. Surface features which have been consistently imaged since 1995 are seen at their highest resolution ever. The images from 10 and 11 December 2001 and 28 February 2002 all show almost the same face of Titan, and the reproducibility and rotation of surface features is apparent. More remarkable, however, are the transient changes visible near the south pole of Titan. These changes are more apparent in polar projections of the images (Fig. 5.2). The bright unresolved spot on the southern limb in the 10 and 11 December images has disappeared by February. The February image instead shows a much larger brightening extending ∼1400 km from 80 to 70 south latitude. Numerous small morphologically similar isolated bright spots occur throughout the images but cannot be verified to be transient because of a lack of duplicate coverage of most longitudes.

5.3 Results

To determine the height in the atmosphere where the transient spots occur, we examined spectra from the 10 and 11 December bright southern spot and compared them to spectra obtained at a location 900 km directly east on the satellite, where the line-of-sight samples

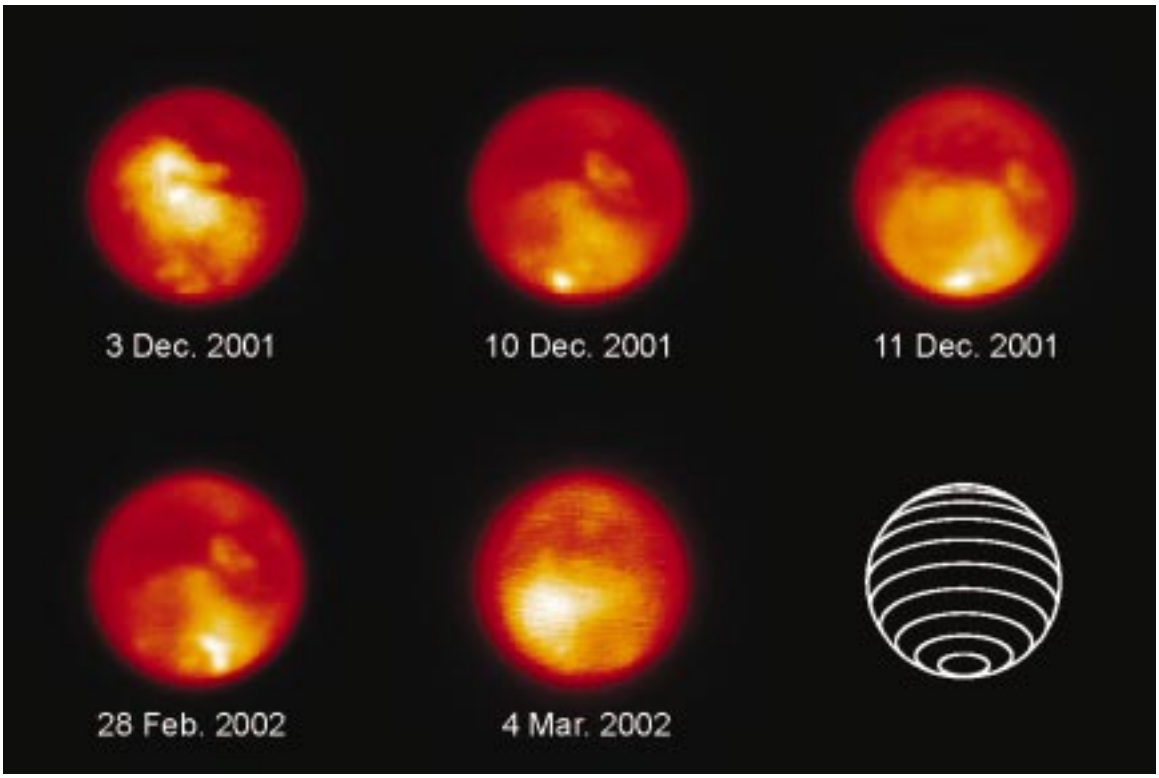

Figure 5.1: Images of Titan show the transient existence of cloud features near the south pole. Images and spectra from 2, 10, and 11 December 2001 were obtained using NIRSPEC, the facility near-infrared spectrograph (McLean *et al.*, 1998), while images (only) from 28 February and 4 March 2002 were obtained using NIRC2, the facility near-infrared AO imager. Images were obtained in the K' wavelength band, which extends from 1.96 to 2.29 μm, and have an angular resolution of 0.05 arcseconds (a linear resolution of 330 km on 10 December 2001) on the satellite. The images shown are combinations of from 4 to 20 individual images shifted to a common center, summed, and divided by an image of the individual pixel response function ("flat field"). The apparent elongation of the cloud feature on the 11 December 2001 image is a temporary artifact of the AO system. Owing to non-photometric observing conditions during some of the nights, no absolute flux calibration was obtained. The individual images are scaled to best see the polar clouds. The line figure shows every 15 degrees of latitude projected for Titan's subsolar latitude of -25.6 degrees at the time of the observations. Titan's subsolar longitudes at the times of observations were 69, 228, 249, 235, and 325 degrees for the 2, 10, and 11 December, and the 28 February and 3 March observations, respectively.

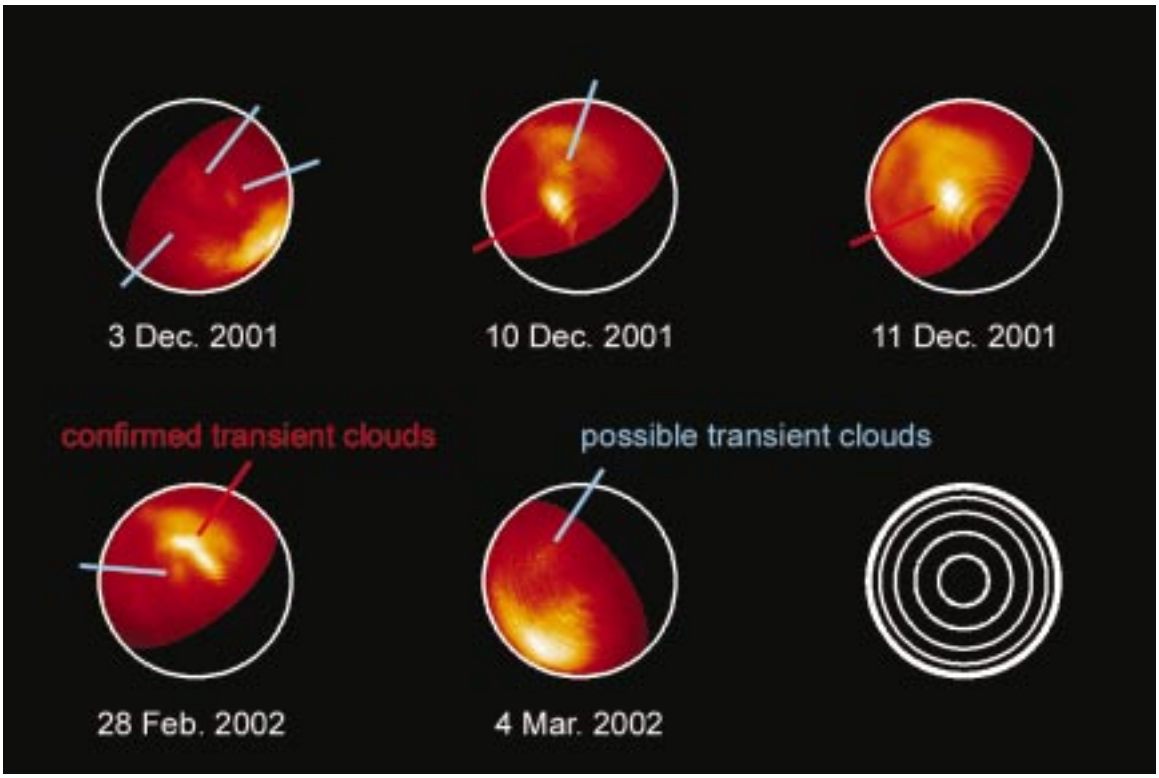

Figure 5.2: The transient polar clouds are best seen in polar projections of the images of Titan. A longitude of zero (facing Saturn) is straight up in these projections and longitude increases counter-clockwise. The line figure shows every 15 degrees of latitude. Confirmed transients (those for which we have multiple images confirming change) are labeled by red lines, while morphologically similar features whose transient nature is unconfirmed are labeled by blue lines. On 10 and 11 December the single brightest spot appears at longitude 150 ± 30, latitude 77 ± 3 south (the large errors in locating spots near the limb precludes any detection of cloud motion between the two nights). The 28 February images shows small brightenings at 200 ± 20, 87 ± 5 and 174 ± 10, 65 ± 5, but none at the precise location of that seen in December. Also visible is a much larger brightening between latitudes 70 and 80 S; nothing similar is seen in the December images. The projections were created by using the circular symmetry of the limb of Titan to define the center of the disk and then projecting the intensity onto a spherical grid. Errors in the position of the center of the disk of ± 0.02 arcseconds give errors in the projected longitude and latitude of features near the south pole of 20 and 5 degrees respectively. No intensity corrections are made for variations in the viewing angle.

the same latitude at an identical zenith angle of 65 degrees but no transient brightening occurs. A comparison between the 2 spectra (Fig. 5.3) shows that they are essentially identical beyond 2.16 μm. These regions of the spectrum contain strong methane absorption lines which saturate in the stratosphere of the satellite. At shorter wavelengths the methane absorption is progressively weaker so photons penetrate progressively deeper into the atmosphere until at a wavelength of 2.12 μm photons reach the surface. The two spectra diverge at a wavelength of 2.155 μm, which clearly requires a reflective layer somewhere between the stratosphere and the surface. Detailed plane-parallel radiative transfer calculations using the models of Griffith *et al.* (1998, 2000) of the difference between the two spectra shows that the bright spot is best modeled as an unresolved highly reflective cloud layer with a filling factor of 25% at an altitude of 16 ± 5 km above Titan's surface, in the middle of Titan's troposphere. The errors in this height estimate are dominated by uncertainties in tropospheric methane abundance; deviation from the plane-parallel assumption at this zenith angle is less than 4%. No changes are apparent in the altitude, intensity, or location of the cloud from 10 to 11 December. These images and spectra conclusively demonstrate the existence of transient clouds in the troposphere of Titan and point to the presence of a vigorous and currently active cycle of methane condensation and dissipation.

The December 2001 cloud has a brightness equivalent to $\sim$0.3% of the total brightness of the disk of Titan at these wavelengths, and can be explained by a single (foreshortened) cloud of 200 km diameter or smaller clouds with the same total area. The 28 February 2002 cloud is significantly larger, reflecting a flux equivalent to $\sim$1% of the total flux of Titan, and covering an apparent area of 4.4×10^5 km^2, implying a filling factor of only $\sim$5%.

These transient clouds will cause rapid changes to Titan's full-disk spectrum similar to the $\sim$0.5% variations previously observed shortward of 2.170μm and interpreted as evidence for such clouds (Griffith *et al.*, 2000). The difference in wavelength of spectral divergence between 2.170 μm in the full-disk spectra and 2.155 μm in the current spectra suggests a change in cloud height or latitude since the time of the previous observations.

5.4 Discussion

No obvious connection exists between these transient tropospheric clouds and the southern tropopause level scattering layer (Bouchez *et al.*, 2000; Lorenz *et al.*, 2001; Griffith *et al.*,

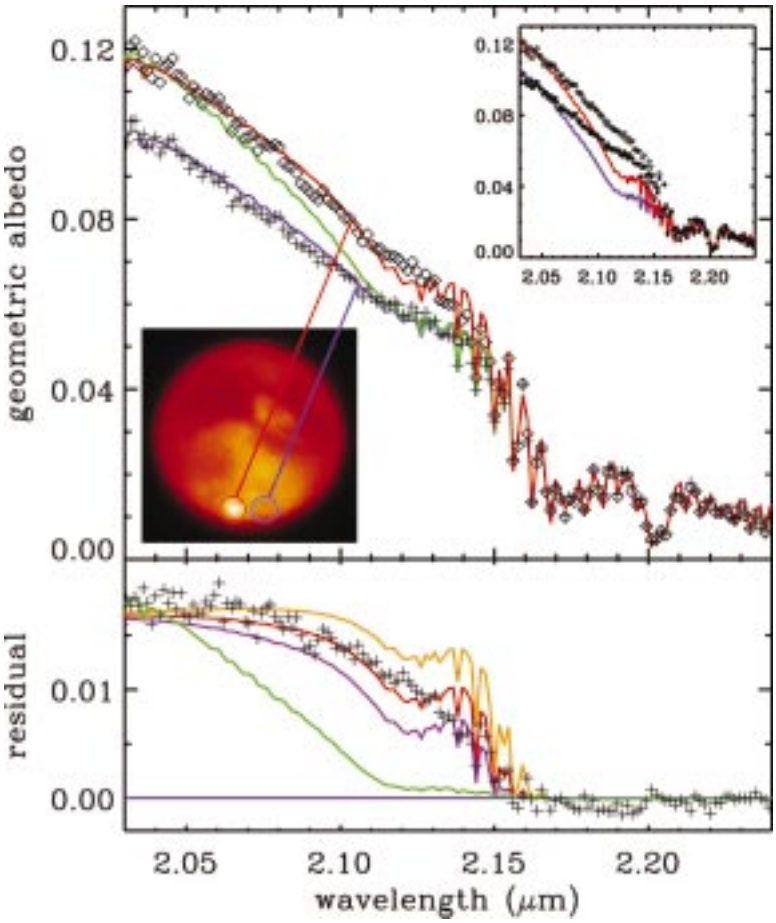

Figure 5.3: Spatially resolved spectra of the disk of Titan showing the height in the atmosphere of the transient features. A comparison of a spectrum of the 10 December 2002 transient brightening and of a location 900 km east on the disk which samples the surface and atmosphere at an identical zenith angle of 65 degrees shows that the transient brightening is caused by tropospheric clouds. The upper panel compares spectra from the regions labeled on the 10 December image with best fit radiative transfer models. The blue line shows the best-fit model to the non-cloud region, while the red line shows the effect of adding a bright scattering layer at 18 km. The green line demonstrates the poor fit obtained if an attempt is made to fit the transient brightening as a surface albedo effect. Neither spectrum can be modeled without the presence of a tropopause cirrus layer of optical depth 0.10±0.02 at 30-40 km (Bouchez *et al.*, 2000; Lorenz *et al.*, 2001; Griffith *et al.*, 2003; Bouchez *et al.*, 2003). The inset shows the best fit models without this tropopause cirrus. The bottom panel shows the difference between the two spectra and between models with clouds at 14 (purple), 18 (red), and 24 km (orange). The green line again shows the poor fit if the spectral difference is modeled purely with a change in surface albedo. The mismatches between the models and data are due to inaccuracies in the methane line strengths; these inaccuracies contribute the greatest uncertainty to the derived cloud height. The spectra were obtained simultaneously using a 0.054 arcsecond wide spectral slit centered on the brightening and placed east-west across the disk. Both spectra have been divided by the spectrum of the G4V star HD 32923 taken at an identical airmass of 1.02 to correct for effects of instrumental sensitivity, telluric absorption, and solar spectrum. The radiative transfer model uses doubling and adding techniques to approximate the equation of radiative transfer, along with line-by-line and Mie scattering calculations to incorporate gas absorption and scattering by particulates. The nominal value of methane humidity is that of Griffith *et al.* (2000); changes of factors of two in methane or allowing methane supersaturation do not significantly change the results.

2003; Bouchez *et al.*, 2003) which occurs at an altitude around 40 km and is visible in the spectra of Fig. 3. This layer has been observed since at least 1994 and has been variously described as a cloud, haze layer, or fog, but the true physical nature, composition, and cause remain unknown. Though this scattering layer is routinely observed, the lack of a consistent name has caused confusion as to its stability and even existence. We use the term "tropopause cirrus" as a morphological name for this distinct layer which describes its approximate altitude, small optical depth, and large areal coverage. At the time of observations, this cirrus layer covered the entire southern hemisphere at latitudes further south than 35 degrees (Bouchez *et al.*, 2003). The southern tropopause cirrus layer is not currently known to vary, though it is likely to change on seasonal time scales with changes in stratospheric haze chemistry and dynamics (Lorenz *et al.*, 2001).

The most striking property of these transient cloud events is their unexpected concentration near the south pole of Titan. While heating at southern summer solstice might be expected to drive polar convection, studies of tropospheric conditions on Titan have suggested an absence of seasonal variation (Hunten *et al.*, 1984; McKay *et al.*, 1997) and predicted that methane clouds, if present, should concentrate at the equator year-round (Tokano *et al.*, 1999). These hypothesized seasonal invariances come from consideration of the long radiative time scale of Titan's lower troposphere which does not allow tropospheric temperatures to appreciably change on seasonal timescales (Hunten *et al.*, 1984).

These predictions of invariance do not consider the effects of small seasonally varying surface temperatures, however, and instead examine only conditions measured during southern spring equinox at the time of the Voyager flyby. Even a very small seasonally and latitudinally varying surface temperature, which is a necessary consequence of Titan's widely varying seasonal insolation, will affect the magnitude of the surface sensible heat flux and change temperatures in the lower troposphere. If the lower tropospheric lapse rate is close to the boundary between stability and instability, as has been measured on Titan (McKay *et al.*, 1997; Lindal *et al.*, 1985; Lellouch *et al.*, 1989), a small additional heat flux can drive the creation of a thermally convective layer, the height of which will depend on the magnitude of the additional heat input and therefore on the surface temperature. Assuming the conditions least favorable to convection that have been inferred from Voyager measurements (McKay *et al.*, 1997), even a surface temperature rise of only 1 K is sufficient to cause a convective layer 7 km in height. If this convective layer reaches the point at

which methane saturates, the height of which is highly dependent on the methane humidity but is estimated to be ∼4 km in typical models (Griffith *et al.*, 2000; Hunten *et al.*, 1984; Lindal *et al.*, 1985; Lellouch *et al.*, 1989), methane condensation will render the air buoyant and drive clouds to the ∼15km levels observed (Awal and Lunine, 1994). In regions with lower surface temperatures, the convective layer will be smaller or even non-existent, and condensation will not occur.

At the time of our observations, Titan was approaching southern summer solstice, and, owing to Titan's obliquity of 27 degrees, the polar regions were in continuous sunlight and receiving more daily averaged insolation than any other spot on the satellite (and 50% more daily averaged insolation than the equator at equinox). We hypothesize that this insolation leads to a maximum surface temperature in these polar regions which drives a convective layer large enough to cause methane condensation and the ensuing moist convection. This hypothesis predicts that the location of these convective clouds will follow the location of maximum insolation (with some lag owing to the thermal inertia of the surface).

5.5 Acknowledgements

We thank E.J. Moyer and M.I. Richardson for enlightening conversations, D. Le Mignant, R. Campbell, M. Konacki, and J. Eisner for enthusiastically acquiring the NIRC2 data, S. Hörst for many nights of monitoring Titan in the cold, and the referees and editor for insightful commentary. This work was supported by a grant from the NSF Planetary Astronomy program.

Chapter 6

Seasonal changes in Titan's tropospheric clouds

6.1 Introduction

The discovery of large transient clouds in Titan's troposphere by Griffith *et al.* (1998) was unexpected. High resolution imaging studies of Titan's surface in the visible (Smith *et al.*, 1996; Richardson *et al.*, 2001; Ch. 2) and near-infrared (Combes *et al.*, 1997; Gibbard *et al.*, 1999; Meier *et al.*, 2000; Coustenis *et al.*, 2001) had revealed Titan's fixed surface albedo features, but despite careful searches had failed to conclusively detect clouds. Increasingly precise spectral observations next demonstrated that smaller clouds, covering $\sim$ 1% of Titan's disk, come and go on a daily basis (Griffith *et al.*, 2000). Yet the location of both the daily and occasional larger clouds remained unknown.

Adaptive optics observations with the Keck and Gemini telescopes in December 2001 clearly located Titan's daily clouds near the south pole (Brown *et al.*, 2002; Roe *et al.*, 2002) (Ch. 5). Individual clouds were observed to persist at least 24 hours in one case (Brown *et al.*, 2002), and vary in flux by 50% over 3 hr in another (Roe *et al.*, 2002), but little other information on their lifetimes, formation frequency, and size spectrum can be gleaned from these few observations (a total of 10 nights). Nor did these observations note anything resembling the large storm detected spectroscopically in 1995, which was inferred to have covered 7% of Titan's disk (Griffith *et al.*, 1998), increasing its 2.0 μm flux by 30%.

Frequent observations over many rotations, either resolved imaging or photometric monitoring, provide the best means of constraining many of these basic properties of Titan's transient clouds. A photometric approach, which ultimately proved inconclusive, is de-

scribed in Ch. 7. Here we present the results of an intensive imaging campaign performed primarily with the Palomar Hale 5-m telescope in the fall and winter of 2002–2003. The goal of this project was to understand the typical locations, lifetimes, formation frequency, and size spectrum of Titan's clouds, and constrain the wind field in the regions of Titan's troposphere in which clouds form. We also include in this study images of Titan taken on 8 nights between October 1997 and December 2002 with the W.M. Keck 10-m telescopes, which extend the temporal baseline of the study.

6.2 Observations

6.2.1 Palomar adaptive optics images, 2001–2003

Images of Titan were acquired on 16 nights between 20 December 2001 and 14 January 2003, using the JPL adaptive optics (AO) system and the Cornell-built PHARO camera/spectrograph at the Cassegrain focus of the Palomar Hale telescope (Table 6.1). The operation of the AO system and PHARO has been described in Ch. 3. All images were taken through a K′ filter (1.945–2.296 μm), and recorded at a platescale of $0\farcs02517$ pix^{-1}, with an integration time of 9.085 s. A minimum of 16 images were taken each night, with the telescope offset by $5''$ between each set of 4 to minimize the effect of bad pixels and uncertain flat-field calibration. Observing conditions ranged from photometric to thin high clouds.

Each set of dithered images was first grouped according to the location of Titan on the detector. For each location, a pixel-by-pixel median of the images not included was calculated and subtracted from each image in this subset, thus correcting for the detector bias, dark current, and the thermal sky background. All images were then divided by a map of the relative pixel gains (the flat-field map), which was calculated from the average of bias- and dark-current-subtracted twilight sky images taken the same night. Finally, pixels with abnormal gain properties, as determined from twilight sky images taken over a wide range of sky brightness, were replaced by the median of the surrounding good pixels.

After pre-processing, each night's images were sorted by resolution and only the best 8–16 frames retained. The quality metric used was the weighted sum of the spatial power spectrum of the image, where the weight at each spatial frequency is the variance of power spectra at that frequency. Thus the frequencies with highest variance, those near the

Table 6.1: Palomar AO observations

Date	UT	Am[a]	D[b]	Sub-Earth[c]	N[d]	Observers
20 Dec 2001	06:31–06:43	1.03	0.87	92.5,-25.5	8/25	A. Bouchez, M. Brown, M. Troy, R. Dekany
23 Sep 2002	11:42–11:45	1.12	0.79	210.5,-26.0	8/16	A. Bouchez, M. Troy, R. Dekany
24 Sep 2002	12:08–12:15	1.07	0.80	233.5,-26.0	16/32	A. Bouchez, M. Troy, R. Dekany
25 Sep 2002	11:29–11:36	1.12	0.80	255.4,-26.0	16/32	A. Bouchez, M. Troy, R. Dekany
26 Sep 2002	12:08–12:24	1.05	0.80	278.6,-26.0	16/64	C. Dumas
27 Sep 2002	11:50–12:05	1.07	0.80	300.9,-26.0	16/64	C. Dumas
14 Nov 2002	10:21–10:38	1.02	0.86	305.2,-26.0	16/64	M. Konacki
15 Nov 2002	10:30–10:54	1.03	0.86	327.0,-26.0	8/96	A. Bouchez, C. Trujillo
16 Nov 2002	09:01–09:16	1.03	0.87	348.2,-26.0	16/64	S. Metchev, C. Bian
17 Nov 2002	09:59–10:06	1.02	0.87	11.7,-26.0	16/32	S. Metchev, C. Bian
18 Nov 2002	09:35–09:42	1.02	0.87	33.9,-26.0	16/32	S. Metchev, C. Bian
24 Dec 2002	08:36–09:07	1.10	0.88	129.1,-26.3	16/160	J. Carson, E. Furlan, W. Forrest, K. Uchida
27 Dec 2002	08:03–08:10	1.05	0.88	196.4,-26.3	16/32	E. Furlan, L. Keller, K. Uchida, D. Watson
28 Dec 2002	07:52–07:59	1.04	0.88	218.9,-26.3	8/32	E. Furlan, L. Keller, D. Watson
12 Jan 2003	07:00–07:14	1.06	0.87	198.0,-26.4	16/64	S. Metchev
14 Jan 2003	05:31–05:38	1.02	0.87	241.9,-26.4	16/32	J. Eisner, S. Metchev

a. Airmass.
b. Diameter of Titan's disk (″).
c. West longitude and latitude of the sub-Earth point (°).
d. Number of frames used to compute the mean image, divided by the total number taken.

Table 6.2: Keck speckle observations

Date	UT	Airmass	Diam.	Sub-Earth	N[b]	Observers
24 Oct 1997	06:12–08:43	1.46–1.04	0.84	75.8,-9.5	21	A. Bouchez, M. Brown, C. Koresko
26 Oct 1997	06:21–07:39	1.38–1.12	0.84	121.1,-9.5	20	A. Bouchez, M. Brown, C. Koresko
02 Nov 1998	12:05–13:01	1.27–1.63	0.86	232.2,-14.9	6	A. Bouchez, C. Koresko, D. Muhleman
05 Nov 1998	11:41–12:52	1.24–1.65	0.85	300.0,-14.8	7	A. Bouchez, C. Koresko, D. Muhleman
06 Nov 1998	10:10–11:27	1.05–1.22	0.85	321.2,-14.8	6	A. Bouchez, C. Koresko, D. Muhleman
07 Nov 1998	06:40–07:59	1.26–1.06	0.85	340.5,-14.8	9	A. Bouchez, C. Koresko, D. Muhleman

a. Number of target-calibrator pairs used to compute mean image.

Table 6.3: Keck AO observations

Date	UT	Airmass	Diam.	Sub-Earth	Int.[a]	N[b]	Observers
28 Feb 2002	06:59–07:01	1.27	0.79	235.2,-25.7	5	12	D. Le Mignant, R. Campbell
29 Dec 2002	10:11–10:30	1.02	0.88	243.9,-26.3	60	8	J.-L. Margot, M. Brown

a. Integration time per frame (s).
b. Number of frames taken.

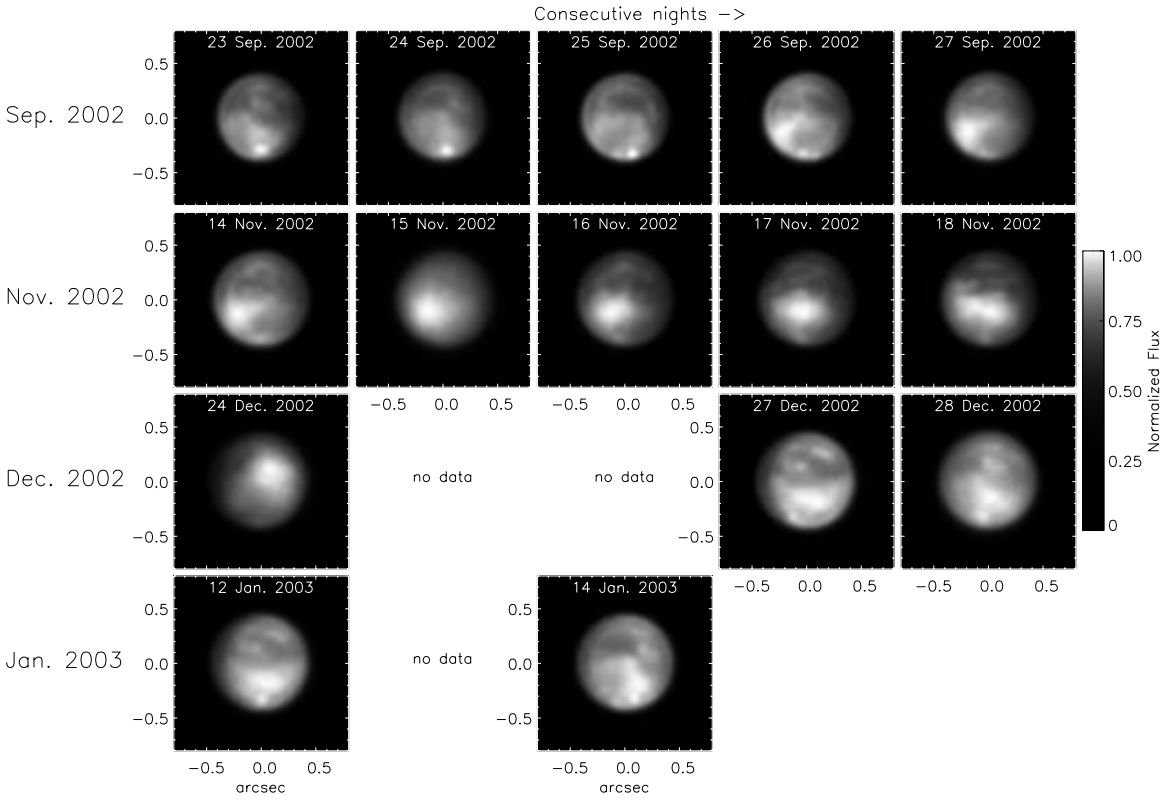

Figure 6.1: Palomar Hale telescope images of Titan in 2002–2003. An additional image taken on 20 December 2001 is included in this study and displayed in Figs 3.1c and 4.5. Bright, unresolved clouds can be identified near Titan's south pole on all but 3 night (27 September and 14–15 November).

resolution limit of that set of frames, are given highest weight and images with more power at those frequencies are retained.

The remaining images were averaged in a two-step process. A template image was first constructed by shifting all frames to an approximate common center (to the nearest pixel) based on the apparent location of Titan's limb, and averaging them. Each frame was next cross-correlated with the template image to the nearest 0.2 pix, and shifted to a common center by adding a phase ramp to the Fourier transform of the image. The mean of these 8–16 Fourier shifted images then constitutes our estimate of Titan's image on that night (Fig. 6.1). The standard deviation at each pixel location over the stack of shifted frames, divided by the number of frames minus 1, provides an estimate of the uncertainty of the pixel values in the mean image.

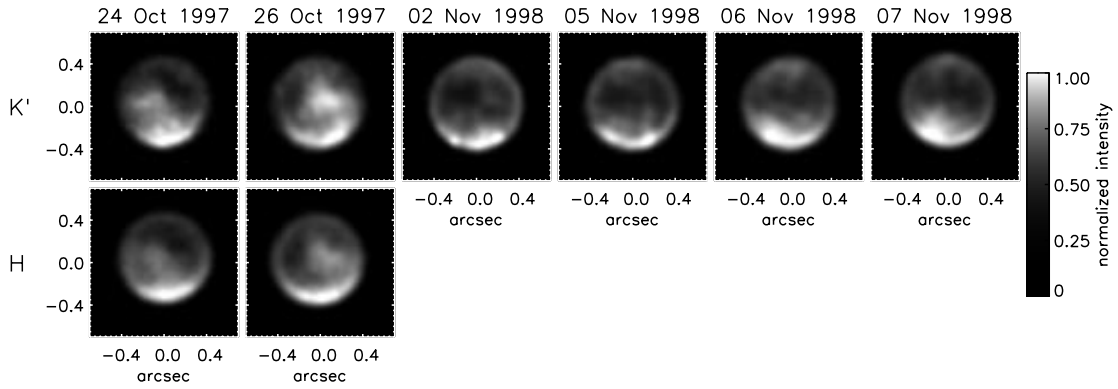

Figure 6.2: Keck-I speckle images of Titan in 1997 and 1998. H band images are included on the first two nights, displaying very similar surface and atmospheric features to those seen in the K′ images.

6.2.2 Keck speckle images, 1997–1998

Speckle observations of Titan taken in October 1997 and November 1998 used the near-infrared camera (Matthews and Soifer, 1994) with the deployable image converter (Matthews *et al.*, 1996) on the Keck-I telescope (see Table 6.2.). Alternating sets of 100 short (149 ms) K′ integrations were taken of Titan and two nearby unresolved calibrator stars, for for 1–2 hours per night. H band (1.491–1.824 μm) images were also acquired on some nights. The deployable image converter (Matthews *et al.*, 1996) provides a platescale of $0\farcs0206$ pix^{-1} over the 256×256 pixel detector.

We used a speckle reconstruction algorithm developed by Koresko *et al.* (1991), modified to account for field rotation during the observations. After bias and flat-field corrections, each frame was divided into 128×128 object and sky regions (the sky regions assembled from the detector corners). The mean power spectrum and bispectrum of the object and sky were then used to reconstruct Titan apparent Fourier phases and amplitudes, which were apodized by a Hanning function. Division by the identically reconstructed Fourier components of the unresolved calibrator star then returns an approximately diffraction-limited image of Titan.

Each paired set of Titan and calibrator star observations was processed independently, and finally averaged to recover a single nightly mean image of Titan. The uncertainty in this final image was estimated from the standard deviation of the constituent images, as

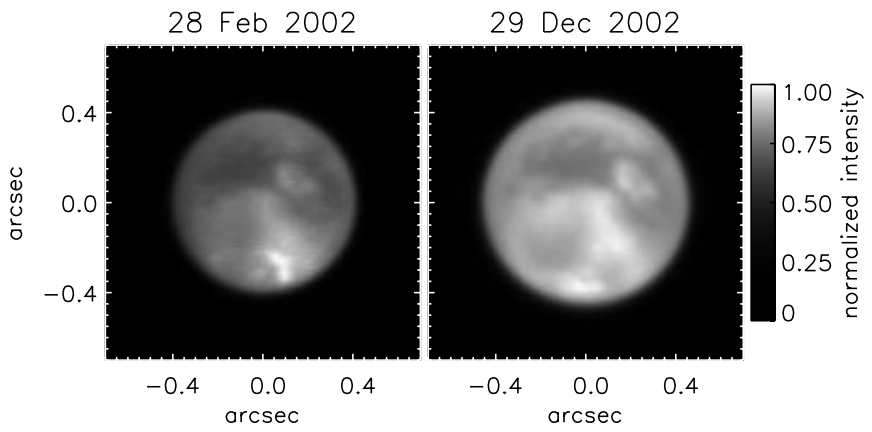

Figure 6.3: Keck-II AO images of Titan in 2002. Both images show complex, resolved transient clouds near the south pole. The 29 December image was taken in particularly stable atmospheric conditions, and may be the highest resolution image yet taken of Titan's lower atmosphere and surface.

with the adaptive optics frames. The nightly mean images are displayed in Fig. 6.2.

6.2.3 Keck adaptive optics images, 2002

We also include two images of Titan taken with the adaptive optics system (Wizinowich *et al.*, 2000) and NIRC2 camera on the Keck-II telescope (Table. 6.3). The first of these images has been previously published in (Brown *et al.*, 2002) but is included here for comparison. As with the Palomar observations, the adaptive optics control loop was locked on Titan, and run at its fastest possible rate. A series of 8–12 K′ images with 5 s or 60 s integration were acquired with the finest platescale camera ($\sim 0.005''$ pix^{-1}), arranged in a four-position dither pattern on the 1024×1024 pixel detector. These images were processed identically to those taken with the Palomar adaptive optics system, though the less variable correction quality allowed us to retain all processed images in the final nightly averages (Fig. 6.3).

6.3 Analysis

6.3.1 Surface albedo map

The purpose of our analysis is to measure the position and flux of the transient clouds recorded in the 24 nightly mean images included in this study. To do this, we must estimate

the PSF of each mean image, and the light contributed by scattering of sunlight at Titan's surface in the stratospheric haze. The approach which we will take is to first determine a rough map of Titan's surface albedo at 2.0 μm by combining the 16 Palomar images. Using this surface map and the mean haze opacity structure determined in Ch. 3, we compute model images of Titan and solve for the PSF which best describes the transformation between modeled and observed images. Subtracting psf-convolved model images from those observed, we can accurately measure the position and flux of the transient clouds.

We compute a map of Titan's relative 2.0 μm surface albedo using a technique similar to that described in Ch. 2 for the analysis of 940-nm images. The first step is to correct the K$'$ images for the light scattered off stratospheric haze. This is done in an *ad hoc* fashion by subtracting a scaled Brackett-γ (Brγ, 2.16–2.18 μm) filtered image, taken on 23 September 2002. The brightness of the eastern and western limbs is strongly asymmetric in this haze-only image, due to the $6\overset{\circ}{.}4$ phase angle of Titan at the time of the observations. We radially averaged this image, then subtracted an appropriate linear combination of the radial average and the actual Brγ image (or its mirror-image) to match the observed limb asymmetry of the K$'$ images. The difference images record only sunlight scattered below the altitude at which $\tau_{\mathrm{CH_4}} \approx 1$ for the Brγ filter, approximately 50 km (Roe *et al.*, 2002).

Using a modification of the technique of Smith *et al.* (1996), we solve for the relative albedo at each location on a latitude-longitude grid, while simultaneously determining a relative photometric scaling factor for each haze-subtracted image. We model the recorded radiance $I_{i,j}$ at each location i on Titan's surface in haze-subtracted image j in terms of the albedo A_i at zero phase, a photometric scaling factor α_j, and a simple Minnaert-type phase function with exponent k, as

$$\alpha_j I_{i,j} = A_i(\mu_{ij}\mu_{0,ij})^k, \tag{6.1}$$

where μ is the cosine of the observer's zenith angle, and μ_0 is the cosine of the solar zenith angle. We find that $k = 1$ adequately describes the phase behavior of Titan's surface in these haze-subtracted images. For Gaussian-distributed uncertainties in the measured radiances σ_{ij}, the best estimate of the surface albedo A_i at each location will be that which

minimizes the χ^2 function

$$(\chi^2)_i = \sum_j \frac{(A_i \mu_{ij} \mu_{0,ij} - \alpha_j I_{ij})^2}{(\alpha_j \sigma_{ij})^2}. \tag{6.2}$$

Solving for A_i at the minimum, we find that

$$A_i = \frac{\sum_j \frac{I_{ij} \mu_{ij} \mu_{0,ij}}{\alpha_j \sigma_{ij}^2}}{2 \sum_j \frac{\mu_{ij}^2 \mu_{0,ij}^2}{\alpha_j^2 \sigma_{ij}^2}}, \tag{6.3}$$

where the sums are taken only over the images in which the location i is viewed at less than a maximum emission angle of 65°. For any set of photometric scaling factors α_j, the optimal distribution of surface albedo A_i can be directly calculated with Eq. 6.3.

However, both the absolute and relative photometric calibration of the Palomar images are unknown *a priori*. Though we cannot determine the true surface albedo distribution from these data alone, we can use the above model to solve for a map of the relative surface albedo A'_i, while simultaneously determining the relative photometric calibration of the images α'_j. We used the Levenberg-Marquardt algorithm (Moré *et al.*, 1980) implemented in IDL by Markwardt (2003) to numerically optimize the 16 photometric scaling factors α'_j by minimizing the χ^2 function

$$\chi^2 = \sum_i \sum_j \frac{(A'_i \mu_{ij} \mu_{0,ij} - \alpha'_j I_{ij})^2}{(\alpha'_j \sigma_{ij})^2}, \tag{6.4}$$

where the sum over j is again taken over the images which view each location i, and the relative albedo map A'_i is recalculated at each iteration using Eq. 6.3.

In an important final step, we normalize the relative surface albedo map A'_j to the 2.0 μm albedo values determined for selected regions of Titan's surface (with lower spatial resolution) by fitting a radiative transfer model to resolved spectra of Titan (Ch. 3). The mean surface albedo of the central region of Titan's sub-earth hemisphere on 26 September 1999 (central longitude 57.4°W, emission angle $< 65°$) was found to be $A_{\rm mean} = 0.09$, with a range from 0.05 ± 0.01 to 0.14 ± 0.02. The calibrated surface albedo map is displayed in Fig. 6.5.

It was necessary to correct this surface map for the continual presence of clouds south of 60°S before using it to generated model images of a cloud-free Titan. This was done

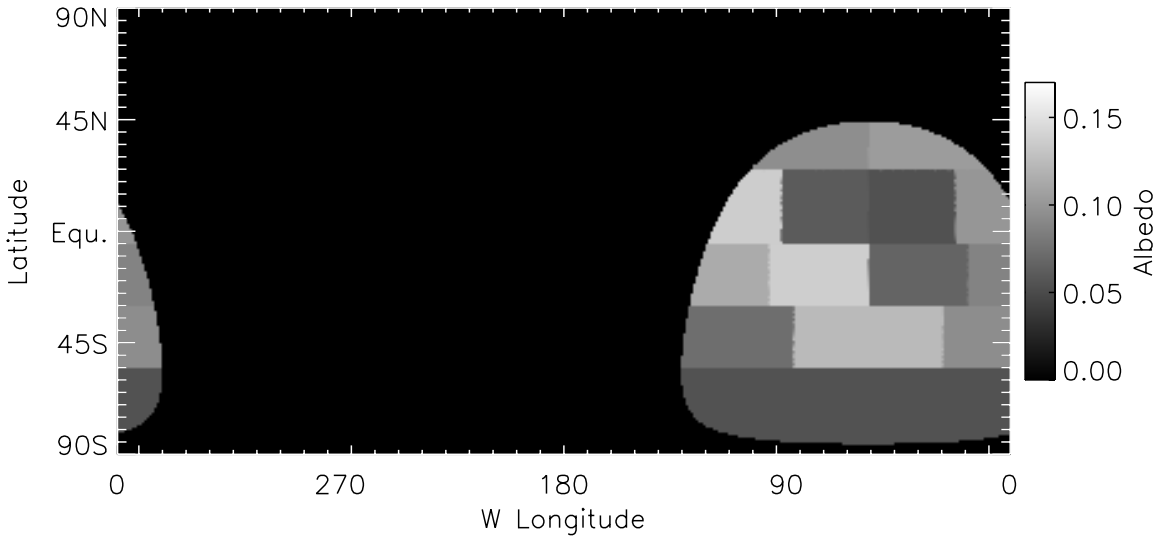

Figure 6.4: Crude map of Titan's surface albedo at 2.0μm, derived by fitting a radiative transfer model to resolved 2.0–2.3 μm spectra of Titan taken on 26 September 1999 (Ch. 3, see Fig. 3.8). Only those locations viewed at an incidence angle of $< 65°$ are mapped.

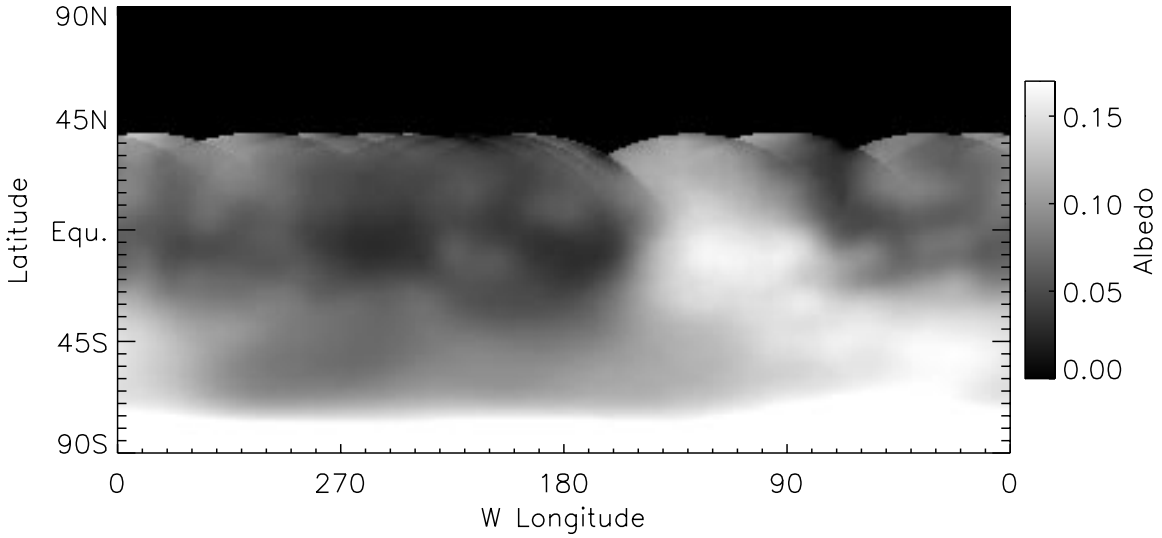

Figure 6.5: High resolution map of Titan's surface albedo at 2.0 μm, uncorrected for tropospheric clouds at the south pole. A relative albedo map calculated from 16 Palomar AO haze-corrected K$'$ images was normalized to spectrally-derived albedos (Fig. 6.4) north of 55°S. The highest and lowest albedos detected north of the polar clouds are 0.17 at (115°W, 13°S) and 0.03 at (259°W, 5°S). The region north of 40°N was not observed.

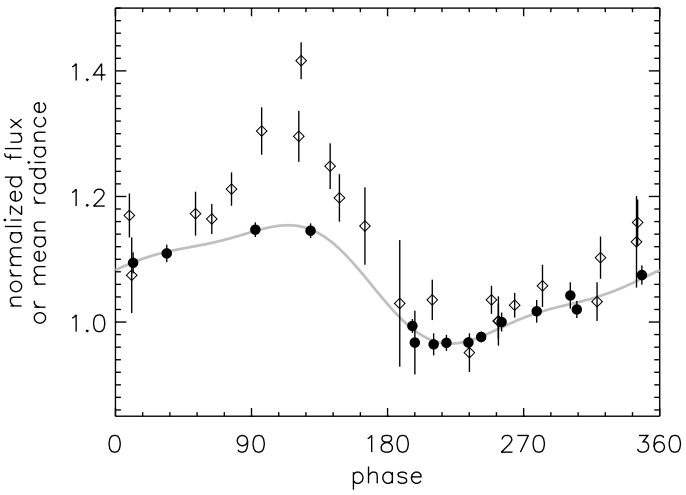

Figure 6.6: Titan's rotational lightcurve. The integrated flux in 16 Palomar K′ images, corrected for the changing distance between Titan and the Earth and Sun, is displayed with black dots, with 1-σ error bars. A 3rd-order Fourier series fit to these data is shown by a gray line. A compilation of K′ photometric observations made over the period 1989–1995 is shown in diamonds, reproduced from Griffith *et al.* (1998). The amplitude of Titan's lightcurve has decreased as our view has become dominated by Titan's south polar region. The photometric effect of Titan's daily transient clouds is insignificant at this scale.

simply by asserting that the surface albedo everywhere south of 60°S is equal to 0.07, the median value over the region 60°S–40°N. Similarly, the region north of 40°N, which was never sampled in Palomar images at an incidence angle of less than 65°, is also assumed to have an albedo of 0.07.

6.3.2 Titan's lightcurve

Though the photometric calibration of the Titan images was initially unknown, the mapping procedure described in the preceding section allows us to determined the relative scaling factors α'_j to 1–2% by matching the observed radiance of surface features. Multiplying each of the 16 Palomar K′ images by this scaling factor, we integrate the light recorded in each image and correct for the changing heliocentric and geocentric distances to recover Titan's rotational lightcurve. This lightcurve is displayed in Fig. 6.6. Following the convention of Lemmon *et al.* (1995), we have normalized the lightcurve to the measurement nearest orbital longitude 253°.

In Section 6.3.4, we determine the flux of each cloud identified in Palomar and Keck images, with respect to Titan's total flux in the images. To then normalize these measure-

ments made at different orbital phases, we divide by a model of Titan's lightcurve, shown as a gray line in Fig. 6.6. This 3rd-order Fourier series is not meant to represent a physical model, but is simply a tool for interpolating between lightcurve points unevenly spaced in orbital longitude.

6.3.3 PSF determination

To assist in identifying transient clouds, we next generated simulated cloud-free images of Titan matching the orientation, platescale, and filter of each set of observations. This was done using the radiative transfer model of Griffith *et al.* (1991), with the simplifying assumption that the distribution of haze in Titan's atmosphere at every latitude is sufficiently well described by the mean atmosphere observed on 20 December 2001 (see Section 3.5.1 and Fig. 3.4). While this is not unreasonable for the majority of the images treated here, taken in 2002, it is not a good approximation for the speckle images taken in 1996–1997. This simplification, however, allowed us to compute a single multi-dimensional grid of 2.00–2.30 μm model spectra, with a range of underlying surface albedos (0–0.50 every 0.02), incidence angles (0°–85° every 1°), and emission angles (0°–85° every 1°), which we then interpolated to predict the spectrum recorded by each pixel of each image. The spectral images thus produced were finally multiplied by the transmission function of the K′ filter used and integrated over wavelength.

Having computed 24 model images with resolution effectively equal to the platescale (with the exception of the surface features, whose resolution is set by the Palomar images out of which the surface map was created), we then determined the PSF which best describes the convolution from model to observed images. We construct the PSF from the sum of either 2 Gaussian functions (for the speckle images) or an Airy pattern and 2 Gaussian functions, the narrowest of which is constrained to have a width equal to the diffraction limit of the telescope. The width of the remaining two Gaussian functions and the ratio of their contributions were allowed to freely vary, as was the position of the model image on the detector. We again used the Levenberg-Marquardt algorithm to optimize these 6 parameters, minimizing the squared difference between the PSF-convolved synthesized images, and the observed images. The resulting PSFs are displayed in the fourth column of Figs. 6.7–6.10.

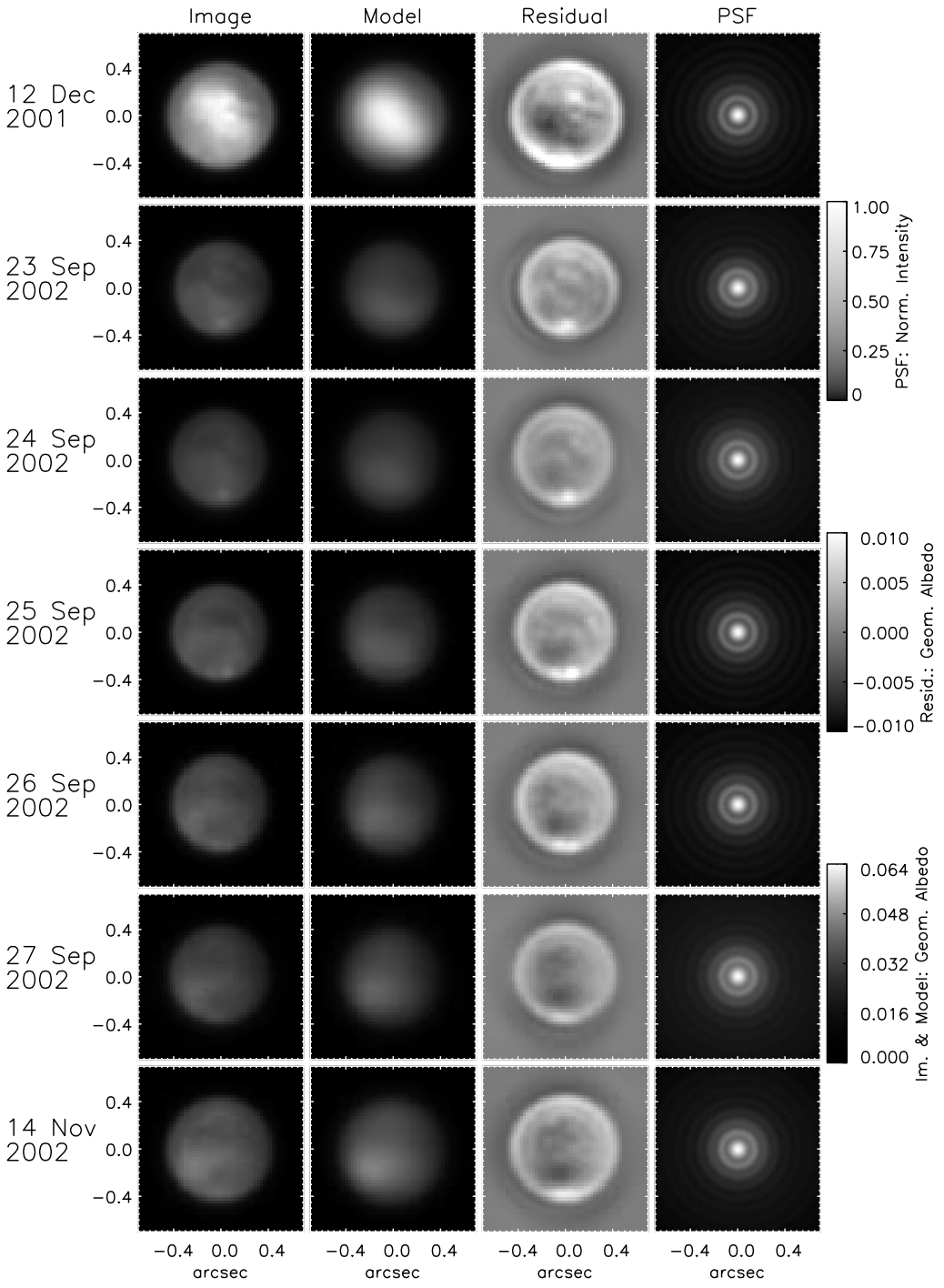

Figure 6.7: Palomar AO images, image models, and residuals. I. *left:* Palomar images, displayed on and absolute geometric albedo scale (lower gray-scale). *left-center:* Model images, displayed on identical gray-scale. *right-center:* Residual, which highlights the transient tropospheric clouds which are nearly always present near Titan's south pole (middle gray-scale). *right:* Optimized PSF (upper gray-scale).

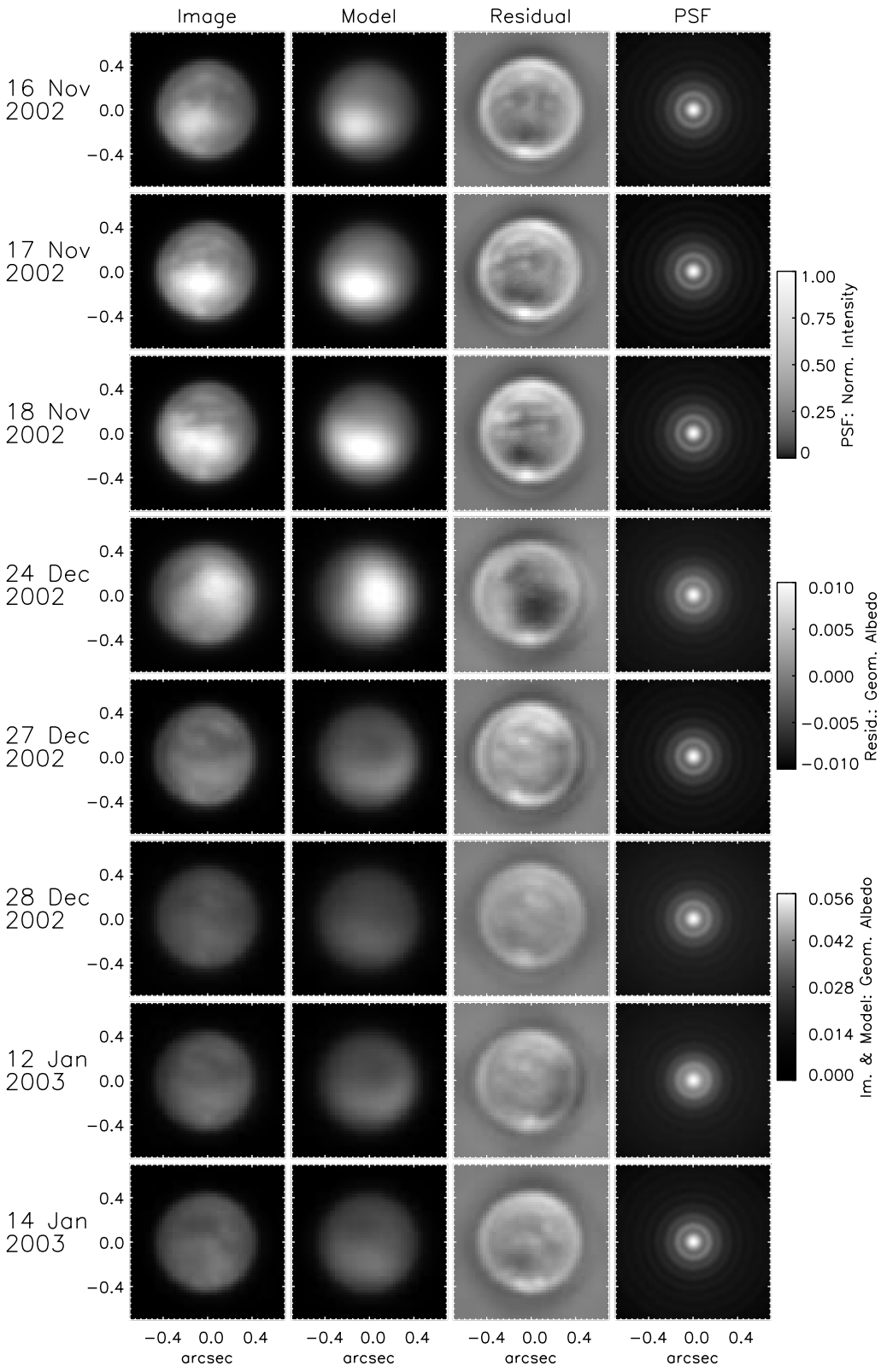

Figure 6.8: Palomar AO images, image models, and residuals. II.

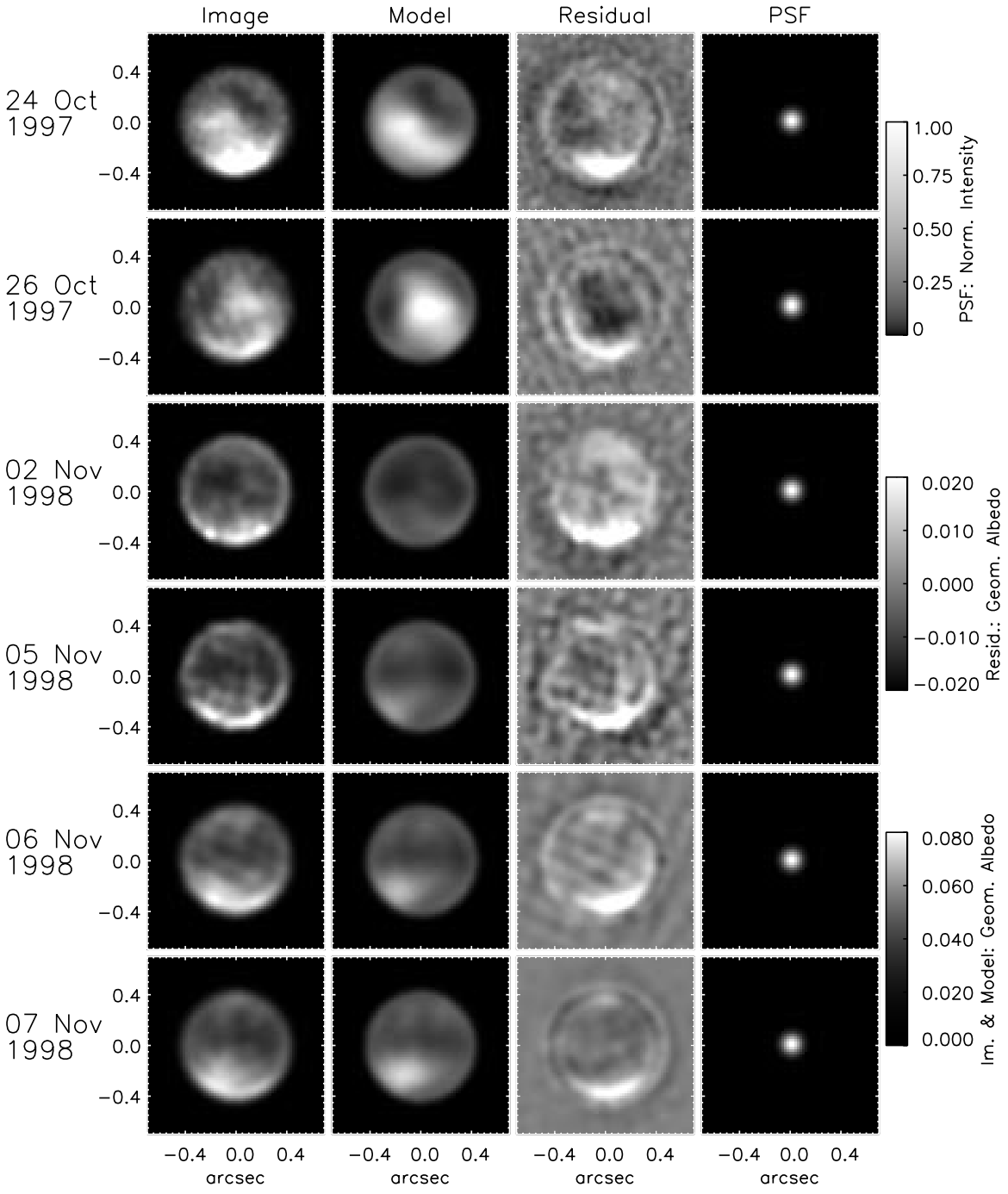

Figure 6.9: Keck speckle images, image models, and residuals. Note the strong, non-Gaussian noise, which renders interpretation of these images difficult.

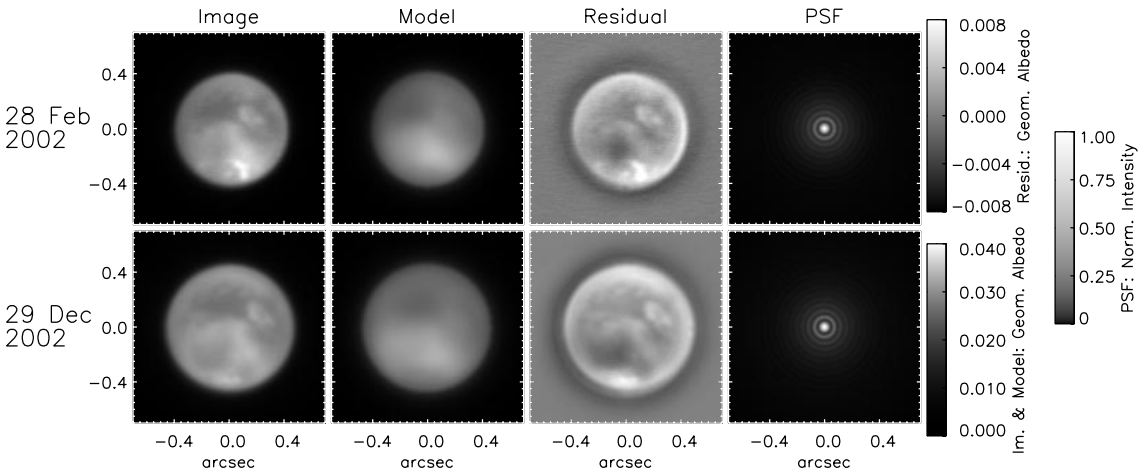

Figure 6.10: Keck AO images, image models, and residuals. The high resolution achieved by these images, with respect to the surface albedo map used to generate the model images, causes strong residuals to surround high contrast surface features.

6.3.4 Cloud positions and fluxes

The residual of each image, minus the model image, was finally searched for transient cloud-like features. 27 candidates were found, and their locations and fluxes with respect to that of Titan's disk are listed in Table 6.4, determined by fitting a scaled PSF to the residual image. The locations of those clouds identified with high confidence are also displayed graphically in Fig. 6.11. Position and relative flux uncertainties were determined by Monte Carlo simulation, by adding 20 realizations of Gaussian noise at the measured 1-σ level, and recomputing the location and flux of the apparent cloud in each. Systematic uncertainties in the PSF are not included, and could lead to systematic errors of up to a factor of 2 in the derived fluxes. We finally multiply the flux of each cloud relative to that of the disk by the the normalized lightcurve value at that orbital longitude (see Fig. 6.6). This corrected flux is therefore that of the cloud, relative to the total flux of Titan's disk at 253°W longitude.

6.4 Discussion

6.4.1 Cloud location

Four features were identified in the Keck speckle images which might be transient clouds. They are all unresolved, $\sim 2\sigma$ brighter than the surrounding regions, and clearly transient,

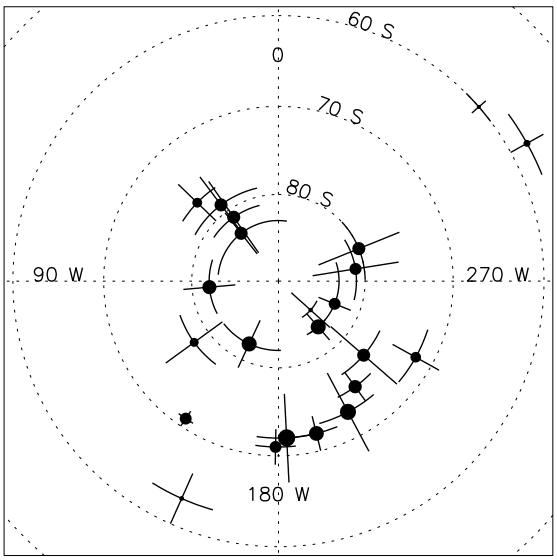

Figure 6.11: Polar stereographic projection of the locations of the transient clouds detected. Their relative flux is indicated by the area of the filled circles, and 1-σ uncertainties in the positions are shown with error bars.

as no feature is visible in subsequent images of the same location. However, given the non-Gaussian nature of the noise in speckle reconstructions, it is difficult to have much confidence in these detections. We note, however, that they occur at more northerly latitudes than the clouds detected several years later in AO images. We have searched for clouds at these locations in HST/NICMOS images taken within one month of the October 1997 Keck observations, but their lower spatial resolution rendered them insensitive to features of this scale.

In contrast to the speckle images in 1997–1998 and even Palomar image taken in 1999-2000 (Ch. 3), distinct unresolved clouds are clearly visible on 13 of 16 nights in Palomar images of Titan taken between 20 December 2001 and 14 January 2003. Even the 3 nights on which the achieved resolution was insufficient to resolve individual clouds showed a regional brightening at the location of previous clouds. It therefore appears that the clouds were continually present pole-ward of 70°S during the period of September 2002 to January 2003. Occasional clouds were also detected at lower latitudes, the furthest north being located at 58°S ±2° on 14 January 2003.

6.4.2 Cloud size

Individual unresolved clouds observed with the Palomar AO system contribute between 0.09% and 1.1% of Titan's flux at 2.0 μm. This corresponds to the brightness expected for

Table 6.4: Position and flux of detected transient clouds

Date	Flux[a]	Corrected Flux[b]	Longitude	Latitude	Comments
24 Oct 1997	0.0025 ± 0.0006	0.0029 ± 0.0007	88 ± 8	-44 ± 7	low confidence
24 Oct 1997	0.0018 ± 0.0006	0.0020 ± 0.0007	62 ± 7	-38 ± 6	low confidence
02 Nov 1998	0.0040 ± 0.0007	0.0041 ± 0.0007	289 ± 13	-58 ± 6	low confidence
02 Nov 1998	0.0026 ± 0.0007	0.0027 ± 0.0007	170 ± 13	-55 ± 6	low confidence
20 Dec 2001	0.0034 ± 0.0005	0.0038 ± 0.0006	46 ± 12	-77 ± 3	
20 Dec 2001	0.0028 ± 0.0005	0.0032 ± 0.0006	126 ± 17	-78 ± 4	
20 Dec 2001	0.0008 ± 0.0005	0.0009 ± 0.0005	156 ± 8	-63 ± 3	
28 Feb 2002	0.0050 ± 0.0010	0.0056 ± 0.0011	146 ± 3	-71 ± 1	cloud resolved
28 Feb 2002	0.0007 ± 0.0001	0.0007 ± 0.0001	228 ± 15	-85 ± 3	
28 Feb 2002	0.0006 ± 0.0001	0.0006 ± 0.0001	311 ± 4	-60 ± 1	
23 Sep 2002	0.0103 ± 0.0008	0.0105 ± 0.0008	183 ± 11	-72 ± 5	
24 Sep 2002	0.0091 ± 0.0008	0.0089 ± 0.0008	208 ± 12	-73 ± 5	
25 Sep 2002	0.0077 ± 0.0008	0.0077 ± 0.0008	194 ± 8	-72 ± 2	
25 Sep 2002	0.0051 ± 0.0008	0.0052 ± 0.0008	279 ± 23	-81 ± 5	
26 Sep 2002	0.0062 ± 0.0007	0.0060 ± 0.0007	216 ± 9	-75 ± 2	
26 Sep 2002	0.0060 ± 0.0007	0.0062 ± 0.0007	292 ± 21	-80 ± 5	
27 Sep 2002	0.0110 ± 0.0020	0.0110 ± 0.0020	-	-	region unresolved
14 Nov 2002	0.0130 ± 0.0020	0.0130 ± 0.0020	-	-	region unresolved
16 Nov 2002	0.0060 ± 0.0010	0.0067 ± 0.0011	38 ± 46	-83 ± 3	
17 Nov 2002	0.0060 ± 0.0010	0.0067 ± 0.0011	37 ± 24	-79 ± 4	
18 Nov 2002	0.0060 ± 0.0010	0.0067 ± 0.0011	35 ± 21	-81 ± 5	
24 Dec 2002	0.0070 ± 0.0020	0.0080 ± 0.0023	95 ± 23	-82 ± 3	
27 Dec 2002	0.0040 ± 0.0010	0.0039 ± 0.0010	241 ± 11	-72 ± 3	
28 Dec 2002	0.0060 ± 0.0010	0.0058 ± 0.0010	229 ± 15	-77 ± 5	
29 Dec 2002	0.0080 ± 0.0010	0.0077 ± 0.0010	221 ± 10	-83 ± 2	cloud resolved
12 Jan 2003	0.0080 ± 0.0010	0.0088 ± 0.0011	155 ± 27	-82 ± 3	
14 Jan 2003	0.0050 ± 0.0010	0.0052 ± 0.0010	179 ± 7	-71 ± 2	
14 Jan 2003	0.0050 ± 0.0010	0.0049 ± 0.0010	248 ± 40	-83 ± 2	
14 Jan 2003	0.0017 ± 0.0006	0.0018 ± 0.0006	299 ± 7	-58 ± 2	

a. Flux of cloud, divided by total disk flux.
b. As *a.*, but normalized to total disk flux at orbital longitude 253°.

optically thick, foreshortened clouds with diameters between 100 and 400 km (see Ch. 5 for details), consistent with the telescope's projected diffraction limit of 500×1000 km. However, on both nights of Keck AO observations, clouds were detected which were clearly spatially resolved with linear dimensions of 1000–1400 km, yet equivalent in brightness to an optically thick cloud of only 250–300 km diameter. This implies a low filling factor of $\sim 5\%$ within the resolved region, if the constituent clouds are optically thick. This conclusion is likely to apply to the apparently unresolved clouds as well, whose brightness is consistent with filling factors of 5–20%.

Integrating the light of all clouds identified each night, the corresponding areal coverage of optically thick clouds over Titan's visible disk varied from 0.2% on 27 December 2002 to 0.7% on 14 November 2002. These figures are similar to those derived by Griffith *et al.*

(2000) for the areal coverage of the clouds responsible for Titan's daily spectral variations at 2.12–2.16 μm. No clouds were detected which rival the 7% coverage event observed spectroscopically on 5 September 1995.

No variation in the flux of clouds was detected which could not be attributed to the fading due to their reduced projected area as they approach Titan's limb. Such fading due to reduced projected area is clearly seen in the cloud near 200°W, 72°S which persisted for 4 nights, gradually decreasing in flux by 40%. We therefore see no evidence of rapid cloud formation or dissipation as observed in more sensitive Keck AO observations by Roe *et al.* (2002).

6.4.3 Seasonal evolution

The relative faintness of the clouds imaged on 28 February 2002, compared to those observed subsequently with the Palomar telescope, is a surprising result. At the time this image was taken, in response to a transient brightening of Titan at 750 nm (Ch. 7), we believed it to represent an unusually bright storm. The previous 8 nights of Keck and Gemini telescope observations which led to the discovery of their location at Titan's south pole (Brown *et al.*, 2002; Roe *et al.*, 2002) had all recorded fainter, unresolved clouds. Yet this apparently bright "outburst", as we called it, was quite modest compared to the majority of nights in 2002–2003. The tentative conclusion which we draw from this is that the typical size, or optical thickness of the clouds at Titan's south pole has been increasing since their discovery in December 2000.

The gradual brightening of the clouds at Titan's south pole is consistent with our current understanding of their formation mechanism (Ch. 5). Titan's tropospheric clouds currently reside at the location of maximum insolation on the satellite (Fig. 6.12). This, along with their altitude near that expected for convective clouds initiated near Titan's surface, suggests that heating of the surface or lower troposphere by sunlight is the trigger which initiates moist convection (Brown *et al.*, 2002). The insolation at Titan's south pole reached a maximum at the time of summer solstice, in late October 2002. It therefore seems likely that cloud formation would be more vigorous up to this date, and possibly continue to increase for some time after if the heat capacity of Titan's surface and lower troposphere plays a significant moderating role.

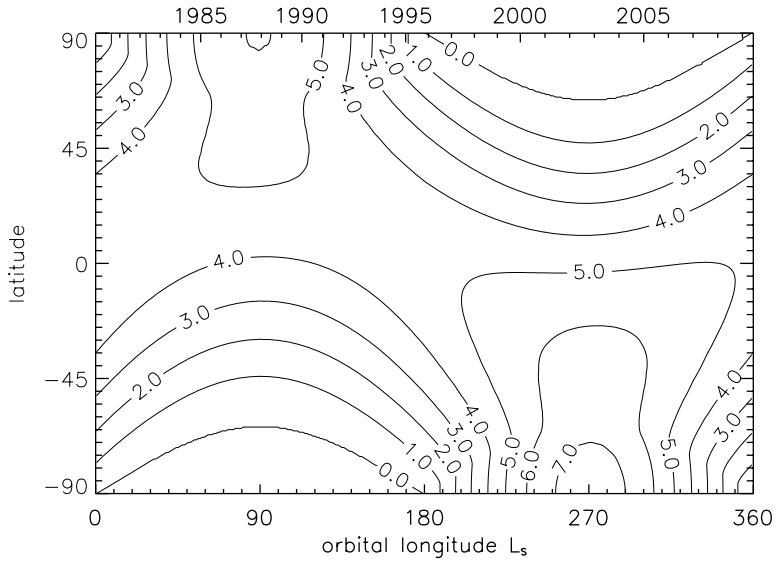

Figure 6.12: The average daily insolation on Titan, as a function of latitude and season, in Watts m^{-1}. Titan's south pole is currently experiencing the strongest insolation of any location on the satellite, significantly stronger than the equator at solstice.

6.4.4 Tropospheric wind

Tracking the motion of tropospheric clouds is one of the few available methods for measuring the tropospheric winds on Titan. The longevity of the clouds which we have detected (3 persist for at least 3 nights) suggests this might be possible. The brightest single cloud detected, which persisted for 4 nights from 23 to 26 September 2002, did appear to move westward $33° \pm 14°$ over 72 hr (equivalent to a speed of 1.7 ± 0.7 m s^{-1}) while remaining at a constant latitude of 73°S±2°. However, the two other clouds observable over more than 2 nights (16–18 November and 27–29 December 2002) both remained stationary to within the positional uncertainties, giving little confidence in this single measurement. Nevertheless, a robust 3-σ upper limit of 3.5 m s^{-1} can be placed on the wind speed at 72°S–83°S, the location of these three clouds. The altitude to which this upper limit applies is assumed to be 16 ± 5 km, the altitude of the cloud tops determined in Ch. 5. This upper limit is consistent with the low tropospheric winds predicted by general circulation models of Titan's atmosphere (Hourdin *et al.*, 1995; Tokano *et al.*, 2001).

The fact that no clouds are observed to dissipate suggests that it might be possible to track clouds over periods greater than one Titan day (15.9 terrestrial days). Figure. 6.13

illustrates the difficulty. Though no cloud is observed to dissipate on Titan's sunlit side, the pattern of clouds which reappears following one full rotation bears little resemblance to that present 16 days earlier.

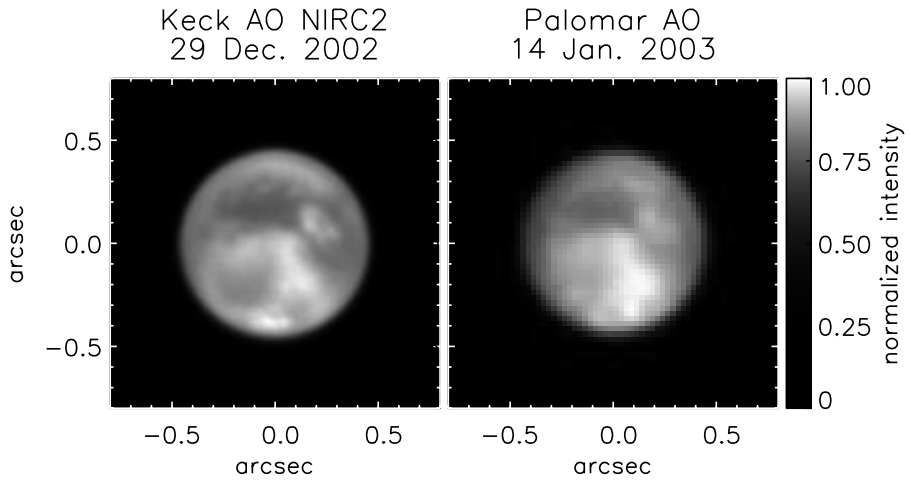

Figure 6.13: Images of Titan separated by one rotation. *left:* Keck AO image on 29 December 2002. *right:* Palomar AO image on 14 January 2003. Significant changes in the cloud distribution have occurred

6.5 Conclusions

The 24-night study presented in this chapter provides the first long-term look at the tropospheric clouds recently discovered near Titan's south pole. Though the presence of clouds in 1997–1998 Keck speckle images is uncertain, AO images acquired with both the Palomar 5-m and Keck-II 10-m telescopes since December 2001 reveal the continuous presence of transient clouds at 70°S-80°. What appear in AO images to be isolated clouds with typical linear scales of < 1000 km may in fact represent regions of scattered cloudiness whose filling factor is 5–20%, or isolated 100–400 km diameter storms. In either case, the clouds account for 0.5–1% of Titan's 2.0 μm flux, consistent with a global cloud cover fraction of 0.2–0.7%.

The location of the clouds, and their apparent increase in area or optical depth over the period from December 2001 to January 2003 is consistent with the hypothesis that their formation controlled by the insolation of Titan's surface (Ch. 5). Regions of cloud cover were observed to persist the length of each observing run (up to 72 hr), rotating over the limb before any change in their areal cover could be detected. They also remained

nearly stationary with respect to Titan's surface, moving at an average speed of less than 3.5 m s^{-1}. Yet sufficient changes take place over one full rotation of Titan to render the cloud distribution unrecognizable.

These observations provide many clues to the true nature of Titan's south polar clouds, but it remains difficult to piece together a single most plausible physical model. If these features represent isolated hurricane-like storms, then these may persist for several Titan days, drifting slowly with the wind at a speed lower than the upper limit derived here. Alternately, the observed clouds could be short-lived regions of scattered cumulus-type convective cells which remain fixed over surface regions rich in CH_4, with different regions active at various times. Continued high resolution monitoring observations of Titan may allow us to distinguish between these possibilities, and to observe the expected decrease in polar cloud activity as Titan's long southern summer draws to an end in August 2009.

Chapter 7

A photometric search for clouds on Titan

7.1 Introduction

Variations in Titan's flux as a function of orbital phase provided the first reliable evidence of a heterogeneous surface in synchronous rotation with Titan's 15.9 day orbit. Titan's rotational lightcurve is only expressed at wavelengths of low methane opacity (spectral windows to the surface), while the flux in the methane bands, due only to sunlight scattered by the stratospheric haze, remains unchanging on this timescale. By dividing the measured flux in a window region by that in a nearby methane band, lightcurves at 1.1, 1.3, 1.6, and 2.0 μm have been derived (Lemmon *et al.*, 1993; Griffith, 1993; Coustenis *et al.*, 1995). Correcting for systematic offsets in the geometric albedo reported by various observers, Lemmon *et al.* (1995) found that Titan's lightcurve repeats from one rotation to the next, to the 5% precision of the data then available. More precise spectral observations have since uncovered transient methane clouds in Titan's troposphere, which superimpose daily $\sim 3\%$ (at 2 μm), and occasionally larger, variations on the rotational lightcurve (Griffith *et al.*, 1998, 2000).

High resolution imaging studies of Titan in the visible (Smith *et al.*, 1996; Richardson *et al.*, 2001; Bouchez *et al.*, 2003) and near-infrared (Combes *et al.*, 1997; Gibbard *et al.*, 1999; Meier *et al.*, 2000; Coustenis *et al.*, 2001) revealed the surface albedo features which give rise to Titan's repeating lightcurve, but long failed to conclusively detect clouds. Recent adaptive optics observations with the Keck and Gemini telescopes, performed soon after the observations described in this chapter were begun, have located Titan's daily clouds

near the south pole (Brown *et al.*, 2002; Roe *et al.*, 2002). Individual storms were observed to persist at least 24 hours in one case (Brown *et al.*, 2002), and vary in flux by 50% over 3 hr in another (Roe *et al.*, 2002), but little other information on their lifetimes, formation frequency, and size spectrum can be gleaned from these few observations (a total of 10 nights.)

Frequent observations over many rotations, either resolved imaging or photometric monitoring, provide the only means of constraining many of these basic properties of Titan's transient clouds. We began nightly photometry of Titan on 5 December 2001, using a 14-inch telescope on the Caltech campus to measure the relative albedo of Titan's lower atmosphere and surface at 750 and 825 nm. Ideally, such a study would be performed in the near-infrared (e.g., the 1.6 or 2.0 μm spectral windows), where the low optical depth of stratospheric haze maximizes the amplitude of Titan's rotational lightcurve (Lemmon *et al.*, 1995), and the photometric effect of any transient clouds. However, available equipment limited us to wavelengths shorter than 1 μm, while variable atmospheric water absorptions ruled out the 950 nm transmission window. The optical depth of Titan's stratospheric haze may be as high as $\tau = 6$ at 750 nm (Rannou *et al.*, 1995), but the high single-scattering albedo of the aerosols (McKay *et al.*, 2001) allows Titan's surface to be detected nevertheless, albeit with low contrast (Smith *et al.*, 1996; Richardson *et al.*, 2001).

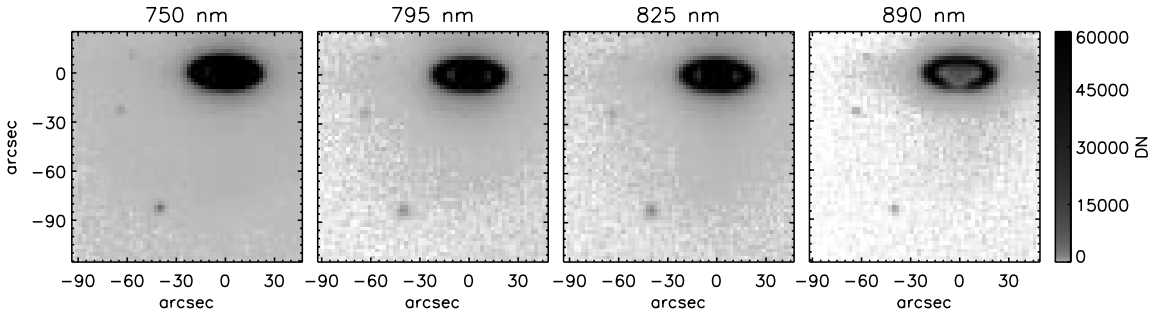

Figure 7.1: A series of 4 consecutive images of Titan taken on 02 February 2002, between 03:57:55 and 03:58:27 UT. Titan is the brightest of the 4 visible satellites, 90″ south-east of Saturn. Raw 5 s integrations have been corrected for detector bias and pixel gain variations. A logarithmic gray-scale highlights the scattered light from Saturn, brightest in the shorter wavelength filters.

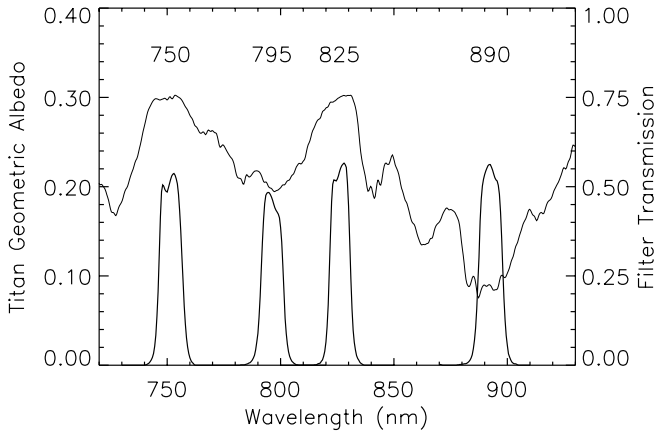

Figure 7.2: Transmission spectra of filters used on the 14-inch telescopes, superimposed on a spectrum of Titan from Karkoschka (1998). Titan is bright where CH_4 opacity is low, and dark in the CH_4 bands at 795 and 890 nm.

7.2 Observations

Photometric observations of Titan were acquired on 81 nights between 5 December 2001 to 12 April 2002, using the 14-inch Celestron Schmidt-Cassegrain telescope of the Robinson-Downs Rooftop Observatory. We recorded the images of Titan on a 512^2 pixel Kodak CCD detector (Santa Barbara Instruments Group camera model ST–9E), with a native platescale of $1.1''$ pix^{-1}. Between 80 and 400 images were acquired each night, with integration times of 5 s or 10 s, depending on seeing conditions and cloud opacity. Seeing was generally 4–5$''$ FWHM, and the weather conditions ranged from clear (46% of the nights) to partly cloudy. To maximize the observing efficiency, images were rebinned by a factor of 2, and only the smallest possible subarray containing both Saturn and Titan was read out, generally 96×64 binned pixels. A summary of the observations is provided in Table 7.1.

Four narrow-band filters between 750 nm and 890 nm were used to sample Titan's spectrum, two centered on CH_4 absorption bands and two centered on window regions of low CH_4 opacity (Fig. 7.2). Titan's atmosphere is opaque below $\sim$ 80 km altitude in both the 795 nm and 890 nm filters, and thus the only light detected is scattered off the stratospheric haze, which we expect to vary only on seasonal timescales. We therefore used Titan's flux in the CH_4 bands as our photometric standards, alternating images taken at window wavelengths (750 nm and 825 nm) with those taken in the CH_4 bands (795 nm and 890 nm), and dividing the consecutively measured fluxes. We typically cycled through

Table 7.1: C-14 observations. I.

Date	UT	Exp.	Lon.	Lat.	Airmass	750/795	N	825/890	N	795/890	N
05 Dec 2001	06:05–06:43	10.0	112.4	-25.6	1.10–1.05	2.496 ± 0.008	25	1.234 ± 0.004	25	4.131 ± 0.037	25
06 Dec 2001	05:48–06:18	10.0	134.7	-25.6	1.12–1.07	2.434 ± 0.033	20	1.139 ± 0.025	20	3.673 ± 0.134	20
07 Dec 2001	05:48–06:27	10.0	157.5	-25.6	1.11–1.06	2.471 ± 0.012	25	1.196 ± 0.004	25	4.031 ± 0.060	25
13 Dec 2001	04:32–04:59	10.0	292.3	-25.5	1.23–1.16	2.471 ± 0.008	20	1.200 ± 0.005	20	4.076 ± 0.036	20
14 Dec 2001	06:08–06:35	10.0	316.5	-25.5	1.05–1.03	2.105 ± 0.060	12	1.111 ± 0.030	12	3.147 ± 0.268	7
16 Dec 2001	04:48–05:14	10.0	0.4	-25.5	1.16–1.11	2.478 ± 0.017	20	1.167 ± 0.007	20	3.888 ± 0.060	20
17 Dec 2001	05:49–06:21	10.0	24.1	-25.5	1.05–1.03	2.491 ± 0.017	25	1.234 ± 0.018	25	4.158 ± 0.057	25
18 Dec 2001	05:22–05:50	10.0	46.3	-25.5	1.08–1.05	2.519 ± 0.007	20	1.257 ± 0.005	20	4.244 ± 0.035	20
19 Dec 2001	06:41–07:15	10.0	70.2	-25.5	1.03–1.04	2.505 ± 0.007	25	1.269 ± 0.004	25	4.342 ± 0.035	25
20 Dec 2001	05:48–06:16	10.0	92.0	-25.5	1.05–1.03	1.171 ± 1.448	9	0.577 ± 0.528	13	2.333 ± 2.438	12
23 Dec 2001	07:40–08:04	10.0	161.8	-25.5	1.08–1.12	2.465 ± 0.014	18	1.163 ± 0.008	18	3.972 ± 0.077	18
25 Dec 2001	05:15–05:42	10.0	204.9	-25.5	1.05–1.04	2.437 ± 0.009	20	1.186 ± 0.012	20	4.010 ± 0.048	20
04 Jan 2002	05:02–05:29	10.0	71.0	-25.5	1.04–1.03	2.476 ± 0.017	20	1.237 ± 0.007	20	4.168 ± 0.064	20
05 Jan 2002	05:05–05:34	10.0	93.8	-25.5	1.03–1.03	2.504 ± 0.016	21	1.223 ± 0.007	21	4.256 ± 0.058	21
06 Jan 2002	05:08–05:35	10.0	116.4	-25.5	1.03–1.03	2.550 ± 0.015	20	1.244 ± 0.008	20	4.241 ± 0.063	20
11 Jan 2002	04:60–05:27	10.0	229.6	-25.5	1.03–1.04	2.456 ± 0.011	20	1.209 ± 0.007	20	4.126 ± 0.047	20
13 Jan 2002	05:01–05:36	10.0	274.9	-25.5	1.03–1.05	2.433 ± 0.027	25	1.186 ± 0.018	25	3.980 ± 0.057	25
14 Jan 2002	04:43–05:10	10.0	297.2	-25.5	1.03–1.03	2.503 ± 0.011	20	1.244 ± 0.005	20	4.148 ± 0.061	20
17 Jan 2002	04:35–05:02	10.0	4.9	-25.4	1.03–1.04	2.467 ± 0.014	20	1.199 ± 0.008	20	4.206 ± 0.123	20
18 Jan 2002	02:51–05:08	10.0	26.8	-25.5	1.11–1.04	2.494 ± 0.005	100	1.229 ± 0.003	100	4.231 ± 0.025	60
19 Jan 2002	07:10–07:42	10.0	52.5	-25.5	1.28–1.42	2.519 ± 0.011	40	1.277 ± 0.005	40	0.000 ± 0.000	0
20 Jan 2002	04:48–05:13	10.0	72.9	-25.5	1.04–1.05	2.516 ± 0.007	30	1.252 ± 0.004	30	0.000 ± 0.000	0
21 Jan 2002	04:40–05:06	10.0	95.4	-25.5	1.03–1.05	2.536 ± 0.004	30	1.255 ± 0.003	30	0.000 ± 0.000	0
22 Jan 2002	04:01–05:05	10.0	117.7	-25.5	1.03–1.05	2.543 ± 0.005	60	1.254 ± 0.002	60	4.320 ± 0.022	60
23 Jan 2002	03:40–06:11	5.0	141.2	-25.5	1.04–1.16	1.996 ± 0.226	30	1.026 ± 0.136	25	2.681 ± 0.809	5
24 Jan 2002	04:45–05:29	10.0	163.5	-25.5	1.04–1.09	2.425 ± 0.010	40	1.246 ± 0.005	40	4.176 ± 0.041	40
25 Jan 2002	04:35–05:31	10.0	186.0	-25.5	1.04–1.09	2.506 ± 0.010	50	1.258 ± 0.005	50	4.116 ± 0.030	50
26 Jan 2002	02:20–03:21	5.0	206.6	-25.5	1.11–1.04	2.475 ± 0.010	45	1.230 ± 0.006	45	4.090 ± 0.064	45
30 Jan 2002	04:29–05:13	10.0	298.9	-25.5	1.05–1.10	2.553 ± 0.010	40	1.259 ± 0.006	40	4.181 ± 0.049	40
31 Jan 2002	03:37–04:25	10.0	320.6	-25.5	1.03–1.05	2.481 ± 0.007	40	1.240 ± 0.004	40	4.088 ± 0.036	40

Table 7.1: C-14 observations. II.

Date	UT	Exp.	Lon.	Lat.	Airmass	750/795	N	825/890	N	795/890	N
01 Feb 2002	04:22–05:06	10.0	343.9	-25.5	1.05–1.10	2.464 ± 0.009	39	1.216 ± 0.003	39	4.159 ± 0.030	39
02 Feb 2002	03:57–04:40	5.0	6.1	-25.5	1.04–1.07	2.484 ± 0.007	60	1.244 ± 0.004	60	4.316 ± 0.035	60
03 Feb 2002	02:53–03:47	10.0	27.7	-25.5	1.04–1.03	2.515 ± 0.006	50	1.268 ± 0.003	50	4.320 ± 0.027	50
04 Feb 2002	05:00–05:53	10.0	52.3	-25.5	1.11–1.24	2.553 ± 0.006	50	1.273 ± 0.004	50	4.370 ± 0.027	50
06 Feb 2002	02:21–03:23	10.0	95.0	-25.5	1.05–1.03	2.505 ± 0.005	55	1.277 ± 0.003	55	4.300 ± 0.025	55
07 Feb 2002	02:05–02:58	10.0	117.3	-25.5	1.06–1.03	2.504 ± 0.005	50	1.275 ± 0.003	50	4.236 ± 0.026	50
08 Feb 2002	02:24–03:06	10.0	140.1	-25.5	1.04–1.03	2.484 ± 0.008	40	1.228 ± 0.004	40	4.237 ± 0.035	40
09 Feb 2002	02:38–03:20	10.0	162.9	-25.5	1.04–1.03	2.454 ± 0.009	40	1.169 ± 0.005	40	3.944 ± 0.045	40
10 Feb 2002	02:38–03:22	10.0	185.5	-25.5	1.03–1.03	2.520 ± 0.009	41	1.268 ± 0.005	41	4.075 ± 0.043	41
11 Feb 2002	02:08–03:12	10.0	207.8	-25.5	1.05–1.03	2.464 ± 0.006	60	1.235 ± 0.003	60	4.129 ± 0.025	60
12 Feb 2002	02:26–03:47	5.0	230.8	-25.5	1.04–1.06	2.427 ± 0.030	58	1.200 ± 0.013	58	3.815 ± 0.109	58
13 Feb 2002	02:35–03:17	10.0	253.2	-25.5	1.03–1.04	2.261 ± 0.036	40	1.188 ± 0.017	40	3.059 ± 0.144	40
15 Feb 2002	03:11–03:48	5.0	298.8	-25.5	1.04–1.07	2.528 ± 0.032	50	1.168 ± 0.014	50	3.725 ± 0.102	50
16 Feb 2002	03:12–03:48	5.0	321.4	-25.5	1.04–1.07	2.492 ± 0.012	50	1.191 ± 0.008	50	4.037 ± 0.049	50
18 Feb 2002	02:04–02:43	5.0	5.3	-25.5	1.03–1.03	1.570 ± 0.308	40	1.203 ± 0.063	36	3.119 ± 0.463	30
19 Feb 2002	02:50–03:27	5.0	28.6	-25.5	1.04–1.06	2.500 ± 0.010	49	1.225 ± 0.008	50	4.124 ± 0.065	50
20 Feb 2002	02:47–03:21	5.0	51.1	-25.6	1.04–1.06	2.539 ± 0.036	50	1.189 ± 0.020	50	3.904 ± 0.119	42
22 Feb 2002	02:26–03:19	10.0	96.0	-25.6	1.03–1.07	2.559 ± 0.006	50	1.225 ± 0.003	50	4.305 ± 0.028	50
23 Feb 2002	02:11–03:48	10.0	118.7	-25.6	1.03–1.11	2.554 ± 0.008	90	1.277 ± 0.004	90	4.281 ± 0.032	90
24 Feb 2002	02:08–03:11	10.0	140.9	-25.6	1.03–1.07	2.497 ± 0.007	60	1.207 ± 0.004	60	4.091 ± 0.031	60
25 Feb 2002	02:32–03:19	10.0	163.7	-25.6	1.04–1.08	2.532 ± 0.013	40	1.236 ± 0.005	40	4.001 ± 0.037	40
26 Feb 2002	02:08–03:20	5.0	186.1	-25.6	1.03–1.09	2.483 ± 0.009	100	1.204 ± 0.005	100	3.971 ± 0.032	100
28 Feb 2002	02:12–03:05	10.0	231.1	-25.6	1.03–1.08	2.526 ± 0.007	50	1.210 ± 0.004	50	4.086 ± 0.035	50
02 Mar 2002	02:12–03:33	10.0	276.4	-25.6	1.04–1.14	2.512 ± 0.008	75	1.199 ± 0.004	75	4.052 ± 0.031	75
03 Mar 2002	02:38–03:48	10.0	299.3	-25.6	1.06–1.18	2.513 ± 0.006	60	1.248 ± 0.004	60	4.155 ± 0.032	60
04 Mar 2002	02:16–03:09	10.0	321.3	-25.6	1.04–1.10	2.515 ± 0.007	50	1.263 ± 0.004	50	4.192 ± 0.031	50
05 Mar 2002	02:17–03:17	10.0	343.9	-25.7	1.05–1.13	2.505 ± 0.006	57	1.233 ± 0.003	57	4.178 ± 0.023	57
06 Mar 2002	02:44–03:56	5.0	6.9	-25.7	1.08–1.23	2.494 ± 0.011	100	1.189 ± 0.005	100	4.038 ± 0.047	100
11 Mar 2002	02:41–03:48	10.0	119.4	-25.7	1.10–1.27	2.600 ± 0.010	63	1.236 ± 0.005	63	4.324 ± 0.035	63
12 Mar 2002	02:21–03:51	10.0	141.7	-25.8	1.08–1.29	2.529 ± 0.009	83	1.192 ± 0.004	83	4.106 ± 0.035	83

Table 7.1: C-14 observations. III.

Date	UT	Exp.	Lon.	Lat.	Airmass	750/795	N	825/890	N	795/890	N
13 Mar 2002	02:23–03:35	5.0	164.2	-25.8	1.08–1.25	2.501 ± 0.009	100	1.172 ± 0.005	100	4.075 ± 0.042	100
14 Mar 2002	02:26–03:35	10.0	186.7	-25.8	1.09–1.26	2.454 ± 0.010	65	1.247 ± 0.005	65	4.056 ± 0.035	65
15 Mar 2002	02:31–03:25	10.0	209.2	-25.8	1.11–1.24	2.520 ± 0.007	50	1.215 ± 0.004	50	4.140 ± 0.025	50
16 Mar 2002	02:27–03:20	10.0	231.7	-25.8	1.11–1.24	2.517 ± 0.007	50	1.202 ± 0.005	50	4.205 ± 0.039	50
17 Mar 2002	02:45–03:57	10.0	254.6	-25.8	1.15–1.39	2.480 ± 0.010	66	1.197 ± 0.006	66	3.862 ± 0.041	66
19 Mar 2002	03:29–04:21	10.0	300.1	-25.8	1.30–1.58	2.512 ± 0.012	50	1.229 ± 0.007	50	4.047 ± 0.035	50
20 Mar 2002	03:13–04:18	10.0	322.5	-25.8	1.26–1.58	2.523 ± 0.010	60	1.227 ± 0.005	60	4.054 ± 0.037	60
21 Mar 2002	02:46–04:27	5.0	344.8	-25.8	1.19–1.68	2.448 ± 0.025	140	1.171 ± 0.010	140	3.050 ± 0.320	140
22 Mar 2002	03:52–04:44	10.0	7.9	-25.8	1.46–1.87	2.519 ± 0.010	50	1.231 ± 0.006	50	3.917 ± 0.036	50
23 Mar 2002	03:21–03:50	10.0	29.7	-25.8	1.33–1.47	2.555 ± 0.015	27	1.204 ± 0.015	27	4.110 ± 0.063	26
25 Mar 2002	04:13–05:07	10.0	75.7	-25.9	1.68–2.33	2.532 ± 0.015	50	1.187 ± 0.007	50	3.965 ± 0.065	50
26 Mar 2002	03:45–04:25	5.0	97.6	-25.9	1.51–1.81	1.698 ± 0.209	36	0.800 ± 0.106	33	1.224 ± 2.296	10
27 Mar 2002	02:35–03:55	10.0	119.4	-25.9	1.22–1.60	2.597 ± 0.007	75	1.255 ± 0.004	75	4.314 ± 0.034	75
31 Mar 2002	03:27–04:09	10.0	209.9	-26.0	1.50–1.84	2.507 ± 0.015	40	1.189 ± 0.009	40	3.701 ± 0.085	40
01 Apr 2002	02:55–03:50	10.0	232.0	-26.0	1.36–1.69	2.486 ± 0.013	50	1.179 ± 0.008	50	4.005 ± 0.052	50
02 Apr 2002	03:08–03:51	10.0	254.6	-26.0	1.44–1.74	2.380 ± 0.017	40	1.186 ± 0.011	40	3.660 ± 0.082	40
05 Apr 2002	02:40–03:45	10.0	321.7	-26.0	1.35–1.78	2.516 ± 0.012	60	1.212 ± 0.006	60	3.938 ± 0.042	60
09 Apr 2002	02:49–03:31	10.0	51.5	-26.0	1.47–1.78	2.585 ± 0.015	40	1.206 ± 0.008	40	4.059 ± 0.076	40
10 Apr 2002	02:52–03:46	5.0	74.1	-26.0	1.50–1.98	2.519 ± 0.017	75	1.202 ± 0.011	75	3.884 ± 0.093	75
11 Apr 2002	02:53–03:41	10.0	96.5	-26.0	1.53–1.95	2.566 ± 0.018	45	1.198 ± 0.010	45	3.991 ± 0.065	45
12 Apr 2002	02:52–03:45	10.0	119.0	-26.1	1.55–2.05	2.570 ± 0.020	50	1.173 ± 0.009	50	3.775 ± 0.079	50

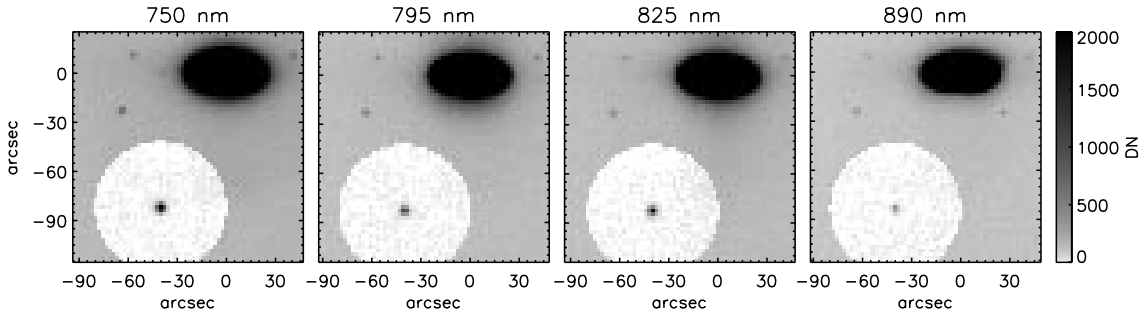

Figure 7.3: Same images as displayed in Fig. 7.1, but with Saturn's scattered light subtracted from the region surrounding Titan.

the 4 filters in order of ascending wavelength, completing a cycle of 4 exposures every 65 s (every 42 s when using 5 s integrations.)

7.3 Data reduction

Each image was corrected for the detector bias and dark current by subtracting a median of identical exposure dark frames taken the same night. Pixel-to-pixel gain variations were then compensated for by dividing each image by the mean of a set of daytime sky images taken once per month. A strong halo of scattered light surrounds Saturn's image on the detector and extends to Titan's vicinity, at a level of $\sim 5\%$ Titan's peak intensity (Fig. 7.1.) This effect is probably due to the highly reflective front surface of the interference filters used in these observations. To correct for the scattered light superimposed on Titan's image, we make the assumption that its intensity is radially symmetric about Saturn's position on the detector, and fit a 4th order polynomial to the background in an annulus $10''$–$40''$ around Titan. We then subtract this model of the background light from the entire region within $40''$ of Titan's location (Fig. 7.3.)

We computed Titan's instrumental magnitude in each image by summing the counts within an aperture centered on Titan's apparent position. The aperture radius was chosen by computing a nightly-mean PSF in each filter and determining the aperture necessary to sample 99.8% of its light, generally $8''$–$12''$. The signal to noise ratio of the resulting photometric measurement ranged from 100 (750 nm) to 15 (890 nm) on clear nights. Figure 7.4 displays the measured instrumental flux of Titan in all four filters on typical clear and partly-cloudy nights.

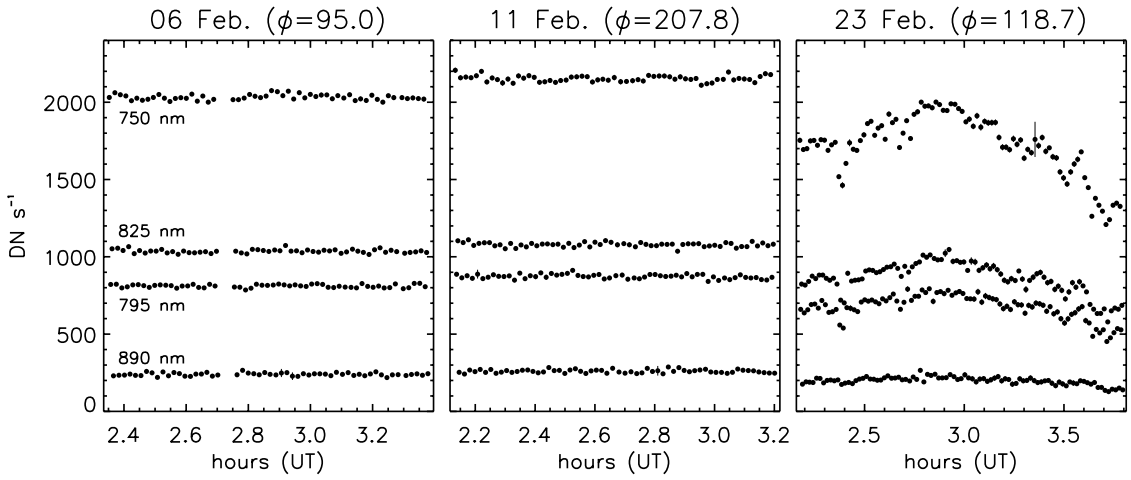

Figure 7.4: Photometry of Titan in four filters on three nights in February 2002. These nights were chosen to illustrate both clear and cloudy conditions, and to sample Titan's leading (6 and 23 February) and trailing (11 February) faces. Though we detect the surface albedo contrasts in the flux ratios (Fig. 7.5), the absolute flux variations seen here are due to changing extinction and clouds. The 1-σ error bars displayed include only the random error due to electronic and photon noise.

The purpose of alternating rapidly between surface-sensitive and CH_4 band filters is to calibrate out opacity variations imposed by atmospheric extinction and clouds on Earth. In practice, we cannot sample the photometry at a sufficiently high rate to keep up with the opacity variations of passing clouds. However, averaged over a sufficiently long period and assuming the opacity is not increasing or decreasing monotonically, the errors average out and the correct flux ratio can be recovered. There remains the concern that the clouds or other sources of opacity might redden Titan's spectrum, mimicking a change in surface albedo or cloud cover on Titan. This effect proves to be important in several filter ratios, and we correct for it below.

Having determined Titan's instrumental flux at 4 wavelengths, 6 possible flux ratios can be computed. The flux ratios 750/795 nm, 825/795 nm, and 825/890 nm record the albedo of Titan's surface and lower atmosphere, relative to that of the overlying haze. We disregard 750/890 nm as it is the most prone to the reddening previously mentioned. The flux ratio 750/825 nm compares the two surface-probing wavelengths, potentially allowing changes in the color of the lower atmosphere and surface to be detected. Similarly, the CH_4 band ratio 795/890 nm measures the color of the stratospheric haze. The most useful of these flux

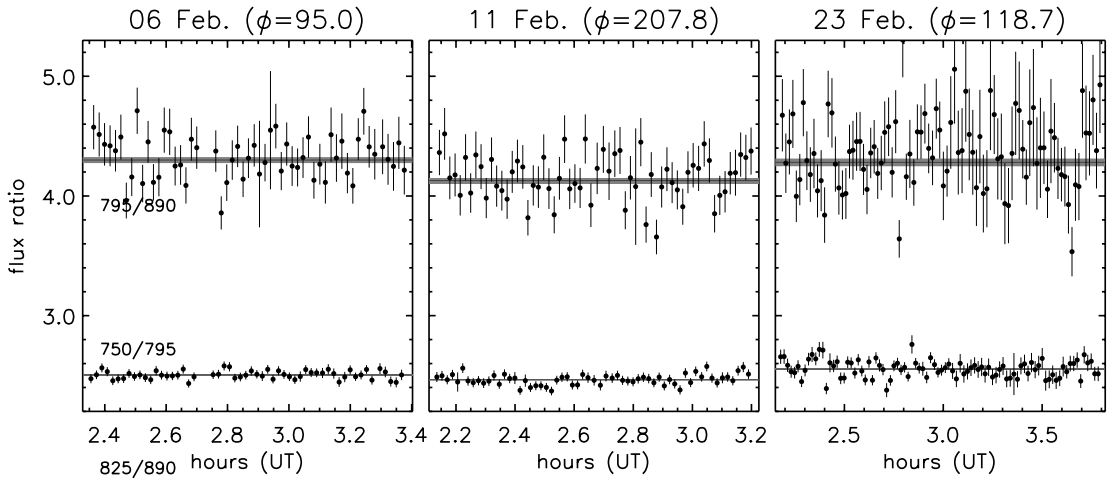

Figure 7.5: Ratio of Titan's flux in alternating filters, on the same nights as displayed in Fig. 7.4. The nightly mean flux ratio, and its 1-σ uncertainty, are indicated by the horizontal lines and gray bands. Note that while the surface-sensitive flux ratios 750/795 nm and 825/890 nm vary with rotational phase ϕ, the CH_4 band ratio 795/890 nm remains unchanged.

ratios proved to be 750/795 nm and 825/890 nm, providing two independent measurements of changes in the albedo of Titan's lower atmosphere and surface, and 795/890 nm as a control. We display time series of these three flux ratios in Fig. 7.5, for the same nights as the raw photometry in Fig. 7.4.

The final step of the initial data reduction process is to compute the weighted mean of each series of flux ratios for every night. The dominant source of uncertainty in the flux ratio estimate on cloudy nights is the temporal variation terrestrial cloud opacity between consecutive observations in the two filters. We therefore adopt the standard deviation of the measured flux ratios as our estimate of their uncertainty. On partly-cloudy nights, this is typically several times larger than the uncertainty expected from electronic and photon noise alone. We reject occasional outliers whose deviation from the weighted mean of that night is greater than 2σ (generally due to a cosmic ray hit within the photometric aperture). Taking a weighted average of the remaining flux ratios, we reduce the night's observations to the mean values of the following 3 flux ratios with associated uncertainties: 750/795 nm, 825/890 nm, and 795/890 nm. Nights on which the signal to noise ratio of the 825/890 nm mean was less than 60.0 were then excluded from further study, leaving 60 nights.

Rapidly alternating between filters and ratioing Titan's flux between them compensates

for correlated changes in flux between the filters, but it does not correct variable wavelength-dependent opacity. Though terrestrial clouds are generally assumed to be "gray" due to their large particle size, this may not be true at the level of a 1% flux ratio over 50 nm. Furthermore, several of our filters include H_2O absorption bands which may vary in opacity as a function of humidity. Though we did not observe any photometric standards, we can roughly estimate the mean extinction on each night by comparing Titan's raw 795 nm flux (in DN s^{-1}) recorded each of the 81 nights. As Fig. 7.6 illustrates, the measured 795 nm flux is dominated by the Earth's gradual recession from Titan, California's cyclic weather patterns, and the increasing airmass of the observations during the final 4 weeks of the project. Scaling Titan's predicted flux to match that observed on what was apparently the clearest night of the entire project (11 Feb 2002), we estimate the mean extinction $\tau_{795} = -\ln(I/I_0)$ on each night.

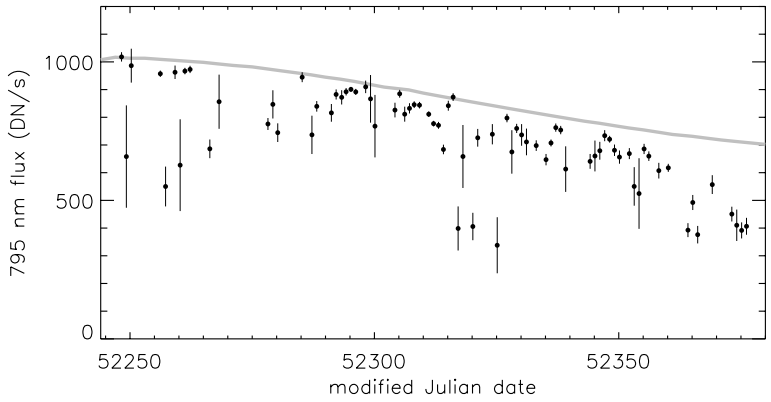

Figure 7.6: Titan's raw 795 nm instrumental flux over 81 nights. A simple model of the predicted flux, multiplied by an arbitrary scaling fact, is shown as a gray line. Error bars indicate the 1-σ standard deviation of the raw flux on each night, not the uncertainty in the mean.

Figure 7.7 displays the observed nightly-mean flux ratios of Titan with respect to the 795 nm extinction τ_{795}. While the 750/795 nm ratio displays no correlation with extinction, the 825/890 nm and 795/890 nm clearly do. This may be due to atmospheric H_2O absorptions within the passbands of the 890 nm and possibly the 825 nm filters, which increase in opacity on cloudy nights. No known H_2O bands are included in the 750 and 795 nm filter passbands. Regardless of its precise cause, we correct for this systematic reddening of Titan by performing a linear fit to the observed values of these two flux ratios, and correcting

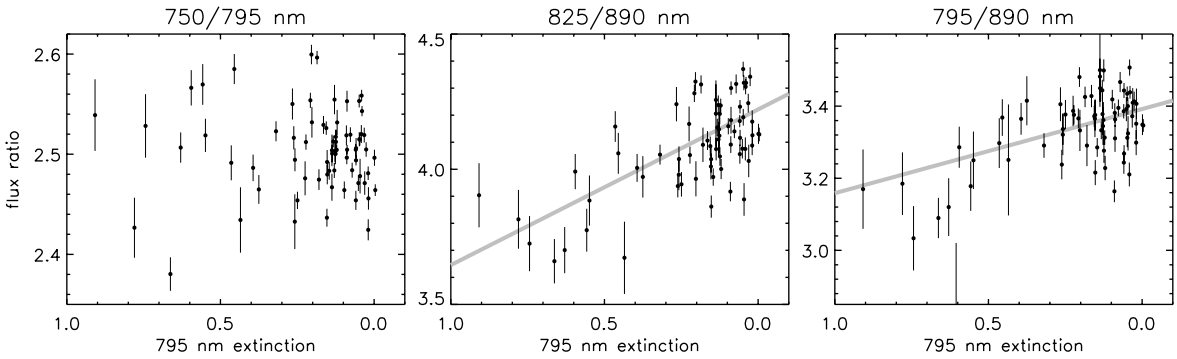

Figure 7.7: Ratios of Titan's flux in various filters, displayed with respect to the mean 795 nm extinction on that night. the 825/890 nm and 795/890 nm flux ratios show a clear dependence on extinction, probably due to variability of H_2O bands in the 890 and possibly the 825 nm filters. No similar effect is seen in the 750/795 nm flux ratio.

their value in the subsequent discussion as follows.

$$f'_{825/890} = f_{825/890} + 0.576\tau_{795} \tag{7.1}$$

$$f'_{795/890} = f_{795/890} + 0.233\tau_{795} \tag{7.2}$$

We present a time series of the corrected flux ratios over the entire 4 month duration of the project in Fig. 7.8, and display them with respect to Titan's orbital phase in Fig. 7.9. The 750/795 nm and 825/890 nm show a clear dependence on orbital phase, with Titan's leading hemisphere relatively brighter than the trailing hemisphere. This is consistent with all previous observations of Titan's surface, and demonstrates the sensitivity of these filters to light scattered from Titan's surface. Though we clearly detect Titan's hemispheric surface albedo contrast in the 750/795 nm flux ratio, its amplitude is low (2% peak-to-peak) due to the high optical depth of the overlying haze. The observed lightcurve amplitude increases to 5% in the 825 nm spectral window, which seem consistent with the 8% amplitude measured by **?** through the 1.1 μm window. As expected, the 795/890 nm flux ratio exhibits no statistically significant dependence on orbital phase.

7.4 Analysis

There is clearly more scatter superimposed on the repeating lightcurve than expected from the uncertainties which we estimate for the individual nightly-mean flux ratio measurements.

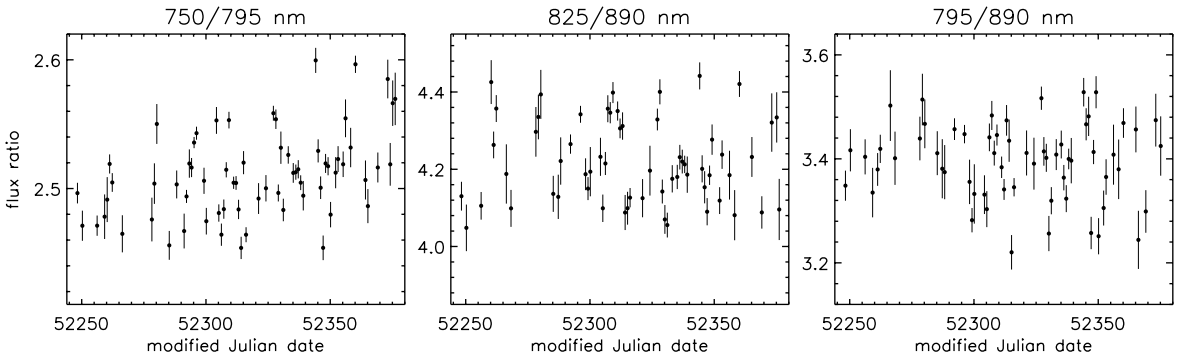

Figure 7.8: Titan's nightly-mean flux ratio, with respect to date, in three filter combinations. 750/795 nm and 825/890 nm provide two independent estimates of the albedo of the lower atmosphere and surface, with respect to the overlying haze. Surface albedo, tropospheric clouds, and gradual changes in the color of the overlying haze might all contribute to these two ratios. The 795/890 nm CH_4 band ratio is insensitive to albedo variations below Titan's tropopause. The same measurements are displayed with respect to Titan's orbital phase in Fig. 7.9

This scatter could be due to a varying bias in the measured flux ratios (such as a variable spectral slope imposed by the Earth's atmosphere) or to temporal variability of the albedo of Titan's surface, lower atmosphere (clouds), or stratospheric haze. To distinguish between these possible contributors, we subtract from the observations an *ad hoc* lightcurve model, determined by fitting a 4th-order Fourier series to the phased 750/795 nm and 825/890 nm flux ratios. The corrected surface-sensitive flux ratios are displayed in Fig. 7.10. A clear trend can be seen in the 750/795 nm flux ratio, which increases by 3% over the 4 months of observation. No comparable long-term trend is seen in either the corrected 825/890 nm flux ratio or the 795/890 nm CH_4 band ratio.

If a gradual decrease in Titan's 795 nm albedo were responsible for the trend in the 750/795 nm flux ratio, then we would expect the 795/890 nm CH_4 band ratio to increase by approximately the same magnitude. Such a result would not occur if Titan's albedo at 890 nm were decreasing at the same rate, but in that case we would note a comparable increase in the 825/890 nm albedo, which is clearly not seen. We must therefore conclude that Titan gradually brightened at 750 nm, with respect to the longer wavelength filters. This trend is consistent with the photometric results of Lockwood *et al.* at shorter wavelengths, reported in Lorenz *et al.* (1999), who observed Titan's "blue" albedo to rise at twice the rate of the "yellow" during 1972–1975, one Titan year previous. These seasonal

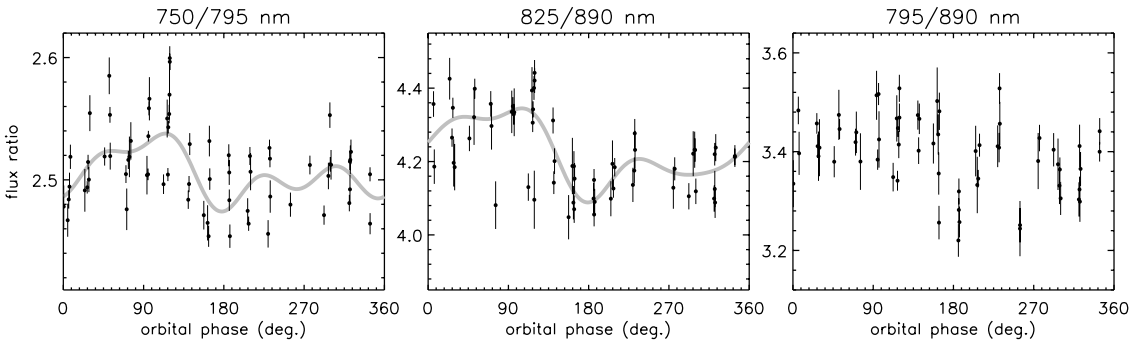

Figure 7.9: Titan's nightly-mean flux ratio, with respect to orbital phase, in three filter combinations. Titan's repeating lightcurve is approximated by the gray line, a least-squares fit 2nd-order Fourier series. The 795/890 nm CH_4 band flux ratio displays no statistically significant repeating lightcurve.

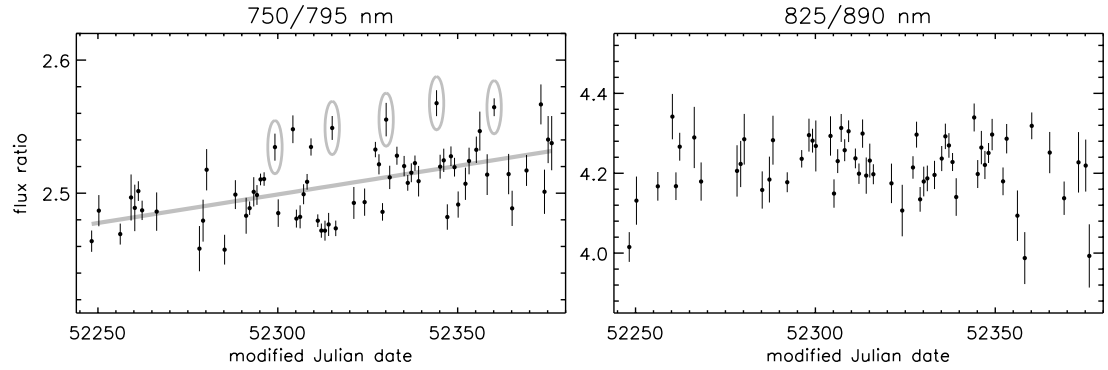

Figure 7.10: Titan's nightly-mean flux ratio, corrected for the repeating surface albedo Fourier series with Titan's orbital period has been subtracted. A clear trend can be seen in the 750/795 nm ratio, indicated by the linear fit in gray. Occasional brightenings of Titan's surface or lower atmosphere which appear to repeat at precisely the orbital period are marked with gray ovals.

albedo variations have been interpreted as being caused by the modification of the size distribution of the haze on the most visible (summer) hemisphere of Titan by meridional transport (Lorenz *et al.*, 1999). In short, though we do detect photons from Titan's surface at 750 nm, they are highly diluted by sunlight scattering off the optically thick haze, which was gradually brightening throughout the period of observation.

Besides this linear increase in the 750/795 nm flux ratio, we cannot conclusively identify any transient change in the flux ratios sensitive to the albedo of Titan's surface or lower atmosphere. Several suggestive features in the data do merit closer attention, however. We twice observed brightenings of the 750/795 nm flux ratio, by $> 3\sigma$ over the expected

mean lightcurve value, which repeated at Titan's orbital period. These observations in question are highlighted in Fig. 7.10. Unexpectedly high surface/lower atmosphere albedos were detected on 25 January, 10 and 25 February, and 11 and 27 March 2002, on which Titan's orbital phase was 186.0, 185.5, 163.7, 119.4, and 119.4, respectively. We have not highlighted every 3-σ deviation from the gradual brightening trend, but it may be significant that in these 5 cases, possible abnormal brightenings appear to repeat at the orbital period.

There are similarly suggestive indications of variability in the lower atmosphere and surface in the corrected 825/890 nm flux ratio, as the values gradually increase to a maximum near MJD 52305 (31 January 2002), then decrease somewhat before increasing to a second maximum near MJD 52335 (2 March 2002), before becoming too noisy to follow such subtle trends. However, these suggestive features in the 750/795 nm and 825/890 nm ratios do not appear to correlate, and we therefore cannot confidently claim to have detected any changes in the albedo of Titan's lower atmosphere and surface besides the unchanging surface lightcurve, on the basis of the C-14 photometry alone.

There are further reasons believe that the apparent lightcurve variability may not be due to changing clouds in Titan's troposphere. Recent nightly imaging of Titan with the Palomar adaptive optics (AO) system has revealed that the clouds currently account for only 0.4–1.3% of Titan's 2.0 μm flux, corresponding to 3–8% of the present peak-to-peak lightcurve amplitude (Ch. 6). If the contrast of surface features which cause Titan's lightcurve is similar at 750–825 nm and 2.0 μm, then we expect the clouds to have a similar photometric effect relative to the measured lightcurve amplitude in the visible. This is well below the 1 σ uncertainties of the measured 750/795 and 825/890 nm flux ratios. Only if the nightly clouds observed with the Palomar AO system were optically thin and composed of small (< 2 μm) droplets, or if the surface feature contrast were far lower in the visible, would the AO-imaged clouds be detectable in the C-14 photometry.

7.5 Conclusions

We attempted to detect the photometric signature of transient clouds in Titan's troposphere, using nightly narrow-band photometry on a 14-inch telescope on the Caltech campus. Though we clearly detect the repeating lightcurve of Titan's surface at 750 and 825 nm, transient brightenings due to clouds could not be conclusively identified. The technique

used remains promising, however, and implementation on a larger telescope or at a drier site might provide the signal-to-noise improvement necessary to achieve this project's goals.

Appendix A

Thesis data

This appendix contains the majority of the images and spectra of Titan analysed in this dissertation, in their most useful reduced and calibrated form. The data can be obtained from the following websites:

- http://www.gps.caltech.edu/~antonin/thesis/
- http://www.gps.caltech.edu/~titan/bouchez_thesis/

or directly from the author.

A.1 Spatially resolved spectra

This section contains the photometrically calibrated AO spectra of Titan which were analysed in Ch. 3. These data are available in the form of reduced long-slit spectra of chords across Titan's disk (two-dimentional FITS files) in which each row represents a spectum of a distinct location on Titan.

A.2 20 December 2001 occultation

This section contains MPEG movies of the occultation image sequence, and the astrometric and photometric analysis of each frame as described in Ch. 4. The data are available in the form of a 4100-line ASCII table, whose columns are as follows:

1. Image filename.
2. UTC from image header, `hh:mm:ss`.

3. Interpolated UTC midpoint time of frame, decimal hours.

4. Identifies which star is used as reference (columns 5–10 of this table). 1 = star A (western, brighter), 2 = star B (eastern, fainter).

5–6. $x_{\rm det}$ centroid location of reference star on detector, 1-σ uncertainty.

7–8. $y_{\rm det}$ centroid location of reference star on detector, 1-σ uncertainty

9–10. Nomalized flux of reference star ($\equiv$1.0), 1-σ uncertainty ($\equiv$ 0.0).

11–12. $x_{\rm det}$ centroid location of near-limb refracted image on detector, 1-σ uncertainty.

13–14. $y_{\rm det}$ centroid location of near-limb refracted image on detector, 1-σ uncertainty.

15–16. Flux of near-limb refracted image relative to reference star, 1-σ uncertainty.

17–18. $x_{\rm det}$ centroid location of far-limb refracted image on detector, 1-σ uncertainty.

19–20. $y_{\rm det}$ centroid location of far-limb refracted image on detector, 1-σ uncertainty.

21–22. Flux of far-limb refracted image relative to reference star, 1-σ uncertainty

A.3 Adaptive optics and speckle images at 2 μm

This appendix contains the 24 adaptive optics and speckle interferometric images of Titan analysed in Ch. 6, as well as the additional 4 adaptive optics images presented in Ch. 5. They are available as FITS and JPEG format images, with relevant ephemeris information.

Bibliography

Abreu, R., D. P. Chadwick, R. D'Amico, C. D. Delp, S. N. Gullapalli, D. Hansen, M. Marchionna, M. E. Meline, W. M. Rappoport, L. Mendyk, R. Pringle, K. Shu, W. Swanson, and W. P. Zmek 2000. SAAO adaptive optics system. In *Proc. SPIE Vol. 3931, p. 272-284, Gas, Chemical, and Electrical Lasers and Intense Beam Control and Applications, Santanu Basu; Steven J. Davis; Ernest A. Dorko; Eds.*, pp. 272–284.

Awal, M., and J. I. Lunine 1994. Moist convective clouds in Titan's atmosphere. *Geophysical Research Letters* **21**, 2491–2494.

Babcock, H. W. 1953. The Possibility of Compensating Astronomical Seeing. *Proceedings of the Astronomical Society of the Pacific* **65**, 229–+.

Baum, W. A., and A. D. Code 1953. A photometric observation of the occultation of a ARIETIS by upiter. *Astronomical Journal* **58**, 108–+.

Bouchez, A. H., M. E. Brown, C. A. Griffith, and R. G. Dekany 2000. Spatially Resolved Spectroscopy of Titan's Surface and Atmosphere. *AAS/Division for Planetary Sciences Meeting* **32**, 0–+.

Bouchez, A. H., M. E. Brown, C. R. Neyman, M. Troy, and R. Dekany 2003. Ground-based visible adaptive optics observations of titan's atmosphere and surface. *Icarus*. Submitted.

Brown, M. E., A. H. Bouchez, and C. A. Griffith 2002. Direct detection of variable tropospheric clouds near Titan's south pole. *Nature* **420**, 795–797.

Caldwell, J., C. C. Cunningham, D. Anthony, H. P. White, E. J. Groth, H. Hasan, K. Noll, P. H. Smith, M. G. Tomasko, and H. A. Weaver 1992. Titan: Evidence for seasonal change - A comparison of Hubble Space Telescope and Voyager images. *Icarus* **97**, 1–9.

Chamberlain, J. W., and C. A. Smith 1959. On the Excitation Rates and Intensities of OH in the Airglow. *Journal of Geophysical Research* **64**, 611–+.

Chanover, N. J., C. M. Anderson, C. P. McKay, P. Rannou, D. A. Glenar, J. J. Hillman, and W. E. Blass 2003. Probing Titan's lower atmosphere with acousto-optic tuning. *Icarus* **163**, 150–163.

Clark, R. N., and T. B. Mc Cord 1980. The Galilean satellites - New near-infrared spectral reflectance measurements /0.65-2.5 microns/ and a 0.325-5 micron summary. *Icarus* **41**, 323–339.

Combes, M., L. Vapillon, E. Gendron, A. Coustenis, O. Lai, R. Wittemberg, and R. Sirdey 1997. Spatially Resolved Images of Titan by Means of Adaptive Optics. *Icarus* **129**, 482–497.

Coustenis, A., and B. Bezard 1995. Titan's atmosphere from Voyager infrared observations. 4: Latitudinal variations of temperature and composition. *Icarus* **115**, 126–140.

Coustenis, A., E. Gendron, O. Lai, J. Véran, J. Woillez, M. Combes, L. Vapillon, T. Fusco, L. Mugnier, and P. Rannou 2001. Images of Titan at 1.3 and 1.6 μm with Adaptive Optics at the CFHT. *Icarus* **154**, 501–515.

Coustenis, A., E. Lellouch, J. P. Maillard, and C. P. McKay 1995. Titan's surface: composition and variability from the near-infrared albedo. *Icarus* **118**, 87–104.

Dekany, R. G. 1996. The Palomar adaptive optics system. In D. Optical Society of America, Washington (Ed.), *Adaptive optics*, Volume 13 of *OSA Technical Digest Series*, pp. 40–42.

Elliot, J. L., R. G. French, E. Dunham, P. J. Gierasch, J. Veverka, C. Church, and C. Sagan 1977. Occultation of Epsilon Geminorum by Mars. II - The structure and extinction of the Martian upper atmosphere. *Astrophysical Journal* **217**, 661–679.

Elliot, J. L., and C. B. Olkin 1996. Probing Planetary Atmospheres with Stellar Occultations. *Annual Review of Earth and Planetary Sciences* **24**, 89–124.

Elliot, J. L., D. F. Strobel, X. Zhu, L. H. Wasserman, and O. G. Franz 1998. The Structure of Triton's Middle Atmosphere from HST Stellar Occultation Observations. *Bulletin of the American Astronomical Society* **30**, 1107–+.

Fink, U., and H. P. Larson 1979. The infrared spectra of Uranus, Neptune, and Titan from 0.8 to 2.5 microns. *Astrophysical Journal* **233**, 1021–1040.

French, R. G., J. L. Elliot, and P. J. Gierasch 1978. Analysis of stellar occultation data - Effects of photon noise and initial conditions. *Icarus* **33**, 186–202.

French, R. G., C. A. McGhee, and B. Sicardy 1998. Neptune's Stratospheric Winds from Three Central Flash Occultations. *Icarus* **136**, 27–49.

Gibbard, S. G., B. Macintosh, D. Gavel, C. E. Max, I. de Pater, A. M. Ghez, E. F. Young, and C. P. McKay 1999. Titan: High-Resolution Speckle Images from the Keck Telescope. *Icarus* **139**, 189–201.

Goody, R. M. and Yung, Y. L. 1989. *Atmospheric Radiation: Theoretical Basis* (2nd ed.). New York: Oxford University Press.

Griffith, C. A. 1991. Investigations of Titan's troposphere and surface and Jupiter's great red spot with infrared observations. *Ph.D. Thesis*.

Griffith, C. A. 1993. Evidence for surface heterogeneity on Titan. *Nature* **364**, 511–514.

Griffith, C. A., J. L. Hall, and T. R. Geballe 2000. Detection of Daily Clouds on Titan. *Science* **290**, 509–513.

Griffith, C. A., J. L. Hall, E. Young, J. Cook, and P. Rannou 2003. Imaging temporal changes on titan. *Icarus*. In press.

Griffith, C. A., T. Owen, G. A. Miller, and T. Geballe 1998. Transient clouds in Titan's lower atmosphere. *Nature* **395**, 575–578.

Griffith, C. A., T. Owen, and R. Wagener 1991. Titan's surface and troposphere, investigated with ground-based, near-infrared observations. *Icarus* **93**, 362–378.

Hansen, J. E., and L. D. Travis 1974. Light scattering in planetary atmospheres. *Space Science Reviews* **16**, 527–610.

Hayward, T. L., B. Brandl, B. Pirger, C. Blacken, G. E. Gull, J. Schoenwald, and J. R. Houck 2001. PHARO: A Near-Infrared Camera for the Palomar Adaptive Optics System. *Proceedings of the Astronomical Society of the Pacific* **113**, 105–118.

Hourdin, F., O. Talagrand, R. Sadourny, R. Courtin, D. Gautier, and C. P. McKay 1995. Numerical simulation of the general circulation of the atmosphere of Titan. *Icarus* **117**, 358–374.

Hubbard, W. B., et al. 1993. The occultation of 28 SGR by Titan. *Astronomy and Astrophysics* **269**, 541–563.

Hunten, D. M., M. G. Tomasko, F. M. Flasar, R. E. Samuelson, D. F. Strobel, and D. J. Stevenson 1984. Titan. In *Saturn*, pp. 671–759.

Hutzell, W. T., C. P. McKay, O. B. Toon, and F. Hourdin 1996. Simulations of Titan's Brightness by a Two-Dimensional Haze Model. *Icarus* **119**, 112–129.

Ingersoll, A. P. 1970. Motions in Planetary Atmospheres and the Interpretation of Radio Occultation Data. *Icarus* **13**, 34–+.

Jefferies, S. M., and J. C. Christou 1993. Restoration of Astronomical Images by Iterative Blind Deconvolution. *Astrophysical Journal* **415**, 862–+.

Kärcher, B. 2002. Properties of subvisible cirrus formed by homogeneous freezing. *Atmos. Chem. & Phys.* **2**, 161–170.

Karkoschka, E. 1998. Methane, Ammonia, and Temperature Measurements of the Jovian Planets and Titan from CCD-Spectrophotometry. *Icarus* **133**, 134–146.

Khare, B. N., C. Sagan, E. T. Arakawa, F. Suits, T. A. Callcott, and M. W. Williams 1984. Optical constants of organic tholins produced in a simulated Titanian atmosphere - From soft X-ray to microwave frequencies. *Icarus* **60**, 127–137.

Khare, B. N., W. R. Thompson, C. Sagan, E. T. Arakawa, and J. J. Lawn 1990. Optical Constants of Solid Ethane from 0.4 to 2.5 μ. *Bulletin of the American Astronomical Society* **22**, 1033–+.

Koresko, C. D., S. V. W. Beckwith, A. M. Ghez, K. Matthews, and G. Neugebauer 1991. An infrared companion to Z Canis Majoris. *Astronomical Journal* **102**, 2073–2078.

Kostiuk, T., K. E. Fast, T. A. Livengood, T. Hewagama, J. J. Goldstein, F. Espenak, and D. Buhl 2001. Direct Measurement of Winds on Titan. *Geophysical Research Letters* **28**, 2361–+.

Kunde, V. G., A. C. Aikin, R. A. Hanel, D. E. Jennings, W. C. Maguire, and R. E. Samuelson 1981. C4H2, HC3N and C2N2 in Titan's atmosphere. *Nature* **292**, 686–688.

Lellouch, E. 1990. Atmospheric models of Titan and Triton. *Annales Geophysicae* **8**, 653–660.

Lellouch, E., A. Coustenis, D. Gautier, F. Raulin, N. Dubouloz, and C. Frere 1989. Titan's atmosphere and hypothesized ocean - A reanalysis of the Voyager 1 radio-occultation and IRIS 7.7-micron data. *Icarus* **79**, 328–349.

Lemmon, M. T., E. Karkoschka, and M. Tomasko 1993. Titan's rotation - Surface feature observed. *Icarus* **103**, 329–332.

Lemmon, M. T., E. Karkoschka, and M. Tomasko 1995. Titan's rotational light-curve. *Icarus* **113**, 27–38.

Lindal, G. F., D. N. Sweetnam, and V. R. Eshleman 1985. The atmosphere of Saturn - an analysis of the Voyager radio occultation measurements. *Astronomical Journal* **90**, 1136–1146.

Lindal, G. F., G. E. Wood, H. B. Hotz, D. N. Sweetnam, V. R. Eshleman, and G. L. Tyler 1983. The atmosphere of Titan - an analysis of the Voyager 1 radio occultation measurements. *Icarus* **53**, 348–363.

Lorenz, R. D. 1993. The life, death and afterlife of a raindrop on Titan. *Planetary and Space Science* **41**, 647–655.

Lorenz, R. D., M. T. Lemmon, P. H. Smith, and G. W. Lockwood 1999. Seasonal Change on Titan Observed with the Hubble Space Telescope WFPC-2. *Icarus* **142**, 391–401.

Lorenz, R. D., P. H. Smith, M. T. Lemmon, E. Karkoschka, G. W. Lockwood, and J. Caldwell 1997. Titan's North-South Asymmetry from HST and Voyager Imaging: Comparison with Models and Ground-Based Photometry. *Icarus* **127**, 173–189.

Lorenz, R. D., E. F. Young, and M. T. Lemmon 2001. Titan's Smile and Collar: HST Observations of Seasonal Change 1994-2000. *Geophysical Research Letters* **28**, 4453–+.

Lunine, J. I., D. J. Stevenson, and Y. L. Yung 1983. Ethane ocean on Titan. *Science* **222**, 1229–+.

Müller-Wodarg, I. C. F., and R. V. Yelle 2002. The effect of dynamics on the composition of Titan's upper atmosphere. *Geophysical Research Letters* **29**, 54–1.

Markwardt, C. B. 2003. , http://cow.physics.wisc.edu/~craigm/idl/idl.html.

Matthews, K., A. M. Ghez, A. J. Weinberger, and G. Neugebauer 1996. The First Diffraction-Limited Images from the W. M. Keck Telescope. *Proceedings of the Astronomical Society of the Pacific* **108**, 615–+.

Matthews, K., and B. T. Soifer 1994. The Near Infrared Camera on the W. M. Keck Telescope. In *ASSL Vol. 190: Astronomy with Arrays, The Next Generation*, pp. 239–+.

McKay, C. P. 1996. Elemental composition, solubility, and optical properties of Titan's organic haze. *Planetary and Space Science* **44**, 741–747.

McKay, C. P., A. Coustenis, R. E. Samuelson, M. T. Lemmon, R. D. Lorenz, M. Cabane, P. Rannou, and P. Drossart 2001. Physical properties of the organic aerosols and clouds on Titan. *Planetary and Space Science* **49**, 79–99.

McKay, C. P., S. C. Martin, C. A. Griffith, and R. M. Keller 1997. Temperature Lapse Rate and Methane in Titan's Troposphere. *Icarus* **129**, 498–505.

McLean, I. S., E. E. Becklin, O. Bendiksen, G. Brims, J. Canfield, D. F. Figer, J. R. Graham, J. Hare, F. Lacayanga, J. E. Larkin, S. B. Larson, N. Levenson, N. Magnone, H. Teplitz, and W. Wong 1998. Design and development of NIRSPEC: a near-infrared echelle spectrograph for the Keck II telescope. In *Proc. SPIE Vol. 3354, p. 566-578, Infrared Astronomical Instrumentation, Albert M. Fowler; Ed.*, pp. 566–578.

Meier, R., B. A. Smith, T. C. Owen, and R. J. Terrile 2000. The surface of Titan from NICMOS observations with the Hubble Space Telescope. *Icarus* **145**, 462–473.

Metchev, S. A., L. A. Hillenbrand, and R. J. White 2003. Adaptive Optics Observations of Vega: Eight Detected Sources and Upper Limits to Planetary-Mass Companions. *Astrophysical Journal* **582**, 1102–1108.

Moré, J. J., B. S. Garbow, and K. E. Hillstrom 1980. User guide for MINPACK-1. Report ANL-80-74.

Nicholson, P. D., C. A. McGhee, and R. G. French 1995. Saturn's central flash from the 3 July 1989 occultation of 28 SGR. *Icarus* **113**, 57–83.

Press, W. H., B. P. Flannery, S. A. Teukolsky, and W. T. Vetterling 1992. *Numerical Recipes: The Art of Scientific Computing* (2nd ed.). Cambridge (UK) and New York: Cambridge University Press.

Rages, K., and J. B. Pollack 1983. Vertical distribution of scattering hazes in Titan's upper atmosphere. *Icarus* **55**, 50–62.

Rannou, P., M. Cabane, E. Chassefiere, R. Botet, C. P. McKay, and R. Courtin 1995. Titan's geometric albedo: Role of the fractal structure of the aerosols. *Icarus* **118**, 355–372.

Rannou, P., F. Hourdin, and C. P. McKay 2002. A wind origin for Titan's haze structure. *Nature* **418**, 853–856.

Richardson, J. E., R. D. Lorenz, and A. McEwen 2001. Titan's Surface and Rotation: New Results from Voyager 1 Images. *AAS/Division for Planetary Sciences Meeting* **33**, 0–+.

Roberts, L. C. 2001. High dynamic range astrometry with the AEOS adaptive optics system. AMOS 2001 Technical Conference proceedings, pp. 326–332.

Roberts, L. C., and C. R. Neyman 2002. Characterization of the AEOS Adaptive Optics System. *Proceedings of the Astronomical Society of the Pacific* **114**, 1260–1266.

Roe, H. G. 2002a. Implications of Atmospheric Differential Refraction for Adaptive Optics Observations. *Proceedings of the Astronomical Society of the Pacific* **114**, 450–461.

Roe, H. G. 2002b. *Titan's atmosphere at high resolution.* Ph. D. thesis, University of California, Berkeley.

Roe, H. G., I. de Pater, B. A. Macintosh, and C. P. McKay 2002. Titan's Clouds from Gemini and Keck Adaptive Optics Imaging. *Astrophysical Journal* **581**, 1399–1406.

Samuelson, R. E., and L. A. Mayo 1997. Steady-state model for methane condensation in Titan's troposphere. *Planetary and Space Science* **45**, 949–958.

Samuelson, R. E., L. A. Mayo, M. A. Knuckles, and R. J. Khanna 1997. C_4N_2 ice in Titan's north polar stratosphere. *Planetary and Space Science* **45**, 941–948.

Sicardy, B., F. Ferri, F. Roques, J. Lecacheux, S. Pau, N. Brosch, Y. Nevo, W. B. Hubbard, H. J. Reitsema, C. Blanco, E. Carreira, W. Beisker, C. Bittner, H.-J. Bode, M. Bruns, H. Denzau, M. Nezel, E. Riedel, H. Struckmann, G. Appleby, R. W. Forrest, I. K. M. Nicolson, A. J. Hollis, and R. Miles 1999. The Structure of Titan's Stratosphere from the 28 Sgr Occultation. *Icarus* **142**, 357–390.

Smart, W. M. 1931. *Textbook on Spherical Astronomy* (1st ed.). Cambridge (UK): Cambridge University Press.

Smith, B. A., L. Soderblom, R. F. Beebe, J. M. Boyce, G. Briggs, A. Bunker, S. A. Collins, C. Hansen, T. V. Johnson, J. L. Mitchell, R. J. Terrile, M. H. Carr, A. F. Cook, J. N. Cuzzi, J. B. Pollack, G. E. Danielson, A. P. Ingersoll, M. E. Davies, G. E. Hunt, H. Masursky, E. M. Shoemaker, D. Morrison, T. Owen, C. Sagan, J. Veverka, R. Strom, and V. E. Suomi 1981. Encounter with Saturn - Voyager 1 imaging science results. *Science* **212**, 163–191.

Smith, P. H., M. T. Lemmon, R. D. Lorenz, L. A. Sromovsky, J. J. Caldwell, and M. D. Allison 1996. Titan's Surface, Revealed by HST Imaging. *Icarus* **119**, 336–349.

Sromovsky, L. A., V. E. Suomi, J. B. Pollack, R. J. Krauss, S. S. Limaye, T. Owen, H. E. Revercomb, and C. Sagan 1981. Implications of Titan's north-south brightness asymmetry. *Nature* **292**, 698–702.

Tokano, T., F. M. Neubauer, M. Laube, and C. P. McKay 1999. Seasonal variation of Titans atmospheric structuresimulated by a general circulation model. *Planetary and Space Science* **47**, 493–520.

Tokano, T., F. M. Neubauer, M. Laube, and C. P. McKay 2001. Three-Dimensional Modeling of the Tropospheric Methane Cycle on Titan. *Icarus* **153**, 130–147.

Wizinowich, P., D. S. Acton, C. Shelton, P. Stomski, J. Gathright, K. Ho, W. Lupton, K. Tsubota, O. Lai, C. Max, J. Brase, J. An, K. Avicola, S. Olivier, D. Gavel, B. Macintosh, A. Ghez, and J. Larkin 2000. First Light Adaptive Optics Images from the Keck

II Telescope: A New Era of High Angular Resolution Imagery. *Proceedings of the Astronomical Society of the Pacific* **112**, 315–319.

Wizinowich, P. L., D. S. Acton, O. Lai, J. Gathright, W. Lupton, and P. J. Stomski 2000. Performance of the W.M. Keck Observatory Natural Guide Star Adaptive Optic Facility: the first year at the telescope. In *Proc. SPIE Vol. 4007, p. 2-13, Adaptive Optical Systems Technology, Peter L. Wizinowich; Ed.*, pp. 2–13.

Yelle, R. V., D. F. Strobell, E. Lellouch, and D. Gautier 1997. The Yelle Titan Atmosphere Engineering Models. In *Huygens: Science, Payload and Mission*, pp. 243+.

Young, E. F., P. Rannou, C. P. McKay, C. A. Griffith, and K. Noll 2002. A Three-dimensional Map of Titan's Tropospheric Haze Distribution Based on Hubble Space Telescope Imaging. *Astronomical Journal* **123**, 3473–3486.

Young, L. A. 2001. , http://www.boulder.swri.edu/~layoung/occl/occl.html.

Yung, Y. L., M. Allen, and J. P. Pinto 1984. Photochemistry of the atmosphere of Titan - Comparison between model and observations. *Astrophysical Journal Supplement* **55**, 465–506.